UNIVERSITÀ DI PISA

DIPARTIMENTO DI INGEGNERIA INDUSTRIALE

Laurea Magistrale in Ingegneria Aeronautica

Rhegmatogenous retinal detachment: a fluid-structure-interaction investigation

Relatori:

Prof. Simone Camarri

Prof. Francesco Viola

Prof. Jan Pralitis

Prof. Rodolfo Repetto

Candidato:

Geraldina Berti

ANNO ACCADEMICO 2023/2024

Contents

Chapter 1

Rhegmatogenous Retinal Detachment

Rhegmatogenous Retinal Detachment (RRD) is a clinical condition including a retinal break and vitreous liquefaction. As a matter of fact, the name of this eye pathology comes from the Greek word "rhegma", which stands for "rupture".
In order to deeply understand the mechanism behind the RRD, it is necessary to have an overview on the structure of the eye and of its main activities of fluid transportation.
The eye has an approximately spherical shape, hence the name "eyeball". Its main structural component is the outer layer, called "corneoscleral envelope", from the name of its two parts, the cornea and the sclera. Both the cornea and the sclera are predominantly made of collagen and they are in direct continuation with each other, but their color and their purpose are different. In the anterior part of the eye, there are the iris and the lens. Both the cornea and the lens lack a blood supply, but their nutrition is based on the circulation of the aqueous humor. The aqueous humor is also needed to maintain the almost-spherical shape of the eyeball, whose corneoscleral envelope is flexible but inextensible. Through the production of aqueous fluid, the eyeball is "inflated" and an intraocular pressure (IOP) is generated. The posterior part of the eyeball contains the retina. The retina forms from the optic vesicles, which are an outpouching of the developing midbrain and invaginate to become the optic cup. The anterior wall of the cup forms the retina, whereas the posterior wall develops into the retinal pigment epithelium (RPE). In pathological cases, a gap, called subretinal space, might exist between the retina and the RPE and it is in this space that fluid accumulates in case of a retinal detachment. The RPE has the major function of pumping out the fluid that leaks into the subretinal space. The RPE prevents the formation of a subretinal gap, since it is necessary to have a close apposition of the retina with the RPE for the correct functioning of the retina itself.
The retina and the RPE are separated from the sclera by the choroid. The choroid is the major blood supply to the eye, the choroidal circulation, which absorbs the

fluid pumped out of the subretinal space by the RPE. If the pump fails, there is fluid accumulation both in the retina and in the subretinal space. [1] Behind the lens there is the vitreous chamber of the eye, which is surrounded posteriorly by the retina. The vitreous chamber is filled with the vitreous humor, which has the consistency of a gel and viscoelastic properties in young healthy subjects. The vitreous humor is in contact with the crystalline lens anteriorly and it is adherent to the retina posteriorly. As a matter of fact, it holds the retina in contact with the RPE, but vitreoretinal tractions, generated during vitreous motion, may lead to retinal detachment.
Figure 1.1 shows the anatomy of the human eye.

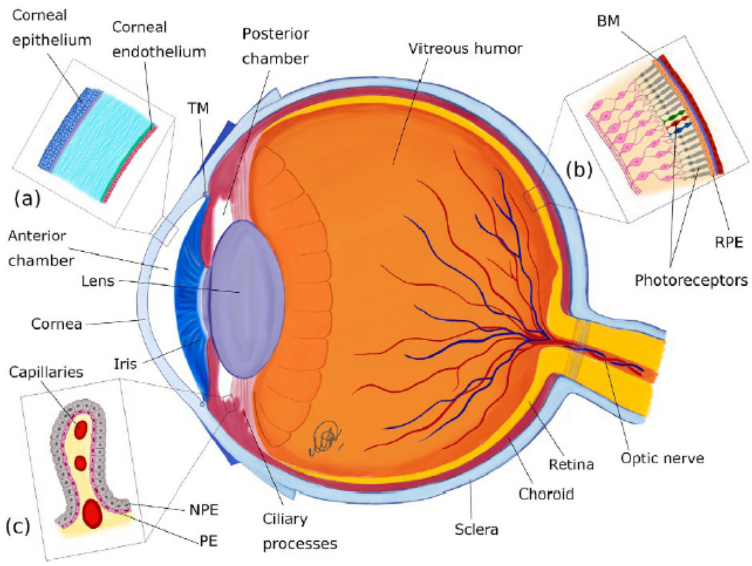

Figure 1.1: Anatomy of the human eye. Source: "Modeling of Mass Transport Processes in Biological Media", Sid M. Beckeret al. add the year

It is also important to introduce the anatomic equator of the eyeball, defined as a circumferential line on which every point is equidistant from the anterior and posterior poles; since the eye is not perfectly spherical, the anatomic equator divides the globe into two unequal halves, the anterior and the posterior hemispheres, and it is, on average, approximately 12.5 to 14 mm behind the limbus, defined as the border between the cornea and the sclera. The anatomic equator is different from the geometric equator, whose diameter is perpendicular to the geometric axis and whose center is equidistant from the anterior and posterior poles. These two equators do not coincide due to the non-perfectly spherical shape of the eye; since the sclera bulges more temporally, the anatomic axis is farther posterior on its temporal side than on its nasal side, as shown in Figure 1.2

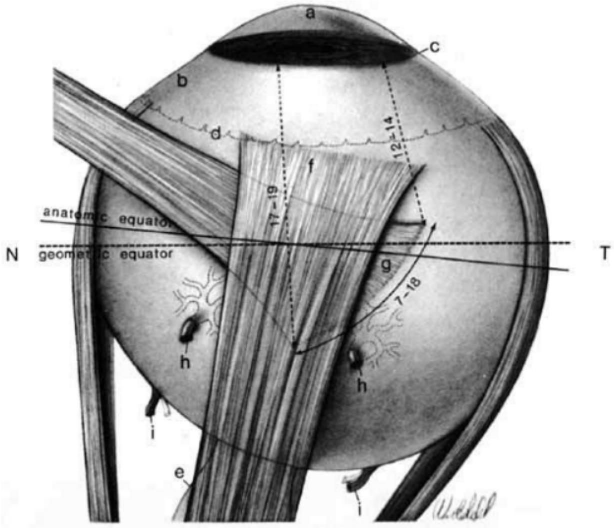

Figure 1.2: Anatomic and geometric equators of the human eye. Source: https://entokey.com/topographic-anatomy-of-the-eye-an-overview/

1.1 Genesis of the pathology

The vitreous humor, introduced above, is a clear transparent matter, mainly made of water, salts, collagen and hyaluronic acid; the latter two substances determine the gel-like characteristics of the vitreous humor in healthy young subjects.
With ageing, a degradation process of the vitreous body might occur and it may cause gel liquefaction, called synchisis, and collagen fiber aggregation, responsible for the shrinking of the vitreous gel (syneresis). [2]
In the major percentage of cases, RRD begins with a posterior vitreous detachment (PVD), consisting in the separation of the vitreous body from the retina. PVD usually occurs in the posterior part of the eyeball due to the progressive shrinking of the vitreous gel. At regions of significant adhesion between the vitreous and the retina, PVD causes vitreoretinal traction, responsible for the creation of retinal tears. Vitreoretinal traction is caused by gravitational force on the vitreous gel and, especially, by rotational eye movement, due to the inertia of the vitreous gel itself.
It is to mention that in a smaller but still significant percentage of patients a complete PVD doesn't occur and vitreoretinal traction may occur in regions of the retina that are near breaks which were unrelated to the PVD process, but the presence of PVD associated with ocular diseases is related to a higher incidence of retinal detachment. [3]
RRD consists in the separation of the sensory layer of the retina from the RPE and it occurs when, after the creation of a retinal break, there's a flow of liquefied vitreous into the subretinal space. It can be said that, in order to have an RRD, it is necessary to have a combination of retinal breaks, vitreous liquefaction and detachment, traction on the retina and intraocular fluids currents; moreover, to make this phenomenon occur, the traction on the retina must exceed the forces

responsible to keep the retina in place.
Retinal breaks can be classified into three different types. Of these, retinal holes are full-thickness retinal defects typically not associated with persistent retinal traction in their vicinity; dialyses are circumferential retinal breaks that occur at ora serrata, the serrated junction between the choroid and the ciliary body, and are usually associated with blunt ocular trauma; retinal tears, instead, are usually caused by an acute PVD at sites of strong vitreoretinal adhesion. Figure 1.3, Figure 1.4 and Figure 1.5 show an example of retinal hole, retinal dialysis and retinal tear respectively. Later in this work, both retinal holes and retinal tears will be discussed.

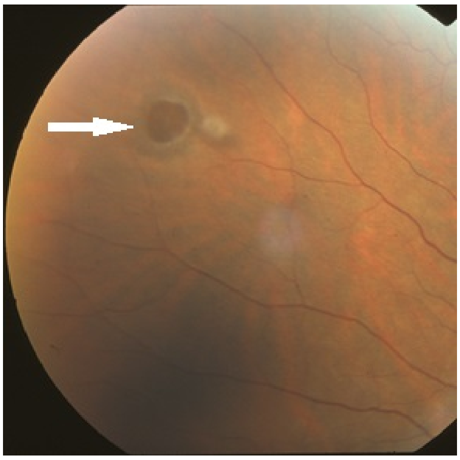

Figure 1.3: Example of retinal hole. Source: https://www.reviewofophthalmology.com/article/evaluation-and-management-of-pvd

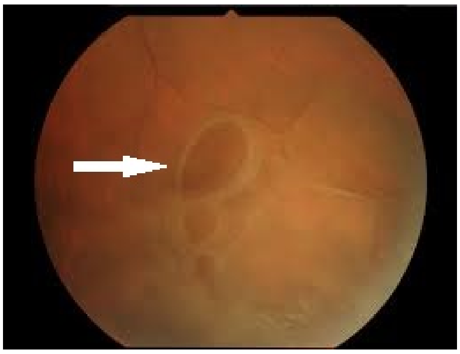

Figure 1.4: Example of retinal dialysis. Source: https://jfophth.com/traumatic-retinal-dialysis/

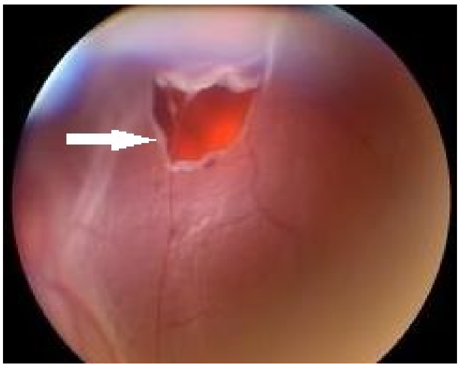

Figure 1.5: Example of retinal tear. Source: https://www.elmanretina.com/what-is-a-retinal-tear-and-how-can-an-eye-surgeon-help/

1.2 Scleral buckling

When RRD occurs, there are three main surgical ways to reattach the retina: scleral buckling, vitrectomy and pneumatic retinopexy.
Scleral buckling is a surgical procedure performed to produce functional closure of retinal breaks responsible for retinal detachment; after the closure, the normal physiological forces can maintain the retina attached permanently.
The term “buckle” means “deformation of a structure under stress”; the name “scleral buckling” comes from the main feature of this surgical procedure, since it consists in the deformation of the inner scleral surface from concave to convex under the application of various shapes of silicon rubber elements to the sclera.
The shape and dimensions of the scleral buckle depend on the location, size, amount and type of the retinal breaks. It is possible to classify the episcleral implants into segmental and encircling ones. Segmental scleral buckles can be radially or circumferentially oriented; radial scleral buckles provide focal support for a retinal tear and minimize the development of radial retinal folds, which will be discussed in more detail later; circumferential scleral buckles provide a zone of support oriented parallel to the region where vitreous traction is more intense, but, on the other side, they increase the risk of retinal folds development. Encircling buckles are buckles encircling the sclera for 360 degrees and are usually intended to support breaks in the region of the posterior edge of the vitreous base. If, when an encircling band is used, an increased buckling effect is needed in only a small area, a radially oriented segment is placed beneath the band.
To sum up, the surgical procedure might involve the usage of a segmental scleral buckle, of a circumferential scleral buckle or of the combination of them both depending on the position, magnitude and amount of breaks. Figure 1.6 represents different configurations for scleral buckles.

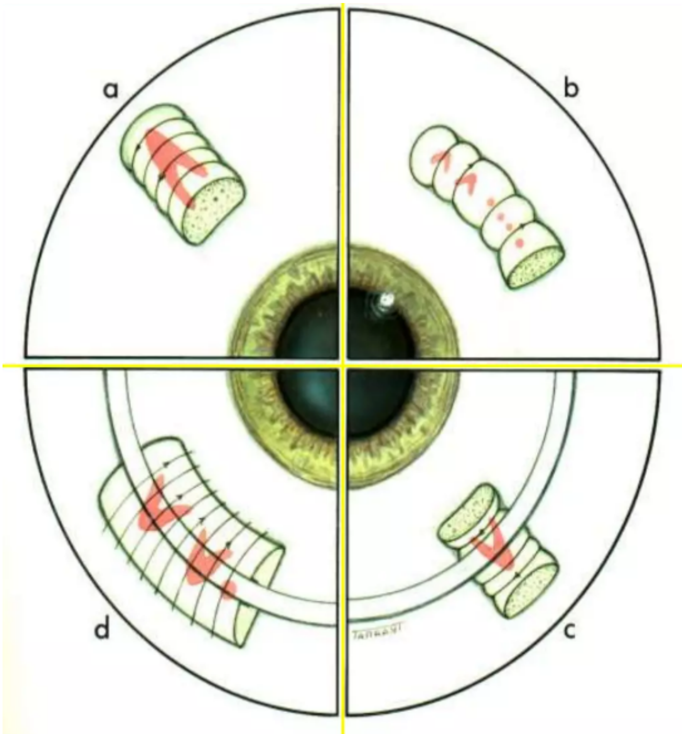

Figure 1.6: Different configurations of scleral buckles: segmental radial (a), segmental circumferential (b), encircling augmented by radial sponge (c), encircling augmented by circumferential sponge (d). Source: Dr. Hendavitharana, "Rhegmatogenous Retinal Detachment"

It is possible to differentiate two types of procedures for the application of a scleral buckle: a non-drainage procedure and a drainage procedure. In the first case, the functional closure of retinal breaks comes from the several beneficial effects of scleral buckling only, such as reduction of retinal traction, displacement of subretinal fluids away from the location of retinal break and scleral buckle, change in the effect of intraocular currents that encourage liquid vitreous to enter the subretinal space thanks to the alteration of the concave shape of the eyeball and increase in resistance to fluid flow through the retinal break. In case of a drainage procedure, after the scleral band has been positioned, an evacuative puncture is made, in a site where there is a lot of fluid, and, at the same time, a flat tool pushes the eye wall to help the subretinal fluid to be drained; moreover, a gas bubble is injected into the eye, in order to get back the volume lost through the drainage: the air bubble expands and pushes the retina to the wall from inside and flattens the break. To minimize the passage of vitreous through the break and out of the eye, drainage of subretinal fluid should be performed at a certain distance from retinal breaks, but its exact position is determined by the configuration of retinal detachment. In a drainage procedure, the previously mentioned beneficial effects of scleral buckling are still present, but the closure of the break is more immediate.
In order to make the procedure for scleral buckling clear, an example of the surgical procedure in its sequential steps of execution is given below. This example concerns

a standard drainage-procedure to fix a retinal detachment through scleral buckling in case of a retinal horseshoe tear. In this example, it is considered the use of an encircling scleral buckle, style 506, which is an oval sponge of dimensions 3.0mm x 5.0mm, as shown in Figure 1.7.

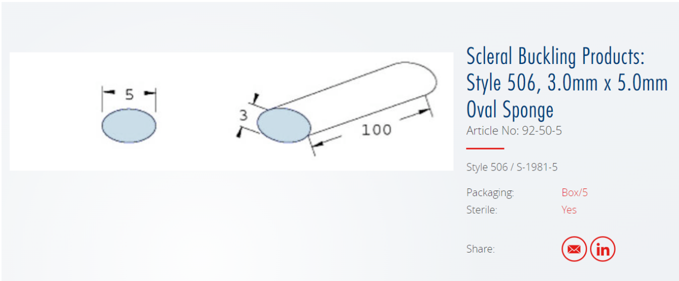

Figure 1.7: Common geometry for scleral buckles. Source: DORC

Figure 1.8 shows the different steps of the surgical practice for scleral buckling. In (a), a retinal horseshoe tear (in yellow) has formed and its anterior edge is attached to the vitreous gel (in grey). The encircling band is inserted under the four rectus muscles of the eye, as shown in (b). In order to understand where to put the buckle, the position of the break is shown through the use of a light (in (c)) and, then, it is treated with cryopexy, a procedure that uses extreme cold therapy or freezing to treat the retinal tear; later, the break is marked on the sclera. The following steps consist of the evacuative puncture, the use of a flat tool to improve the drainage of fluid and, finally, the insertion of a gas bubble (in (d), (e) and (f), respectively). As explained before, the gas bubble expands and pushes the retina from the inside (in (g) and in (h)).

Eventually, the encircling band is fixed with sutures and its position is such that the break is in the middle of the band (in (i)); at the end of the procedure, the band should create a 1.15 mm indentation from outside and the air bubble should push the retina from the inside (in (j)).

The decision of drainage of subretinal fluids depends on several factors, such as the configuration and the size of retinal tears, the amount of traction, but also the subjective experience of the surgeon regarding the amount of subretinal fluid that can be allowed to remain between the crest of the buckle and the break. Generally, drainage is almost never performed if a single break can be easily and almost completely closed without draining the fluid; on the other side, drainage is almost always performed when a high and broad encircling scleral buckle is required. [3]

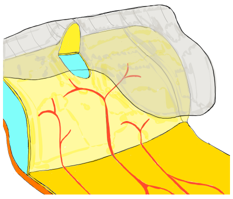

(a) Horseshoe retinal tear

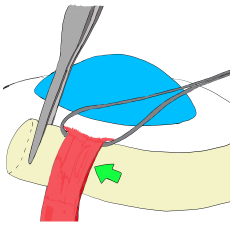

(b) Insertion of the scleral buckle

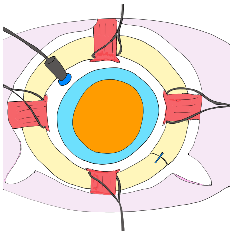

(c) Highlighting of the retinal break

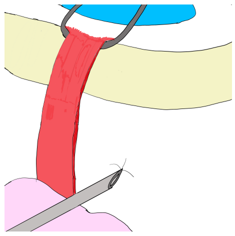

(d) Evacuative puncture

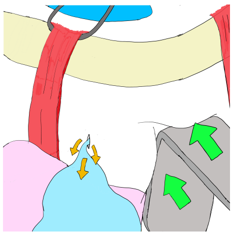

(e) Drainage of the fluid through a flat tool

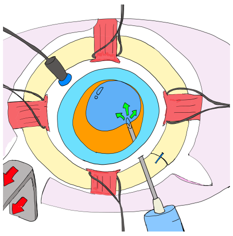

(f) Insertion of a gas bubble

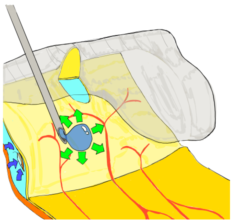

(g) Expansion of the gas bubble

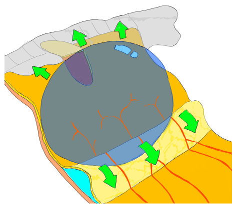

(h) The gas bubble pushes the retina from the inside

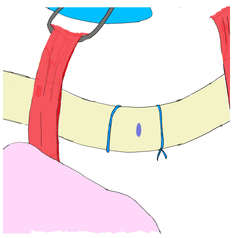

(i) Position of the retinal break with respect to the scleral buckle

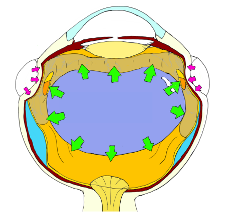

(j) Indentation of the diameter of the eye

Figure 1.8: Surgical drainage-procedure for scleral buckling. Source: Andrea Govetto

1.2.1 Volume displacement from the vitreous cavity

Even though the choice of a drainage or a non-drainage procedure is usually up to the experience of surgeons and to the single case, it is possible to estimate the amount of fluid to be drained and, consequently, of expanding gas to inject, through a mathematical model that predicts the intraocular volume displacement from the vitreous cavity. This displacement of fluid is determined by the application of the scleral buckle and causes a reduction in the volume of vitreous cavity. The mathematical model considers the intraocular volume displacement as a function of buckle size, position, height and circumference for a given axial length of the eye. The assumptions on which this model is based are the following:

- The vitreous cavity is a section of sphere
- The axial length of the eye is unchanged by the scleral buckle
- The scleral buckle width is measured from the equator
- The buckle makes an arcuate indentation in the sclera

It is to notice that the invariance of axial length is an approximation, since the presence of a scleral buckle, especially an encircling one, might induce variation in axial length. The formula to determine the displace volume V is the following:
$V = C \cdot (\frac{\pi}{360}) \cdot (2rh - h^2) \cdot (w_1 + w_2)$,
where C is the circumference of the buckle expressed in degrees, r is the internal radius of the eye (mm), h is the height of the buckle (mm) and w_1 and w_2 are the width of the buckle respectively anterior and posterior to the equator (mm). [4]

1.2.2 Variation of axial length of the eye

Circumferential scleral buckle may induce changes in the axial length of the eye, which, from a sphere, turns into a prolate spheroid. The result may be an increase or a reduction of axial length, depending on the buckle: at low to moderate buckle heights, the decrease in the circumference of the eye due to scleral buckle leads to an increase in the anteroposterior dimension of the eye; at very high buckle heights, invagination of the sclera around a broad encircling band with mattress sutures leads to a decrease in the axial length of the eye. A mathematical model is available to predict the axial length changes. This model is based on the following assumptions:

- The overall contour of the eye with a scleral buckle is an ellipse
- The circumference of the eye is constant

The formula to predict the axial length change is the following:
$P = 4a \cdot \int_0^{\frac{\pi}{2}} \sqrt{1 - (\sqrt{\frac{a^2-b^2}{a}})^2 \cdot \sin^2\theta d\theta}$

P is the perimeter of the eye-4, a=0.5(axial length of the eye), b=0.5(indented equator of ellipse). In Figure 1.9, changes in axial length due to indentation of diameter are shown. [5]

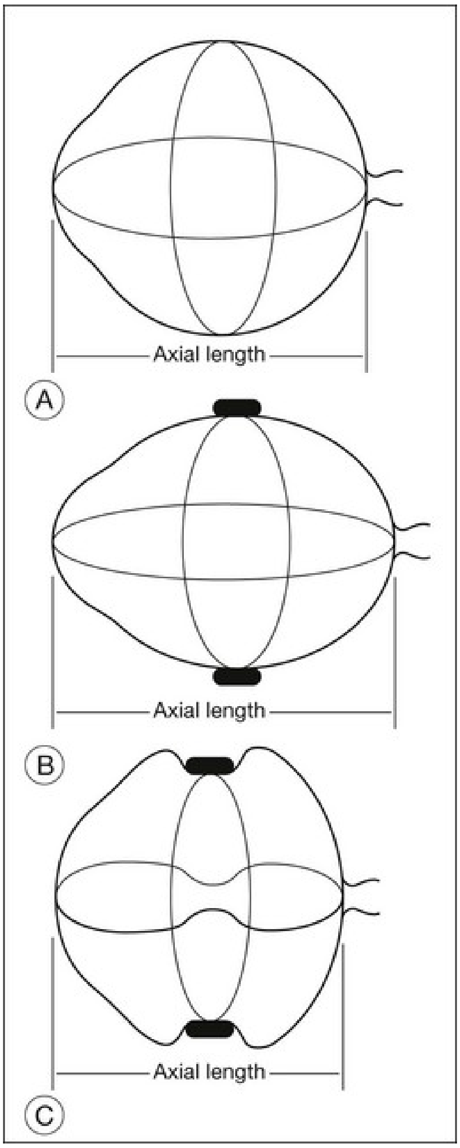

Figure 1.9: Variation of axial length in indented eye. Source: https://entokey.com/the-effects-and-action-of-scleral-buckles-in-the-treatment-of-retinal-detachment

1.2.3 Retinal folds

Moderate to high circumferential encircling scleral buckles may also cause radial folding of the retina. The circumferential scleral buckles cause a reduction in the normal circumference of the eye in the equatorial meridian and, since the sclera and the retina are unable to shrink to the smaller circumference, they may be thrown into radial folds. Moreover, if a radial fold bisects a retinal tear, the fishmouth phenomenon occurs. Figure 1.10 highlights both these mechanisms. [5]

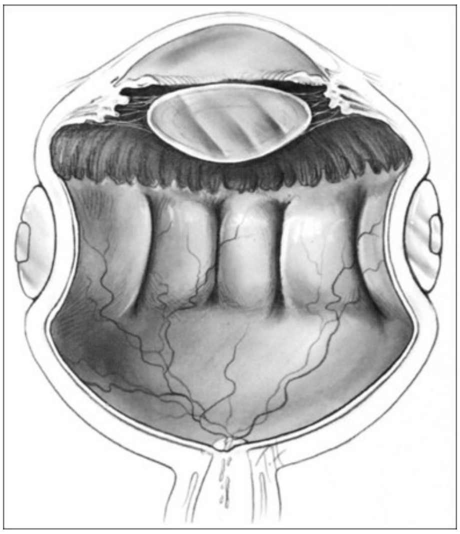

(a) Retinal folds due to scleral buckling

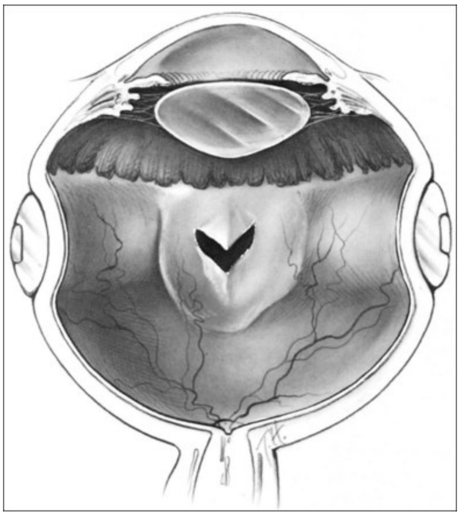

(b) Fishmouth phenomenon

Figure 1.10: Side effects of scleral buckling. Source: https://entokey.com/the-effects-and-action-of-scleral-buckles-in-the-treatment-of-retinal-detachment

Chapter 2

Kinematics of the eye

The purpose of this work is to simulate and evaluate the fluid dynamic behavior of the eye for different types, configurations, and locations of retinal breaks and following surgery.
In order to accomplish this purpose, it is necessary to impose the eye an adequate kinematic law, which takes into account the typical eye motion, such as saccadic eye movements and head movements. Saccadic eye movements are involuntary rotations of the eye around its vertical axis (which it will be referred to, later, as the z-axis); all these movements are similar, even among different subjects. Head movements, instead, embrace various kind of movements depending on the daily activities made by each subject, such as coughing, sitting down, walking and jogging.
It is difficult to know with certainty the impact of head movements on retinal detachment, with some studies tying to evaluate this contribution, such as [6], but without reliable results due to the use of several approximations and to the wide variety of head movements to be considered. On the other side, many studies have demonstrated the importance of saccadic movements as a contribution to retinal detachment, like [7]. Due to the lack of reliable results about the relevance of traction forces on the retina caused by head movements and to the impossibility to standardize this kind of movements, in this work saccadic eye movements only are taken into account to analyze loads acting on the retina. As a reference, the kinematic law defined in [7] was used, since it takes also into account implicitly head movements related to high saccade amplitude values.
A saccadic eye movement starts with a very high angular acceleration (up to 30'000° s^{-2}), followed by a less intense deceleration (capable of inducing an efficient stop to the movement) and, finally, a peak angular velocity rising in proportion to the saccades amplitude up to a saturation value (between 400 and 600° s^{-1}). It is possible to define a range of amplitude for saccades between 0.05° and 90°, which is to be considered as the physical limit for the orbit; as stated above, at very high values of saccades, head rotations are also involved. The quantities used to describe saccadic movements are the following: the saccade amplitude A, the saccade duration D, the peak angular velocity Ω_p and the acceleration time t_p, defined as the time

required to reach the peak velocity starting from rest. The relationship between saccade duration and saccade amplitude is accurately described by the linear law $D = D_0 + dA$, with 5°<A<50° , D expressed in seconds, $d \simeq 0.0025$ s·deg^{-1} and D_0 ranges between 0.02 and 0.03 s. Moreover, once the average angular velocity during a saccadic movement is defined as $\bar{\Omega} \equiv \frac{A}{D}$, the ratio between the peak and the mean velocities attains a fairly constant value, which is $\frac{\Omega_p}{\bar{\Omega}} \simeq 1.64$. Finally, from experimental data, it is shown that for small amplitudes of saccades the acceleration time t_p is approximately equal to 0.45D and that the dimensionless acceleration time $\frac{t_p}{D}$ varies linearly with increasing saccades amplitudes. According to [7], in the present work a fifth degree polynomial function is employed to reproduce the time law $\theta(t)$, since it represents the angular displacement of the eye during a saccadic movements accurately:
$\theta(t) = -(c_0 + c_0 t + c_2 t^2 + c_3 t^3 + c_4 t^4 + c_5 t^5)$
The six coefficients that appear in the law of motion can be determined by imposing the following constraints: $\theta(0) = 0$, $\theta(D) = A$, $\dot{\theta}(0) = 0$, $\dot{\theta}(D) = 0$, $\dot{\theta}(t_p) = \Omega_p$, $\ddot{\theta}(t_p) = 0$. [7] In Figure 2.1 and Figure 2.2 angular velocity and angular displacement are plotted, respectively, for different values of saccade amplitude.

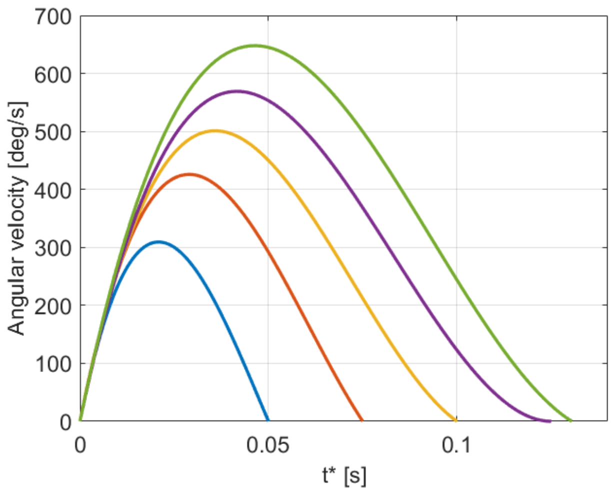

Figure 2.1: Angular velocity for saccade amplitudes of 10° (blue line), 20° (red line), 30° (yellow line), 40° (purple line) and 50° (green line). Source: [7]

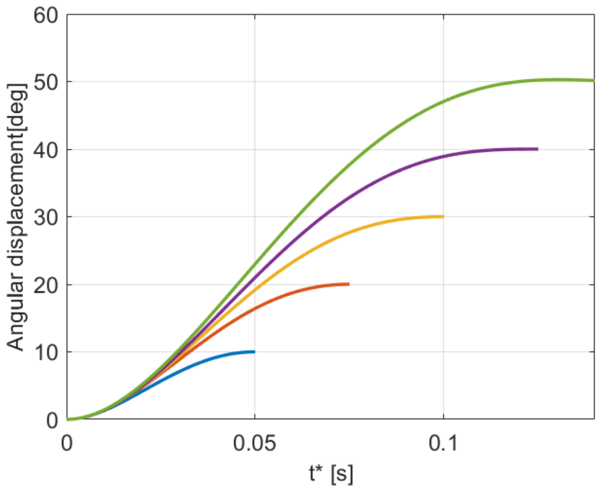

Figure 2.2: Angular displacement for saccade amplitudes of 10° (blue line), 20° (red line), 30° (yellow line), 40° (purple line) and 50° (green line). Source: [7]

For the purpose of this work, a value of $D_0 = 0.025$ s was chosen. In addition, a saccade amplitude of 30 degrees was selected; this amplitude is quite large, compared to those occurring more often - around 10°-, but its high value helps to more clearly assess the fluid dynamics during simulations due to the longer and wider eye movement. For this selected value of amplitude, the saccadic movement lasts for 100 ms.

Chapter 3

The FSI code

The kinematics of the eye, described in Chapter 2, generates a strongly three-dimensional flow of the liquified vitreous from the eyeball to the subretinal space. The hydrodynamic loads acting on the wet surface force the deformation and the motion of the detached portion of retina, whose tissues have nonlinear and anisotropic elastic properties.

Due to the complexity of this mechanism from a computational point of view, a multiphysics computational approach has been used. This approach allows to simulate simultaneously the elasto-mechanics and the fluid dynamics of the eye and their coupled interactions. This model has already been used and implemented successfully to simulate the very complex behaviour of a human heart, as explained in [8].

The model, for the purpose of this study, lies on two pillars: a fluid solver for the fluid dynamics of the liquefied vitreous evolving in a complex-geometry, deforming domain; a structure solver for the anisotropic hyperelastic biological tissues, where the dynamics is determined by both active tension and hydrodynamic loads. It is to mention, however, that, in real cases, the vitreous gel does not liquefy completely, but a biphasic fluid is contained in the vitreous chamber; for the sake of this work, a completely liquefied vitreous will be considered and this hypothesis and its consequent implications will be discussed in more detail later for individual case studies.

The fluid dynamics developing in the deformable shape of the eye is dealt with by an Immersed Boundary Method, which means that the whole geometry is placed in a Cartesian computational domain where the Navier-Stokes equations are integrated and the no-slip condition on all wet surfaces is imposed through body forces. The size of domain is l_x x l_y x l_z = 304 x 304 x 253 mm^3, discretized by a uniform mesh of 621 x 621 x 519 nodes corresponding to a grid spacing $\Delta = 4.83$ μm.

The characteristics of the two modules and their coupling are explained separately below.

3.1 Flow solver

Liquefied vitreous velocity $\mathbf{u}$ and pressure p are governed by Navier-Stokes and continuity equations for an incompressible, viscous flow:

$$\frac{\partial \mathbf{u}}{\partial t} + \mathbf{u} \cdot \boldsymbol{\nabla} \mathbf{u} = -\boldsymbol{\nabla} p + \boldsymbol{\nabla} \cdot \boldsymbol{\tau} + \mathbf{f}$$

$$\boldsymbol{\nabla} \cdot \mathbf{u} = 0,$$

where $\boldsymbol{\tau}$ is the viscous stress tensor, which, in this model, depends on the strain-rate tensor $\mathbf{E} = \frac{(\boldsymbol{\nabla}\mathbf{u}+\boldsymbol{\nabla}^T\mathbf{u})}{2}$ through a Newtonian constitutive relation, since the liquefied vitreous has very similar characteristics to those of the water. Accordingly, in this study, the linear constitutive relation $\boldsymbol{\tau} = \frac{2\mathbf{E}}{Re}$ has been used, thus imposing for the fluid the dynamic viscosity of the water $\mu = 1.065 \cdot 10^{-3}$ Pa·s and the density of the water $\rho^* = 1000$ kg/m^3. The Reynolds number, whose value $Re = 2482.986$ is computed through the relation $Re = U^* L^* \rho^*/\mu$, has been defined using the mean velocity $U^* = 0.115$ m/s and the reference length $L^* = 22.997$ mm, which is the max width of the eye.

The previously-mentioned governing equations are numerically solved using the AFiD solver based on central, second-order, finite differences on a staggered mesh for spatial discretization. As a matter of fact, the eye is placed in a Cartesian computational domain, where the no-slip condition on the wet surfaces is imposed using an Immersed Boundary Method (IBM) technique based on the moving least square (MLS) approach. Given the velocity field $\mathbf{u}^n$ and the pressure field p^n at time t^n, and the time step Δt, the provisional nonsolenoidal velocity field $\hat{\mathbf{u}}$ satisfies

$$\frac{\hat{\mathbf{u}} - \mathbf{u}^n}{\Delta t} = -\alpha \boldsymbol{\nabla} p^n + \gamma H^n + \rho H^{n-1} + \frac{\alpha}{2Re} \nabla^2 (\hat{\mathbf{u}} + \mathbf{u}^n),$$

where H incorporates the nonlinear terms and some volume forces, $\gamma = 3/2$, $\rho = -1/2$ and $\alpha = \gamma + \rho = 1$ are the coefficients of the Adams-Bashforth/Crank-Nicolson time advancement scheme.

The no-slip condition on wet surfaces is imposed at the Lagrangian markers uniformly distributed on the immersed boundaries and then transferred to the Eulerian grid points. The Lagrangian markers are placed at the centroids of the triangulated mesh, whereas the mass is concentrated at the nodes; as a matter of fact, a 3D support domain consisting of N_e=3 x 3 x 3 = 27 Eulerian nodes is created around each Lagrangian marker (as explained in Figure 3.1) and the fluid velocity therein $\hat{\mathbf{u}}(\mathbf{x}_b)$ is computed through interpolation using the velocity at the N_e Eulerian points of the support domain

$$\hat{u}_i(\mathbf{x}_b) = \sum_{k=1}^{N_e} \phi_i^k(\mathbf{x}_b) \hat{u}_i(\mathbf{x}_k),$$

where $\phi_i^k(\mathbf{x})$ are the transfer operators which depend on the shape functions used for the interpolation.

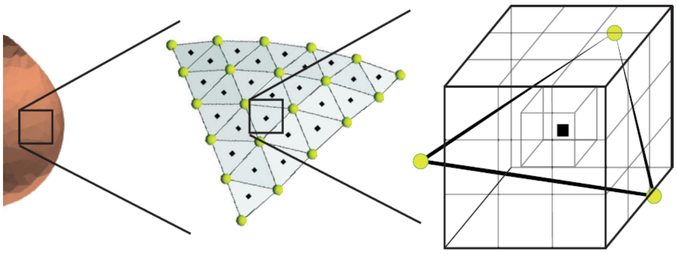

Figure 3.1: Immersed Boundary method for deformable tissues. From left to right, a generic wet surface, a triangulated mesh with the Lagrangian markers at its centroid and with the mass concentrated at the nodes, support domain around a Lagrangian marker. Source: [8]

Since, usually, the interpolated velocity does not match the velocity of the corresponding Lagrangian marker $\mathbf{u}_b(\mathbf{x}_b)$, their difference is therefore used to compute a source term $\mathbf{f}_b = [\mathbf{u}_b(\mathbf{x}_b) - \hat{\mathbf{u}}]/\Delta t$. This term is then transferred back to the Eulerian grid points as a distributed forcing $\mathbf{f}$. This procedure made by a relation similar the previous one and it is repeated for all Lagrangian markers. The resulting forcing field is used to update the provisional velocity $\hat{\mathbf{u}}$ as

$$\mathbf{u}^* = \hat{\mathbf{u}} + \Delta t \mathbf{f}$$

$\mathbf{u}^*$ is still a nonsoleinodal field, so it is projected into a divergence-free space by the following correction in the form

$$\frac{\mathbf{u}^{n+1} - \mathbf{u}^*}{\Delta t} = -\alpha \boldsymbol{\nabla} \Phi \Rightarrow \mathbf{u}^{n+1} = \mathbf{u}^* - \alpha \Delta t \boldsymbol{\nabla} \Phi$$

The scalar field Φ comes from the elliptic equation $\nabla^2 \Phi = \boldsymbol{\nabla} \cdot \mathbf{u}^*/(\alpha \Delta t)$, which also deals with the updated pressure through

$$p^{n+1} = p^n + \Phi - \frac{\alpha \Delta t}{2Re} \nabla^2 \Phi$$

Moreover, the projection step, which enforces the divergence-free condition for the velocity $\mathbf{u}^{n+1}$, lightly perturbs the field $\mathbf{u}^*$, satisfying the Immersed Boundary condition imposed in $\mathbf{u}^* = \hat{\mathbf{u}} + \Delta t \mathbf{f}$. It is to notice that the last two steps might be repeated iteratively in order to get a velocity $\mathbf{u}^{n+1}$ that complies with the solenoidal-condition and with the no-slip boundary-condition at the same time up to a given tolerance.

Pressure and viscous stresses are evaluated at the Lagrangian markers lying on the immersed body surface since hydrodynamic loads are needed as inupt for the structural solver.

Inside this work, two different types of structures, both 2D, are concerned: the eyeball surface and the retinal break surface, which will be treated in several different shapes later. As far as retinal breaks are involved, both surface sides are wet by the flow, and the local force at each triangular face $\mathbf{F}_f^{ext}$ is computed along positive $\mathbf{n}^+$ and negative $\mathbf{n}^- = -\mathbf{n}^+$ normal directions:

$$\mathbf{F}_f^{ext} = [-(p_f^+ - p_f^-)\mathbf{n}_f^+ + (\boldsymbol{\tau}_f^+ - \boldsymbol{\tau}_f^-) \cdot \boldsymbol{n}_f^+]A_f,$$

where A_f is the area of the surface. Regarding the surface of the eyeball, since it is a closed surface, hydrodynamic loads are computed on one side of the surface only, with the following relationship:

$$\mathbf{F}_f^{ext} = [-p_f\mathbf{n}_f + \boldsymbol{\tau}_f \cdot \boldsymbol{n}_f]A_f,$$

where $\mathbf{n}_f$ is the outward normal vector of the wet surface. The hydrodynamic loads, which have been evaluated at the baricentric Lagrangian markers, are then transferred to the triangle nodes according to

$$\mathbf{F}_f^{ext} = \frac{1}{3}\sum_{i=1}^{N_{nf}} \mathbf{F}_{fi}^{ext} A_{fi},$$

with N_{fi} the number of faces sharing the node n and $\mathbf{F}_{fi}^{ext}$ and A_{fi} hydrodynamic forces and surfaces of the ith face sharing of the node n.

In order to have the two-way transfer between Lagrangian and Eulerian grids, it is necessary that each grid cell crossed by the immersed boundary can be associated at least with a surface triangle. This means that the triangulation should be neither too fine nor too coarse to obtain a correct solution without wasting computational resources. It has been shown that a working compromise is to have a surface triangulation with equilateral triangles having edges of size ≈ 0.7 times the local grid spacing. Consequently, as the Eulerian grid is refined, also the Lagrangian resolution must be increased, which implies geometry remeshing for every change of Eulerian resolution. An adaptive Lagrangian mesh refinement procedure is used, so that the initial triangular mesh is automatically subdivided into virtual subtriangles, named "tiles", until each one gets smaller than the local Eulerian grid size, thus avoiding holes in the interfacial boundary condition. This procedure allows to discretize the retinal tissue independently of the Eulerian mesh and each triangle is successively refined until the Lagrangian resolution of the tiled surface is fine enough.

There are different possible tiling approaches; of these, the barycentric adaptive rule consists of splitting the triangles into three parts according to the medians passing through the centroid and higher Lagrangian resolution can thus be obtained by successive splitting of the subtriangles, according to the same procedure.

This rule has its own drawbacks, such as changes in the shape of triangles with respect to the initial triangle and esponential increase of the number of tiles with the tiling step. These drawbacks are mitigated by an adaptive quadratic tiling, where triangles are tiled by tracing a set of m-1 (with $m = 1, 2, 3, ...$) equispaced lines parallel to each triangle edge intersecting the other two; the number of tiles grows algebraically $N_{tiles} = m^2$ with the tiling steps m. In particular, this last

feature can be further improved through a combination of the quadratic tiling rule and the barycentric rule. Both strategies are used to split the triangles with the number of barycentric and quadratic steps, named b and m respectively, which can be varied independently so as to obtain the desired Lagrangian refinement.
This mixed rule provides a richer space of tiling configurations with the number of tiles growing slower than respect for other strategies. [8]

3.2 Structural mechanics

Even if the Cauchy-Poisson equation is generally used to solve the dynamics of deformable biological tissues, with appropriate constitutive relations, using finite-element or finite-volume method, the present problem implies large time-dependent displacements and deformations, so an alternative problem has been used.
The interaction potential method is very simple and it allows to treat both 2D and 3D structures. Regarding 2D structures, such as the eyeball and the retinal breaks concerned in this work, they are described by triangular elements and the mass is evenly distributed among the nodes, which are connected by elastic links. It is possible to describe the dynamics of the nth node through the second Newton's law of motion

$$m_n \frac{d^2 \mathbf{x}_n}{dt^2} = \mathbf{F}_n^{ext} + \mathbf{F}_n^{int},$$

with $\mathbf{x}_n$ the node position, $\mathbf{F}_n^{ext}$ and $\mathbf{F}_n^{int}$ the external and the internal, respectively, acting on each mesh vertex. External forces must be intended as hydrodynamic loads, which are nonzero only on the nodes located on wet surfaces, whereas internal forces depend on the material constitutive relation, but they can also include additional constraints.
As mentioned above, the eyeball concerned in this study is reduced to the thin layer of the retina and is modeled as a shell, whose internal stresses are computed using the 2D link network given by surface triangulation. The same happens for the retinal breaks, which, independently from their shapes, are treated as 2D structures.
For 2D structures, the mass is lumped at the nodes proportionally to the area of the triangles sharing a given vertex, so the mass m_n of the nth node is

$$m_n = \frac{1}{3} \sum_{j=1}^{N_n} \rho_j s_j A_j,$$

with ρ_j local density, s_j tissue thickness, A_j area of the triangular element and N_n number of triangles sharing the nth node.
The anisotropic hyperelastic material properties are accounted for by a Fung-type constitutive relation, for which the strain energy density can be written as

$$W_e = \frac{c}{2}(e^Q - 1),$$

where $Q = \alpha_f \epsilon_{ff}^2 + \alpha_s \epsilon_{ss}^2 + \alpha_n \epsilon_{nn}^2$ is a combination of the Green strain tensor components in the fiber (ϵ_{ff}), in the sheet (ϵ_{ss}) and in the sheet-normal (ϵ_{nn}) directions. As a matter of fact, biological tissues with fibers are stiffer in the fiber direction ($\hat{\mathbf{e}}_f$) than in the sheet ($\hat{\mathbf{e}}_s$) and sheet-normal ($\hat{\mathbf{e}}_n$) direction, with the stiffness increasing nonlinearly with the strain. This expression of Q is a general one including the cross terms of the Green strain tensor and, thanks to the assumption of pure axial loading, it can be simplified. This assumption implies that the nonnull second Piola-Kirchhoff stress tensor components in the three directions are $\boldsymbol{\tau}_{ff} = c\alpha_{ff} e^{\alpha_{ff}\epsilon_{ff}^2} \epsilon_{ff}$, $\boldsymbol{\tau}_{ss} = c\alpha_{ss} e^{\alpha_{ss}\epsilon_{ss}^2} \epsilon_{ss}$ and $\boldsymbol{\tau}_{nn} = c\alpha_{nn} e^{\alpha_{nn}\epsilon_{nn}^2} \epsilon_{nn}$. Moreover, it is found experimentally that $\alpha_{nn} = \alpha_{ss}$, which implies that the local axial stress of the mesh springs depends only on their inclination, ϕ, with respect to the local fiber direction. Consequently, the local stress within an edge inclined by ϕ with respect to the local fiber direction is computed as

$$\boldsymbol{\tau}_\phi = c\alpha_\phi e^{\alpha_\phi \epsilon_\phi^2} \epsilon_\phi,$$

with, due to the assumption of $\alpha_{nn} = \alpha_{ss}$, $\alpha_\phi = \sqrt{\alpha_{ff}^2 \cos^2\phi + \alpha_{nn}^2 \sin^2\phi}$. Figure 3.2 explains the constitutive relation for hyperelastic and orthotropic materials.

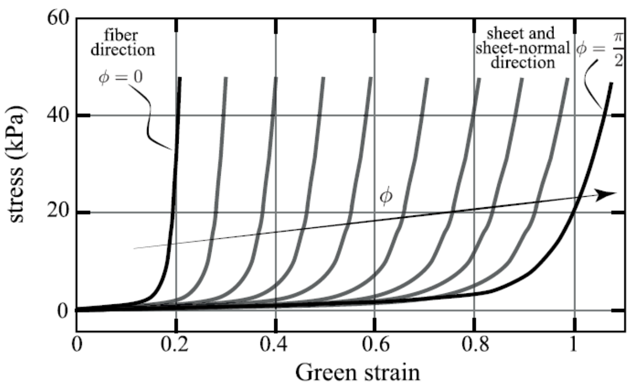

Figure 3.2: Hyperelastic and orthotropic constitutive relation as a function of the local inclination between the mesh edge and the fiber direction. Source: [8]

The strain ϵ_ϕ is the spring elongation relative to its instantaneous length , $\epsilon_\phi = (l - l_0)/l$, with l and l_0 the actual length and the stress-free length of the edge, respectively. The force exerted by the link connecting the nodes n and m is

$$\mathbf{F}_n^{el} = \boldsymbol{\tau}_\phi s \frac{A_{n,m}^{(1)} + A_{n,m}^{(2)}}{l_{n,m}} \frac{\mathbf{r}_n - \mathbf{r}_m}{l_{n,m}},$$

$$\mathbf{F}_m^{el} = -\mathbf{F}_n^{el},$$

where $\mathbf{r}_n$ and $\mathbf{r}_m$ are the position of the node n and m, respectively, and $A_{n,m}^{(1,2)}$ are the areas of the two triangles sharing the edge $l_{n,m}$. The term $\boldsymbol{\tau}_\phi$ is the stress, the term $s\frac{A^{(1)}_{n,m}+A^{(2)}_{n,m}}{l_{n,m}}$ indicates the tissue cross-sectional and the term $\frac{\mathbf{r}_n-\mathbf{r}_m}{l_{n,m}}$ is the force direction. The relation above accounts for the in-plane stiffness only, so an additional bending energy term is added to provide out-of-plane bending stiffness to the surfaces and to prevent them to wrinkle. The out-of-plane deformation of two adjacent triangles sharing an edge is then associated with an elastic reaction of a bending spring; its discretized bending energy, which involves four adjacent nodes, considering a surface with nonzero initial curvature in the stress-free configuration, can be written as

$$W_b = k_b[1 - \cos(\theta - \theta_0)],$$

with θ the angle between the normals of adjacent triangular faces of the tessellated surface and θ_0 the neutral angle of the stress-free configuration. The bending constant is $k_b = 2B/\sqrt{3}$, where $B = c\alpha_\phi s^3/[12(1-\nu_m^2)]$ is the bending modulus of a planar structure, s is the tissue thickness, $c\alpha_\phi$ is the equivalent Young modulus in the limit of small strain, depending on the Fung tissue properties, and $\nu_m = 0.5$ is the Poisson ratio of the material. The corresponding bending nodal forces, $\mathbf{F}^{be}_n$, can be obtained from the gradient of the bending potential W_b.
The total internal force of these 2D structures, at a given node, is given by

$$\mathbf{F}^{int}_n = \mathbf{F}^{el}_n + \mathbf{F}^{be}_n$$

This formulation of the internal force of the surfaces is used inside the second Newton's law written above to compute the time-dependent dynamics.

3.3 Model coupling

None of the two main models described above works independently from the other one, as each one relies on the result of the other as input. The integration of the second Newton's law needs the hydrodynamic loads and, on the other side, it is possible to handle Naver-Stokes' equations only once the fluid domain is known thanks to the structure model, which provides the actual tissues configuration.
For this work, a so-called "loose coupling" has been employed with a constant time step $\Delta t = 0.01$ ms; in this method, fluid is solved first, using the structure at the previous time step, and the consequent hydrodynamic loads are used to evolve the new structure.
It is to mention the importance of GPUs, whose usage has allowed simulations to run faster with respect to the CPU version of the code; the usage of a Nvidia's A100 GPU has permitted to run a campaign of simulation with different positions and types of retinal breaks, requiring 3.82 hours for each simultion.

Chapter 4

Retinal holes

typically

Retinal detachment is tipically the consequence of retinal tears originated from posterior vitreous detachment (PVD); on the other way round, retinal detachment without PVD is usually associated with either retinal dyalises or round retinal holes.
Round holes do not usually account for retinal detachment, but this consequence happens in a range of cases from 2 to 21%. Many studies have highlighted a predominance of retinal detachment arising from round holes in young myopic patients in comparison with patients with emmetrope eyes. For this reason, it has been considered of clinical relevance to evaluate the influence of fluid dynamics of liquefied vitreous in the evolution of retinal holes into retinal detachment.
There is a morphological difference between emmetrope and myopic eyes, which consists in a different axial length, major for myopic eyes. An emmetrope eye has an axial length from 23 to 24 mm, whereas the axial length of a myopic eye might overcome 30 mm. The elongation of the eye implies a stretching and a thinning of the retina, especially in the posterior section of the eye near the macula. It is not known whether this morphological difference plays an important role into the phenomenon of retinal detachment associated to retinal holes, or whether it depends on fluid dynamic loads. To fill the lack of certainties about this topic, this work has as purpose the quantification of fluid dynamic loads acting on a portion of retina slightly risen around a hole and the analysis of the contribution of this factor in the risks for progression to retinal detachment. [9]

4.1 Set-up of the problem

For the above-mentioned purpose, two different types of eye have been evaluated; consequently, two different models have been made thanks to the use of the software Rhinoceros.
These models represent an emmetrope and an highly myopic eye, with an axial length of 23.5 mm and 28.5 mm, respectively. Moreover, each model represents only the part of interest of the eye, consisting in the portion which surrounds the vitreous between the retina and the lens; consequently, these models don't include

the cornea and the lens. This simplification does not penalize the quality of this study, since those parts do not take part into the process of retinal detachment and they follow the eyeball during the saccade with a rigid motion. It is also to mention that the models for the emmetrope and for the myopic eye have coincident axes and origin, which implies that they rotate around the same z-axis. This might influence the results, but this choice was necessary to better understand the impact of fluid dynamics on retinal detachment with a limited number of variables, due to the complexity of this problem.
The hypothesis of a completely liquefied vitreous is made to proceed with this study, in order not to increase the computational effort required for the simulations of a biphasic fluid. Even though this is a strong hypothesis, it does not affect much results from the simulations, since retinal detachment consequent to retinal holes is not associated with posterior vitreous detachment. For this reason, vitreoretinal traction is involved in the genesis of the retinal hole, but it doesn't contribute to its evolution, which might depend on fluid dynamic loads or on the different characteristics or retinal tissue between emmetrope and myopic eyes. For each type of eye, 3 different sections along the y-axis (axis of symmetry) have been chosen, anterior to the equator, posterior to the equator and macular. The macula, instead, has been considered coincident with the posterior pole. For the emmetrope eye, the center of the anterior retinal hole has been set at a distance $h_1 = 4$ mm forward the equator in the direction of the axis, whereas the center of the posterior retinal hole is set $h_2 = 4$ mm behind the equator. These distances have been scaled for the myopic eye with a constant factor $\alpha = h/H$, where h is the distance of the center of the retinal hole from the forward end of the eye along the y-axis and H is the axial length of the eye. The value of α is 0.18 for the anterior hole and 0.6 for the posterior hole. Figure 4.1 and Figure 4.2 explain the measures that were taken as referrals for the various positions of holes in the emmetrope and the myopic eye, respectively.

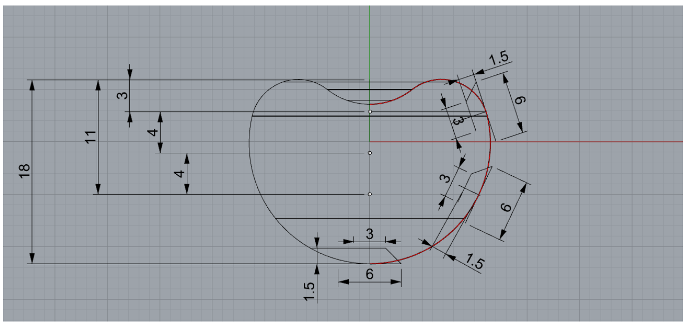

Figure 4.1: Referral measures for the emmetrope eye

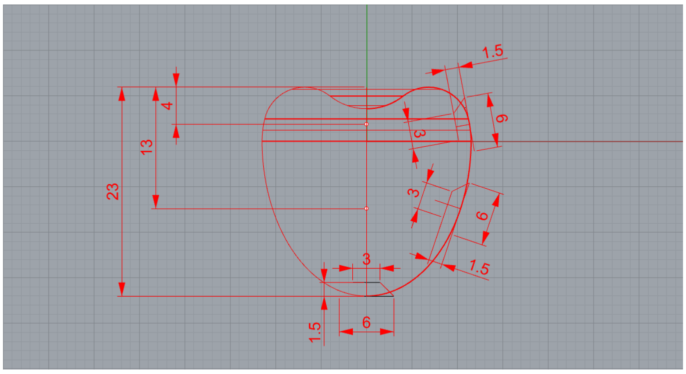

Figure 4.2: Referral measures for the myopic eye

For both the emmetrope and the myopic eye and for both the anterior and the posterior section, five different positions of the retinal hole have been considered, equally spaced of 45°, in the superior half of the eye. The 0° configuration consists of a retinal hole whose center intersects the xy plane passing through the center of the eye. It was chosen to only consider the superior half of the eye since the presence of the gravity force is not taken into account for this preliminary study and, consequently, due to the geometric symmetry of the eye with respect to the yx plane, no difference exists between the superior and the inferior half of the eye.
The choice of 5 different positions of the hole comes from the asymmetry of the kinematics; as a matter of fact, there is a geometric symmetry with respect to the yz plane, but the choice of analyzing one saccadic movement only, i.e. a rotation in one direction only, results in an asymmetry within the problem that is taken into consideration. On the other side, regarding the macular hole, it has one position only for each model, since it is located at the posterior pole.
It is to mention that, in human eyes, the dimensions of retinal holes might vary with their position along the axial length, with a smaller diameter for the macular holes and a consistently bigger diameter for anterior positions. For the sake of this study, only one dimension of the diameter is chosen, in order to reduce the number of parameters involved and to concentrate on the hydrodynamic loads only. For this reason, a retinal hole of diameter $d = 3$ mm is used for each model and for each position. This diameter is more realistic for the holes in anterior position, while it is less realistic for the posterior ones and, in particular, for the macular ones, whose average diameter is about 0.5 mm. Even thought this fact was taken into consideration when the problem set-up was made, the bigger dimension of diameter has been chosen in first approximation for the sake of computational costs and a further work might be done to analyze more realistic dimensions. Moreover, in order to analyze the fluid dynamic loads acting on the retina and responsible for a possible progressive detachment in absence of other external loads, a raised portion of the retina around the hole was created, with a conic shape, 45° angle of inclination and 1.5 mm of lift; the value of the initial angle of inclination is in accordance with those from clinical studies.

The positions of the retinal holes anterior to the equator, posterior to the equator and macular in an emmetrope eye are shown in Figure 4.3, Figure 4.4 and Figure 4.5 respectively, whereas the same positions in the myopic eye are shown in Figure 4.6, Figure 4.7 and Figure 4.8 respectively.

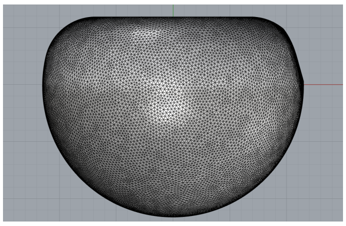

(a) Retinal hole at 0°

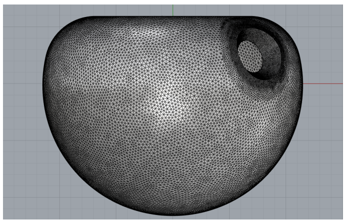

(b) Retinal hole at 45°

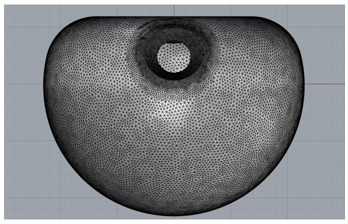

(c) Retinal hole at 90°

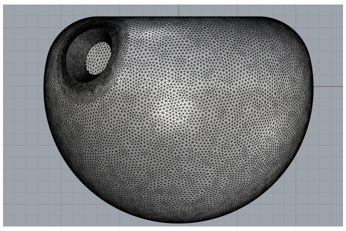

(d) Retinal hole at 135°

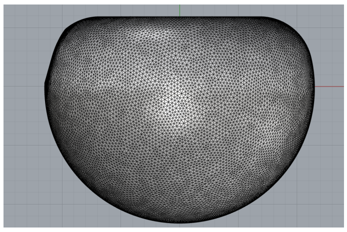

(e) Retinal hole at 180°

Figure 4.3: Positions of the retinal hole anterior to the equator in an emmetrope eye

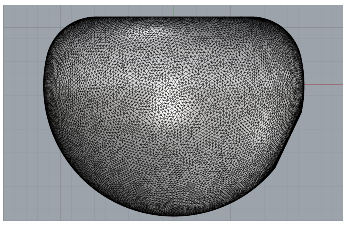

(a) Retinal hole at 0°

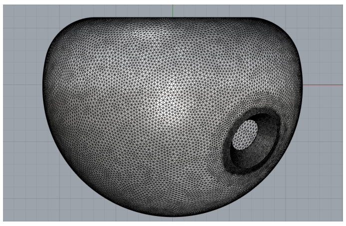

(b) Retinal hole at 45°

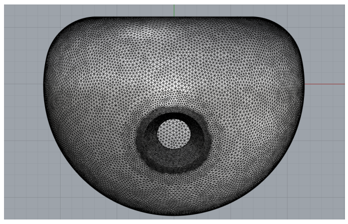

(c) Retinal hole at 90°

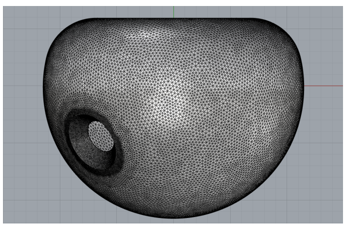

(d) Retinal hole at 135°

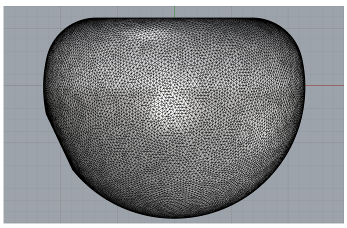

(e) Retinal hole at 180°

Figure 4.4: Positions of the retinal hole posterior to the equator in an emmetrope eye

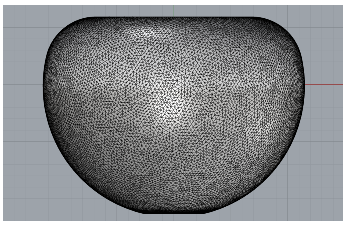

potresti indicare con una freccia o simile dov'è il macular hole

Figure 4.5: Macular hole in an emmetrope eye

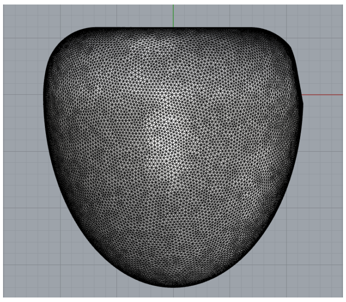

(a) Retinal hole at 0°

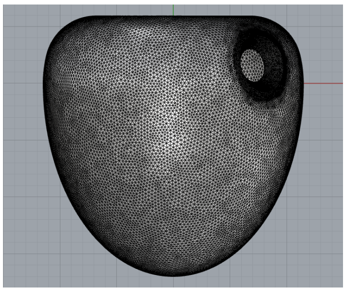

(b) Retinal hole at 45°

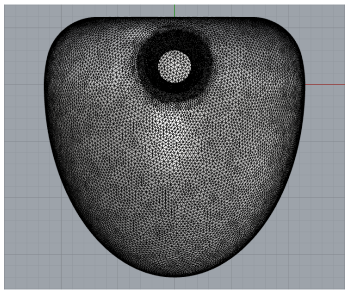

(c) Retinal hole at 90°

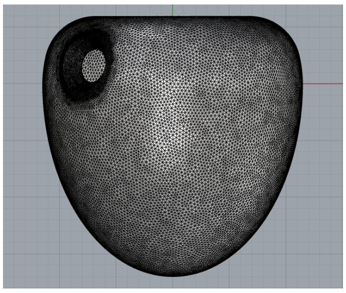

(d) Retinal hole at 135°

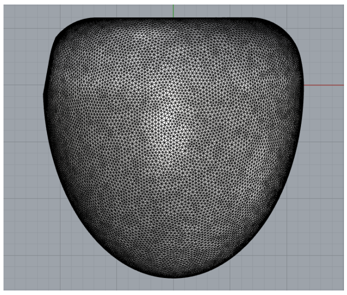

(e) Retinal hole at 180°

Figure 4.6: Positions of the retinal hole anterior to the equator in a myopic eye

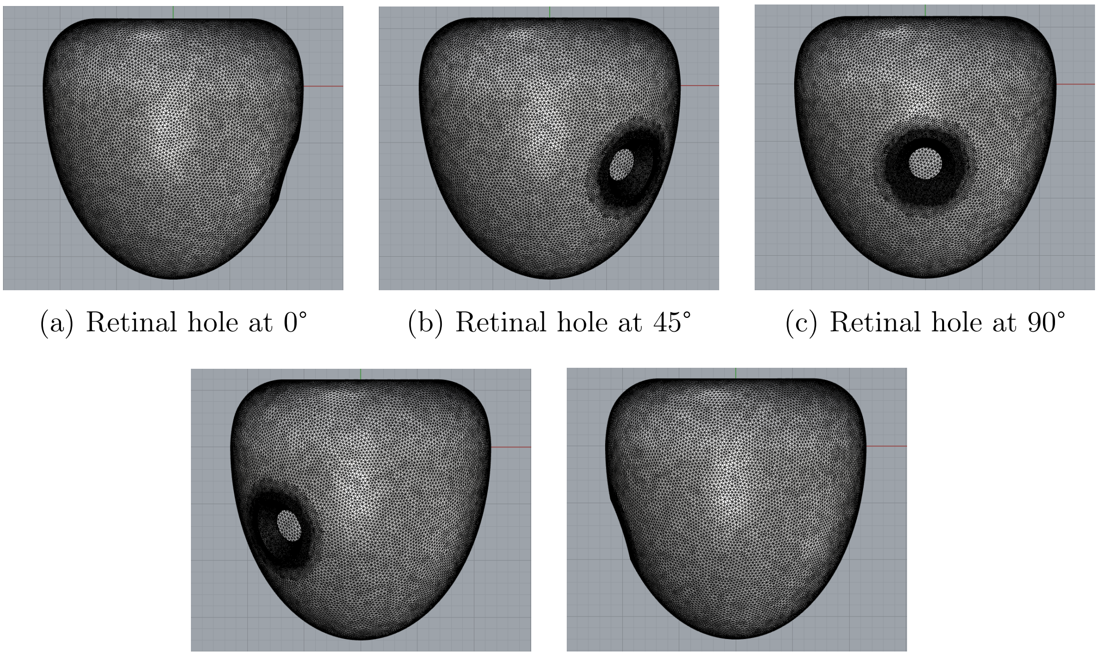

(a) Retinal hole at 0° (b) Retinal hole at 45° (c) Retinal hole at 90°

(d) Retinal hole at 135° (e) Retinal hole at 180°

Figure 4.7: Positions of the retinal hole posterior to the equator in a myopic eye

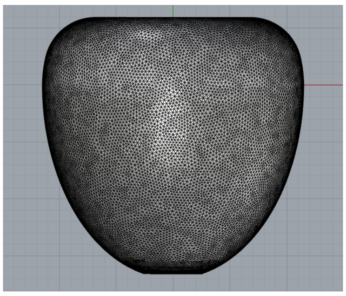

Figure 4.8: Macular hole in a myopic eye

per info, potresti indicare il range di t, anche se hai scelto t=0.22mm

In accordance with many experimental and computational studies about eyes, a realistic value of Young's Modulus has been selected for the retina, $E_1 = 1$ kPa [10]. The thickness of the retina has been set at a value of $t = 0.22$ mm, which is in line with the values reported in literature, as [6]. In fact, the retinal thickness varies along the axial length, but, as before, to reduce the number of free parameters, it was chosen to have one value of thickness only, which is reasonable, since the spacial thickness variation of the retina is known to be small.
Since the purpose of this work concerns the study of fluid dynamic loads acting at the edge of the raised retina for each type of eye and each position of the retinal hole, it was necessary to create two different CAD models, one for the choroid and the other one for the holed retina with lifted surface. These two models only differentiate for the part of the hole; the surfaces in common between the retina and the choroid are exactly the same and have coincident nodes; this fact makes

it easier to set-up the problem for simulations and it also allows further studies about the progression of detachment under fluid dynamic loads. The nodes on the choroid undergo the imposed kinematics described in Chapter 2; regarding the holed retina with a hole
retina, all of the nodes coincident with those on the choroid have the same imposed kinematics as above; the nodes on the raised portion of retina, instead, are free to move consequently of the fluid dynamics. This kinematic constraint imposed on the nodes at the edge of the retinal hole causes the lifted retina to be clamped. Due to this constraint it is possible to calculate the constraining reactions, equal and opposite to the fluid dynamic loads, and the peeling stresses they generate and that can lead to a disconnection of those nodes. Figure 4.9 shows the two different models for the choroid and for the holed retina in case of an emmetrope eye with an anterior hole.

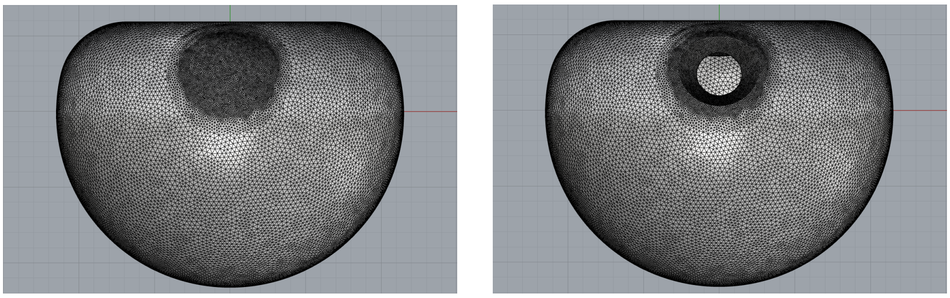

(a) Model for the choroid (b) Model for the holed retina

Figure 4.9: Models for emmetrope eye with anterior hole

4.1.1 Detachment criterion

In order to evaluate the importance of fluid dynamic loads acting at the edge of the retinal hole, it is necessary to compare their values, for each case, to a referral one. For this reason, a detachment criterion is imposed, both for comparison with the values obtained from simulations and for a further 3D analysis of the progressive detachment.

For this purpose, [11] gives the most accurate description of mechanics of retinal detachment and offers a valid and simple detachment criterion, which is easily applicable to this work. In spite of its easiness of comprehension, this study is based on a detailed description of biological features of the retina. As stated in Chapter 1, the basic forces related to retinal detachment are pressure-driven flows, active RPE pump flows, cell-cell adhesion forces and retinal tension forces. As mentioned before, for the purpose of this study, retinal tension forces are not considered since the vitreous humor is treated as completely liquefied. Moreover, details of the retina are not taken into account and the retina is reduced to a thin layer. Even if this assumption is coherent with the grade of approximation necessary for this work, more details might be considered when it comes to detachment criteria. As a matter of fact, in absence of hydraulic forces, it is possible to define the cellular adhesion potential $U(z)$, where z is the separation between the retina and the RPE; $z = 0$ is the equilibrium adhesion bond length between apposed retina and RPE cells, corresponding to the minimum of the potential. Consequently, the adhesive stress between two cell layers is defined as $\sigma(z) \equiv \frac{dU(z)}{dz}$ for $z < z^*$, which corresponds to the maximum separation sustainable for the tissue. The maximum yield stress that can be sustained by the cell layers can be approximated to $\sigma_{max} \sim U^*/z^*$. In Figure 4.10 $U(z)$ and $\sigma(z)$ are represented.

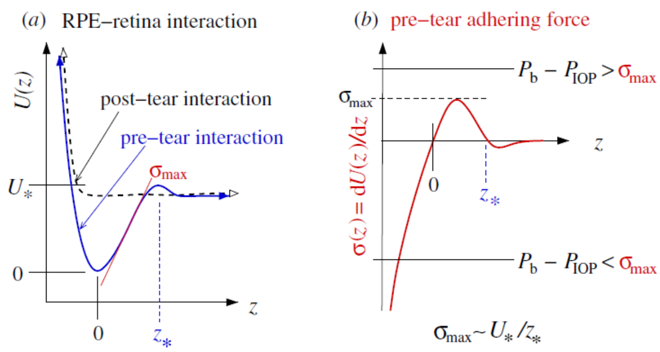

Figure 4.10: Adhesive energy per area U(z) between retinal layer cells and RPE, uniformely separated by a distance z (a), and the adhesive stress (force per area) $\sigma(z)$ between the two cell layers. Source: [11]

As stated above, cellular adhesion is not the only force involved in retinal detachment. As a matter of fact, from an anatomically-detailed point of view, pressure-driven fluid flows across the different tissue layers are also implied in the generation of forces. In [11], different pressures are considered:

- P_c is the fluid pressure in the choriocapillaris, related to the venous blood pressure
- P_{IOP} is the intraocular pressure of the vitreous humor, controlled by the total flow of vitreous humor
- P_b is the fluid pressure in the narrow extracellular space between the RPE and retina, containing the adhesion bonds

Both P_c and P_{IOP} are known parameters that can be determined from measurements and their difference is about $\Delta P \equiv P_c - P_{IOP} \simeq 5 - 10$ mm Hg; on the other way round, P_b depends on the fluid flow through the choroid and retinal layer. It is possible to define the volume fluxes J_c and J_r, where $J_c = L_c(P_c - P_b)$ and $J_r = L_r(P_b - P_{IOP})$, with L_c and L_r the effective hydraulic conductivities of the choriocapillaris and the retina, respectively; these parameters depend on the physiological state of the tissues. Moreover, since the physiological state of the RPE is important for this model, the pressure-independent parameter J_p is introduced; J_p depends on the state of the RPE cells and the regulation mechanisms of the pumps;

the RPE

as a matter of fact, RPE cell layer is fundamental to pump fluid from the retinal space through Bruch's membrane and back into the choroid.
From a mechanical point of view, as far as the stability of attached retina is concerned in the presence of fluid flow, it is necessary to satisfy the following relation:
$J_c = J_r + J_p$
This relation means that, for the static equilibrium, the volume flow into the subretinal space equals the flow out of it. By replacing the terms above with their expressions, it is possible to define the adhesion force $\sigma(z)$ as a function of the hydrodynamic pressure difference $P_b - P_{IOP}$, which tends to separate the retina from the RPE:
$P_b - P_{IOP} = \frac{L_c \Delta P}{L_r + L_c} - \frac{J_p}{L_r + L_c} = \sigma(z) \equiv \frac{dU(z)}{dz}$
This equation can be solved to find the cellular layer separation z as a function of ΔP, J_p, L_r and L_c. Depending on the sign of ΔP, two different cases can be differentiated:

- if $\Delta P < 0$, the retina is compressed onto the choroid by the outward passive flow and only negative values of $\sigma(z)$ can satisfy the equation; in this case, a detachment can only occur under external traction forces from the vitreous humor;
- if $\Delta P > 0$ and it is sufficiently large and/or J_p is sufficiently small, a new equilibrium separation might be obtained for $z < 0$ due to the fluid pressure; in this situation, if $\Delta P > max\{dU(z)/dz\} \equiv \sigma_{max}$, no value of z can satisfy the equation and the retina is irreversibly detached from the RPE.

Figure 4.11 shows the latter situation ($\Delta P > 0$) both in case of stability of the retina (Case (a)) and in case of overcoming of the yeld stress and consequent delamination of the cell layers (Case (b)).

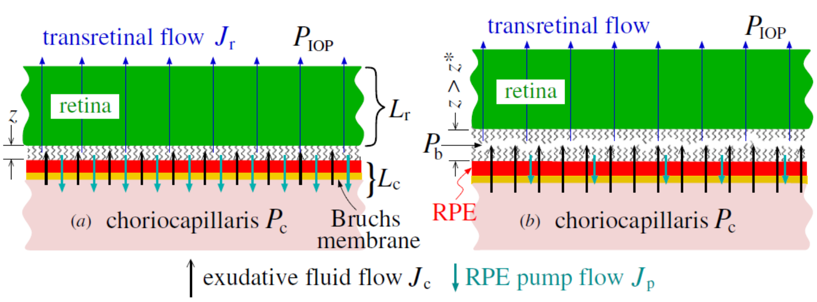

Figure 4.11: Representation of pressures and flows acting between the choriocapillaris and the retina. Case (a) shows an active pumping of the RPE and a retinal stability against delamination with $P_c > P_b > P_{IOP}$. Case (b) shows a situation where P_c has increased and/or J_p has decreased, implying accumulation of fluid at the retina-RPE interface and detachment. Source: [11]

According to [11], the resulting values of z* and U*, at which a spontaneous uniform delamination occurs, are $z^* \sim 10^{-7}$m and $U^* \leq 10^{-4}$ Jm^{-2}; it is to notice that this small value of U* is due to the fact that, in absence of vitreoretinal traction, loss of RPE function alone is not sufficient to determine a large scale delamination.

Many ~~During years, m~~any studies have been made to estimate the adhesion force between retina and RPE both experimentally and numerically; as far as experimental studies are concerned, many techniques have been used, such as peeling off the retina from the RPE mechanically to estimate the required force for detachment or pumping a solution in the subretinal space to evaluate the pressure, but every technique has its own drawbacks and no approach can be considered completely reliable. On the other hand, many studies have showed results comparable to those obtained in [11] and the theoretical explanation behind it makes it eligible as a reference for this work. For this reason, in order to evaluate the severity of the selected configurations of retinal holes in emmetrope and myopic eyes in this paper, a reference value of $\sigma_{max} = 1$ kPa is used. For each eye and for each position of retinal holes, a peeling stress σ_{peel} is calculated at the edge of the hole and it is compared to this reference value, in order to identify those configurations which are likely to lead to retinal detachment and to define the worst case scenario.

4.2 Building up the eye models

In this section, the creation of the eye models is discussed. The execution is the same for the emmetrope and for the myopic eye; the latter is created from the sketch of the emmetrope eye by replacing the posterior part with a portion of ellipse. In Figure 4.12, the red line indicates the myopic eye, while the yellow line indicates the emmetrope eye.

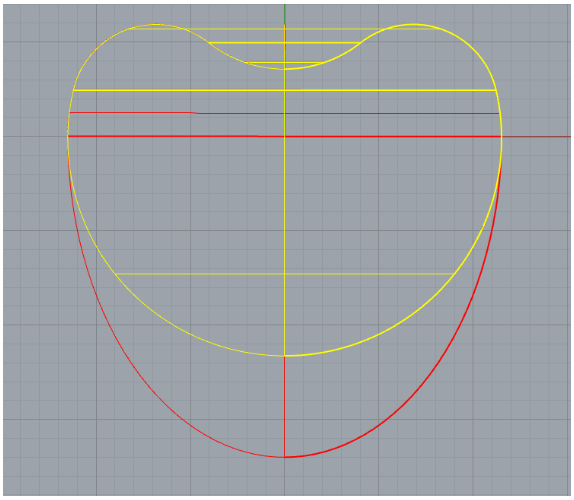

Figure 4.12: Sketch of the myopic and the emmetrope eye

Since a model for the choroid and a model for the holed retina are needed with coincident nodes in the portions they have in common, firstly the model for the retina is created and, later, the one for the choroid is made from the first one. Regarding the retina, it is made as an eye surface which intersects a conic surface, representing the retina hole with lifted surface around it. The creation of the models begins with the revolution of half the above sketch around the y-axis through the command "Revolve" to create a surface of revolution for the retina. In this section, images will refer to the case of holes in anterior position only, but the same procedure has been applied to the other positions. After creating the surface of retina, the sketch for the raised portion of retina is drawn. In order to do that, 3 different lines of construction are needed: two parallel to each other and one perpendicular to the other two and passing through their middle points. So, a first line, 6 mm long, is drawn through the command "Line: tangent from curve" where the curve is the contour of the eye surface in the position of interest and the point of tangency is the middle point of the line. As a reference, a second line, perpendicular to the first one and passing through its middle point, is drawn with the command "Line: perpendicular from curve". Using, once again, the command "Line: perpendicular from curve", the third line, parallel to the first one, is drawn, at a distance of 1.5 mm. Once these three construction lines have been drawn, a line of conjunction between the extremities of the two parallel ones is made. This one, which will be a little longer than expected for practical reasons, will be used to create the surface of rotation for the detached retina, whose sketch is a trapezoid with minor base $d_1 = 3$ mm and angle of 45 degrees. Construction lines and their dimensions are represented in Figure 4.13 for both the emmetrope and the myopic eye. It is to notice that, for each type of eye and for both the anterior and posterior position of the retinal hole, only the model at zero degree is drawn, since the other ones are obtained through a rotation of the meshes around the y-axis.

the retina

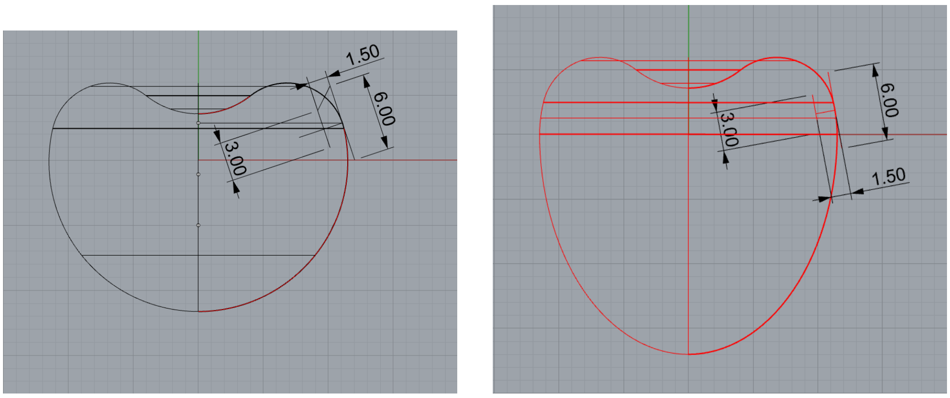

(a) Emmetrope eye (b) Myopic eye

Figure 4.13: Models for emmetrope and myopic eyes with anterior hole

After the cancellation of the two parallel lines, through the command "Revolve" a surface of revolution is made from the oblique line around the perpendicular line drawn previously. This way, the conic surface representing the lifted portion of retina intersects the surface of the retina. In order to create the hole surrounded by the lifted retina, it is necessary to remove that part of the surface. This part will be rebuilt later for the choroid model in order to have coincident nodes at the border. For this reason, the command "Split" is used with the cone as a cutting tool to cut the surface of the retina and the portion inside the cone is cancelled; successively, the command "Split" is used once again, with the surface of the retina as a cutting tool, to cut the exceeding portion of the cone. The so-obtained surfaces are joined through the command "Join" and the result is represented in Figure 4.14.

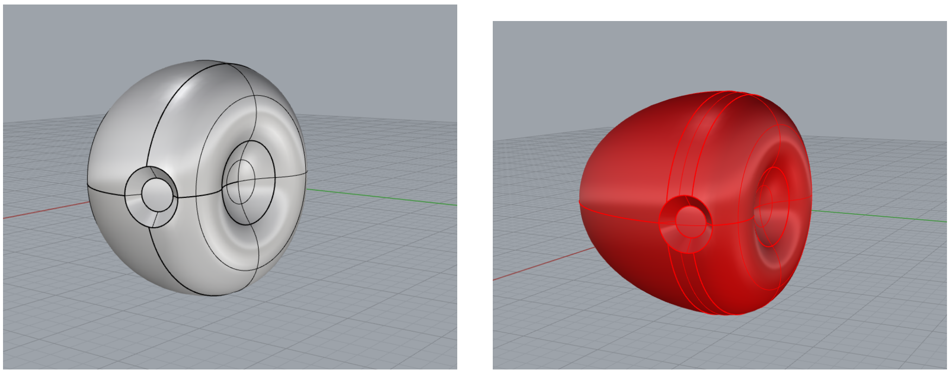

(a) Emmetrope eye (b) Myopic eye

Figure 4.14: Emmetrope and myopic eye with lifted retina

To create a quadrangular mesh, the command "Mesh from surface/polysurface" is applied on the surface, as shown in Figure 4.15, and then the surface below is removed and the quadrangular mesh is turned into a triangular one through the command "Triangulate mesh" (Figure 4.16).

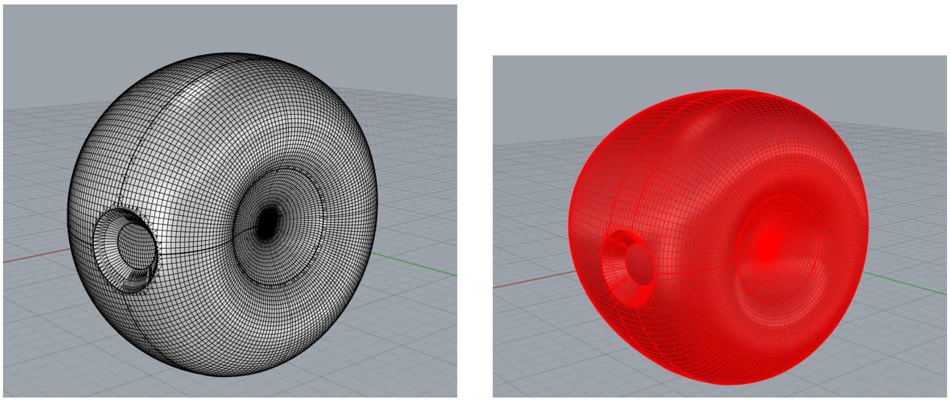

(a) Emmetrope eye (b) Myopic eye

Figure 4.15: Quadrangular mesh on the emmetrope and on the myopic eye

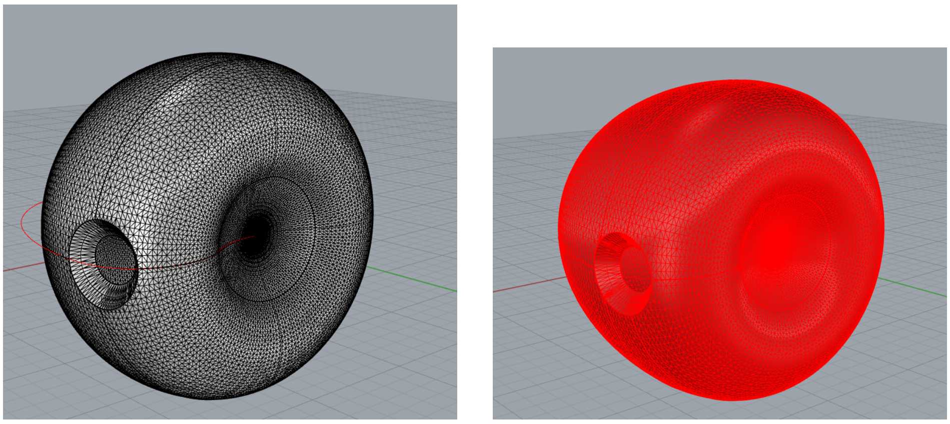

(a) Emmetrope eye (b) Myopic eye

Figure 4.16: Triangular mesh on the emmetrope and on the myopic eye

In order to obtain a more uniform mesh, it is imported on MeshLab, where the filter "Remeshing: isotropic explicit remeshing" is applied, with a number of ten iterations and a target length of 0.1. Consequently, as far as the retinal hole in anterior position is concerned, after this step, the emmetrope eye has 357'356 faces and 178'730 nodes, while the myopic eye has 400'744 faces and 200'438 nodes. Figure 4.17 shows the two models after this initial remeshing.

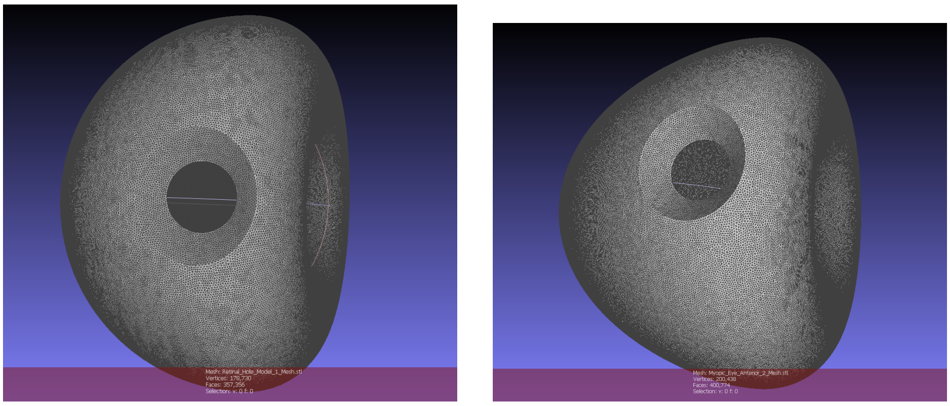

(a) Emmetrope eye (b) Myopic eye

Figure 4.17: Refined mesh on the emmetrope and on the myopic eye

It is to notice that the mesh above is more refined than needed and it will be loosened in Meshmixer in the areas far enough from the retinal hole. The portion including the risen retina and around it needs to be very finely meshed, since it is the portion of interest for this work and a sufficiently refined discretization is needed to understand the fluid dynamic phenomena around the hole. For this reason, a remeshing is done on Meshmixer, after closing the hole for practical purpose, in order to keep the mesh near and on the raised retina fine and to loosen the rest. The resulting meshes are shown in Figure 4.18, Figure 4.19 and Figure 4.20 for the anterior, posterior and macular position of the retinal hole, respectively, while 4.1 reports the number of nodes and faces for each model of the retina.

Eye type	Position of the hole	Number of nodes	Number of faces
Emmetrope	Anterior	23'769	47'434
Emmetrope	Posterior	23'937	47'768
Emmetrope	Macular	23'179	46257
Myopic	Anterior	26'379	52'656
Myopic	Posterior	27'356	54'611
Myopic	Macular	26'610	53'123

Table 4.1: Number of nodes and faces for models of the retina

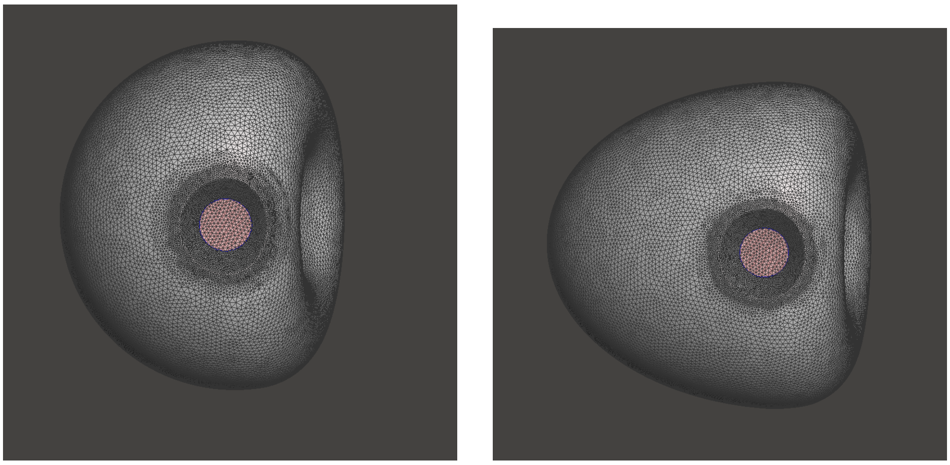

(a) Emmetrope eye (b) Myopic eye

Figure 4.18: Final mesh on the emmetrope and on the myopic eye with retinal hole in anterior position

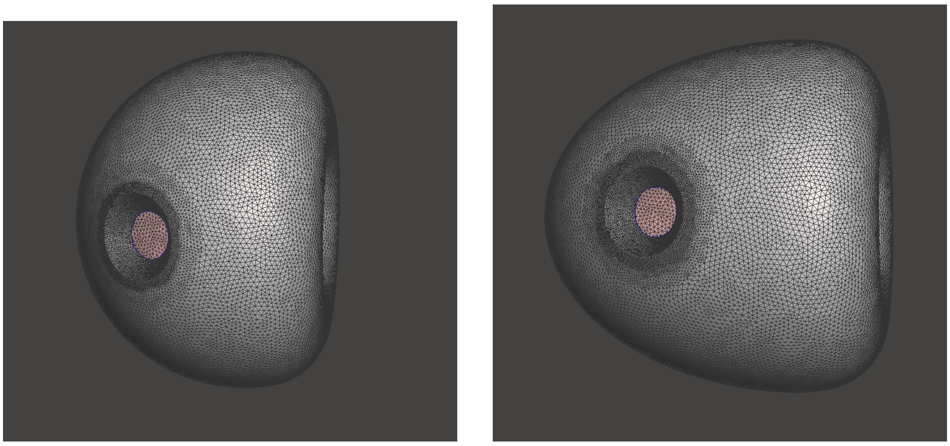

(a) Emmetrope eye (b) Myopic eye

Figure 4.19: Final mesh on the emmetrope and on the myopic eye with retinal hole in posterior position

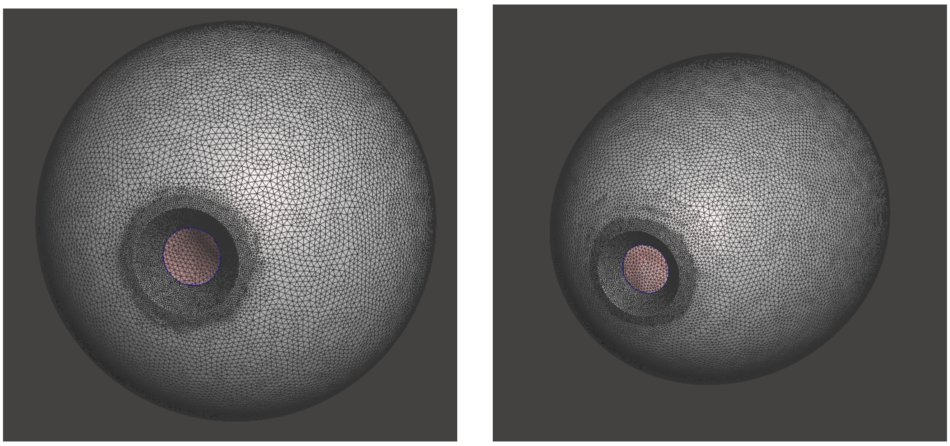

(a) Emmetrope eye (b) Myopic eye

Figure 4.20: Final mesh on the emmetrope and on the myopic eye with retinal hole in macular position

As stated before, it is necessary, for each type of eye and each position of the lifted retina, to create a model of the choroid, whose nodes are coincident with those of the retina in the portions they have in common. For this reason, the model for the choroid is built from that of the retina through a reconstruction of the holed portion of mesh. In order to do that, the portion of the cone must be removed from the models above and the hole must be filled thanks to the function "Inspector" on Meshmixer. This function fills the hole with a flat surface, consequently it will be necessary to recreate the curvature of the choroid. To do so, the holed retina and the filled hole are saved separately and the filled hole is joined with the cone. This passage is fundamental in order to maintain the nodes at the border of the surface, since it will be joined to the holed retina once the curvature is made. This new surface is imported in Meshmixer and the command "Attract" is applied to the filled surface only, by using the healthy eye as a magnet. Later, the cone is removed and the curved surface is joined to that of the holed retina to create a healthy choroid. Figure 4.21, Figure 4.22 and Figure 4.23 show the choroid in the retinal hole emmetrope and myopic eyes obtained to match with that of the holed retina in anterior, posterior and macular position, respectively.

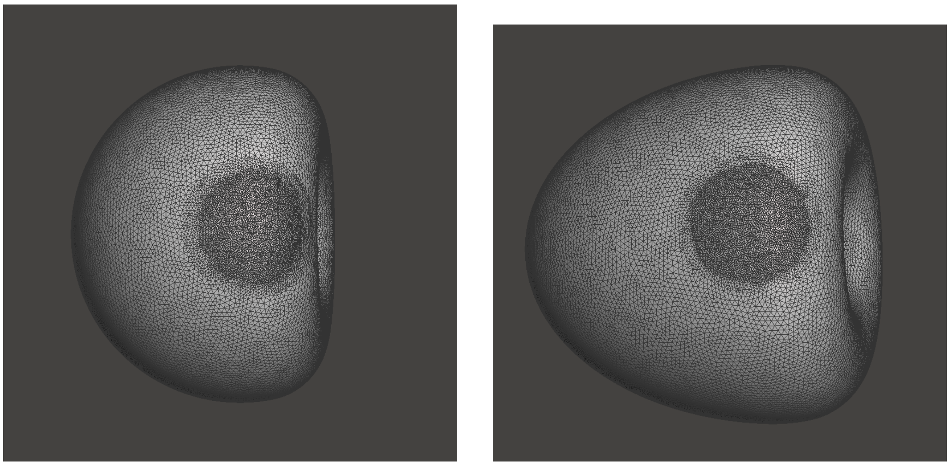

(a) Emmetrope eye (b) Myopic eye

Figure 4.21: Healthy choroid in emmetrope and myopic eye - anterior position of the detachment

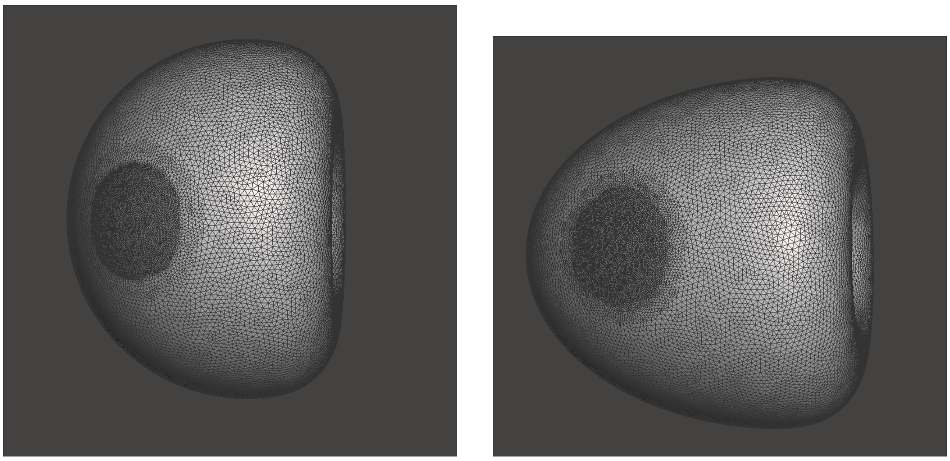

(a) Emmetrope eye (b) Myopic eye

Figure 4.22: Healthy choroid in emmetrope and myopic eye - posterior position of the detachment

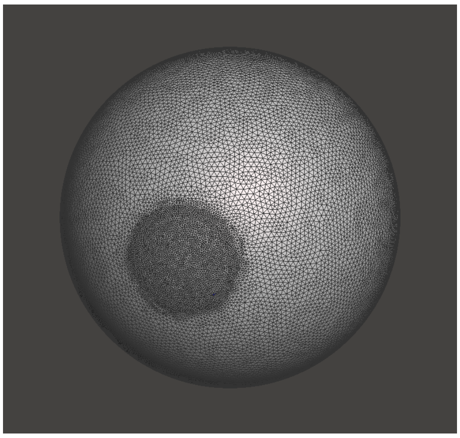

(a) Emmetrope eye

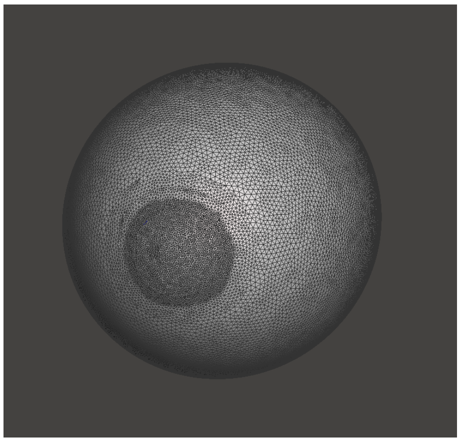

(b) Myopic eye

Figure 4.23: Healthy choroid in emmetrope and myopic eye - macular position of the detachment

4.3 Results

In this section, the results obtained from simulations, in terms of maximum peeling stress σ_{peel}, are graphed for every type of eye and position of the holes. In particular, results for each angle at which the retinal hole is positioned is directly compared between the emmetrope eye and the myopic eye, in order to immediately evaluate the worst scenarios. Results have been gathered into six different configurations depending on the angle at which the retinal holes is located with respect to the xy plane passing from the center of the eyes: at 0°, 45°, 90°, 180°; the last group concerns macular holes only. This division was made since at the same angle similar factors influence the results, while they may differ between different angles. Simulations were run for a time $t = 2T$, with T being the period discussed in Chapter 2. The results will be further discussed in the following section, in accordance with the group divisions adopted here. It is to mention that each model reaches its maximum stress at a different time, which will be reported in the tables above; for this reason, figures representing deformations are taken, for each model, at the time (and rotation) corresponding to the maximum peeling stress indicated in the graphs. Moreover, for each group of results taken into account, the configuration
Figure 4.24 shows the maximum peeling stress acting at the edge of retinal holes for the groups with retinal holes at 0°, in anterior and posterior positions. As it is possible to understand from the figure, for both the anterior and the posterior position of the hole, the myopic eye is more penalized than the emmetrope one. Moreover, for this group of configurations, the myopic eye with posterior retinal hole is the one that undergoes the heaviest peeling stress, while the emmetrope eye with retinal hole in anterior position undergoes the lightest stress. Table 4.2 sums up the results obtained for the configurations at 0°, while Figure 4.25 shows the maximum deformations for the different cases.

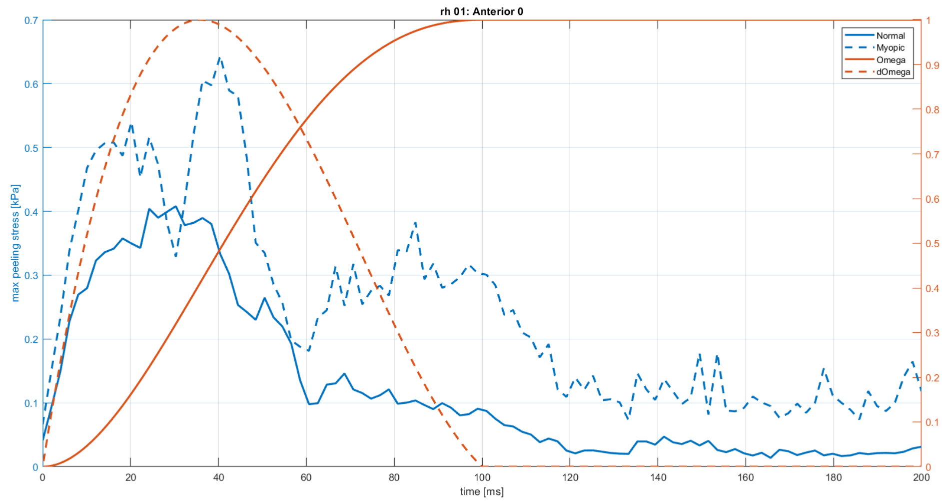

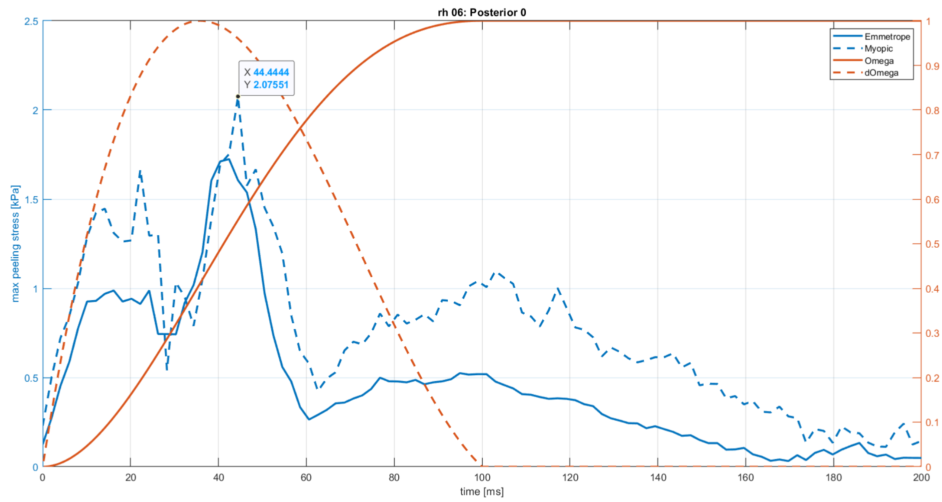

Figure 4.24: Peeling stress acting at the edge of retinal holes in anterior and posterior position for 0°.

Eye type	Position of the hole	σ_{peel} (kPa)	Time of maximum stress (ms)
Emmetrope	Anterior	0.41	30.00
Myopic	Anterior	0.64	40.00
Emmetrope	Posterior	1.72	42.4
Myopic	Posterior	2.00	44.4

Table 4.2: Peeling stress for configurations at 0°.

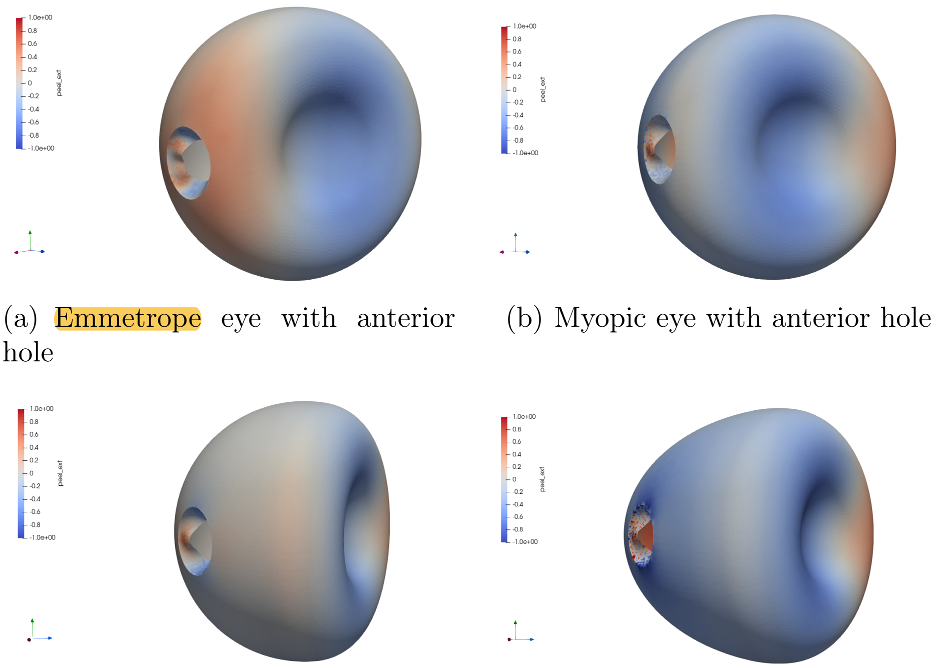

(a) Emmetrope eye with anterior hole

(b) Myopic eye with anterior hole

(c) Emmetrope eye with posterior hole

(d) Myopic eye with posterior hole

Figure 4.25: Maximum deformations occurring for eyes with retinal holes at 0°

As far as the group with retinal hole at 45° is concerned, the corresponding results are showed in Figure 4.26. Results for this group have a similar trend as those for the group at 0°. Consequently, the most critical case is that of the myopic eye with posterior hole, while the less penalized one is that of emmetrope eye with anterior hole, as reported in Table 4.3. Maximum deformations are shown in Figure 4.27.

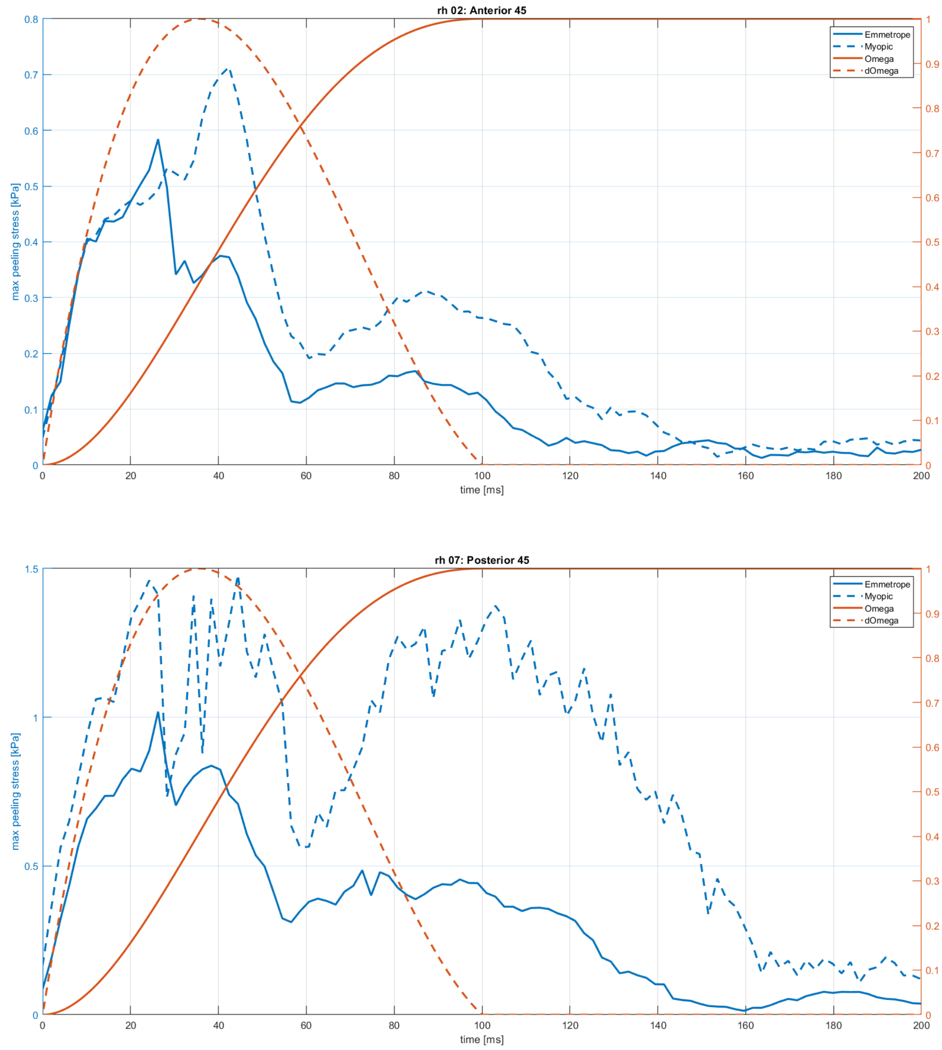

Figure 4.26: Peeling stress acting at the edge of retinal holes in anterior and posterior position for 45°.

Eye type	Position of the hole	σ_{peel} (kPa)	Time of maximum stress (ms)
Emmetrope	Anterior	0.58	26.30
Myopic	Anterior	0.71	42.00
Emmetrope	Posterior	1.01	26.30
Myopic	Posterior	1.48	44.40

Table 4.3: Peeling stress for configurations at 45°.

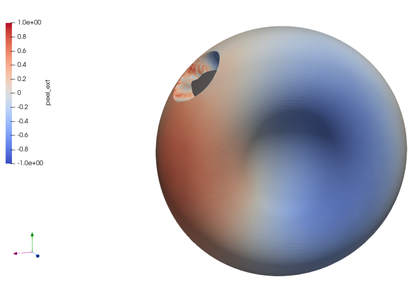

(a) Emmetrope eye with anterior hole

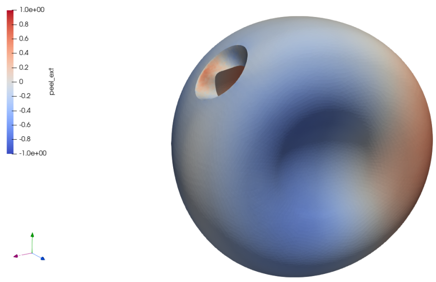

(b) Myopic eye with anterior hole

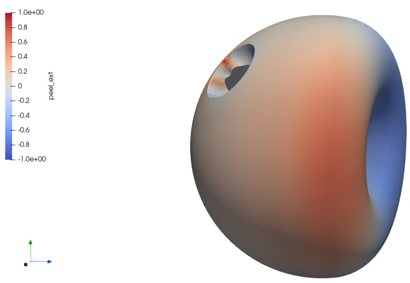

(c) Emmetrope eye with posterior hole

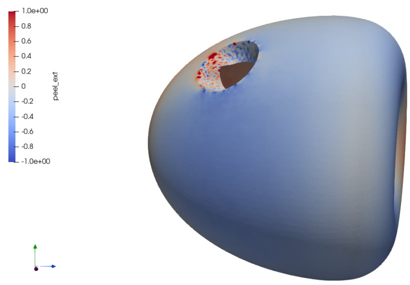

(d) Myopic eye with posterior hole

Figure 4.27: Maximum deformations occurring for eyes with retinal holes at 45°

In Figure 4.28 the maximum peeling stress is graphed for the group with retinal holes at 90°. For this group, the worst case scenario concerns the emmetrope eye with anterior retinal hole, while the emmetrope and the myopic eye with posterior retinal hole undergo comparable, lighter stresses. Results are reported in Table 4.4, while Figure 4.29 shows maximum deformations for the different models.

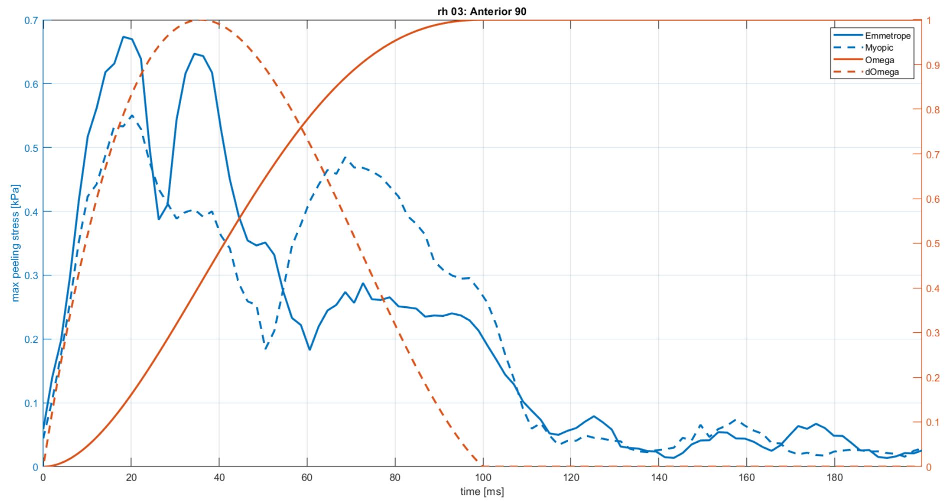

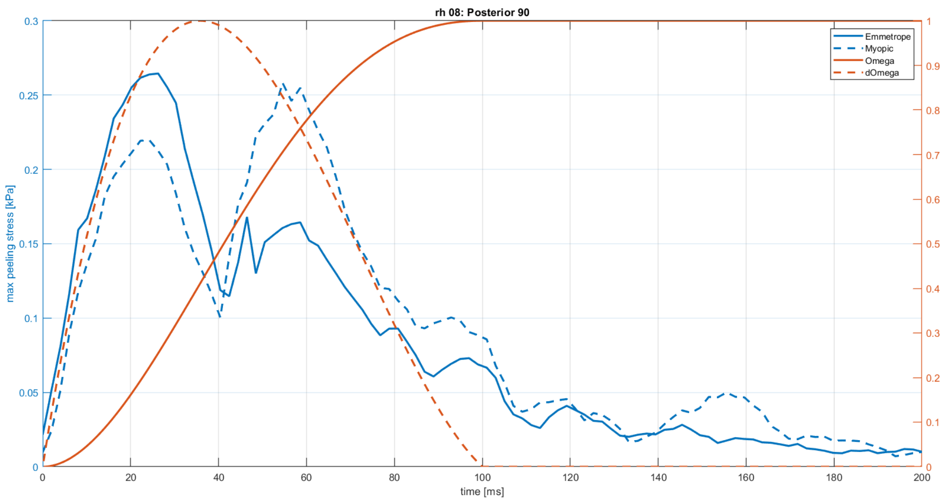

Figure 4.28: Peeling stress acting at the edge of retinal holes in anterior and posterior position for 90°.

Eye type	Position of the hole	σ_{peel} (kPa)	Time of maximum stress (ms)
Emmetrope	Anterior	0.67	18.20
Myopic	Anterior	0.55	20.20
Emmetrope	Posterior	0.26	26.30
Myopic	Posterior	0.26	54.50

Table 4.4: Peeling stress for configurations at 90°.

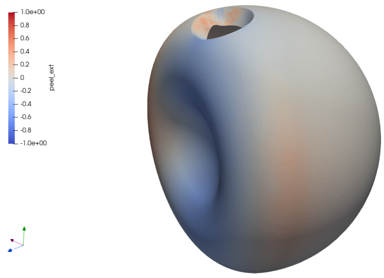

(a) Emmetrope eye with anterior hole

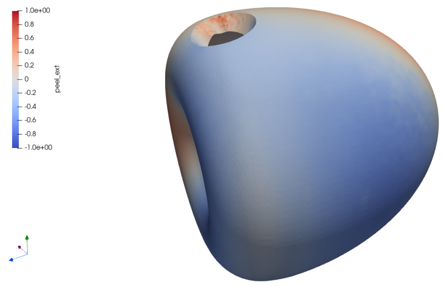

(b) Myopic eye with anterior hole

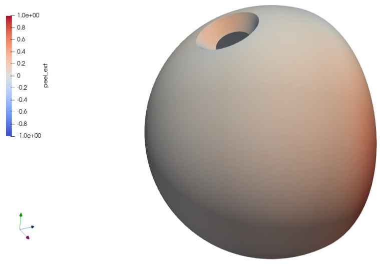

(c) Emmetrope eye with posterior hole

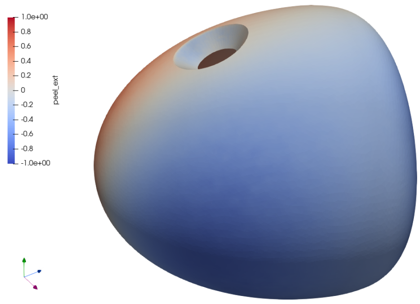

(d) Myopic eye with posterior hole

Figure 4.29: Maximum deformations occurring for eyes with retinal holes at 90°

Regarding the group with retinal holes at 135°, the trend of the maximum peeling stress is represented in Figure 4.30, while their maximum values for each model are listed in Table 4.5. The worst case scenario among these models is that of the myopic eye with posterior retinal hole, while the best configuration is that of the myopic eye with anterior retinal hole. The maximum deformation for each position of the hole is represented in Figure 4.31.

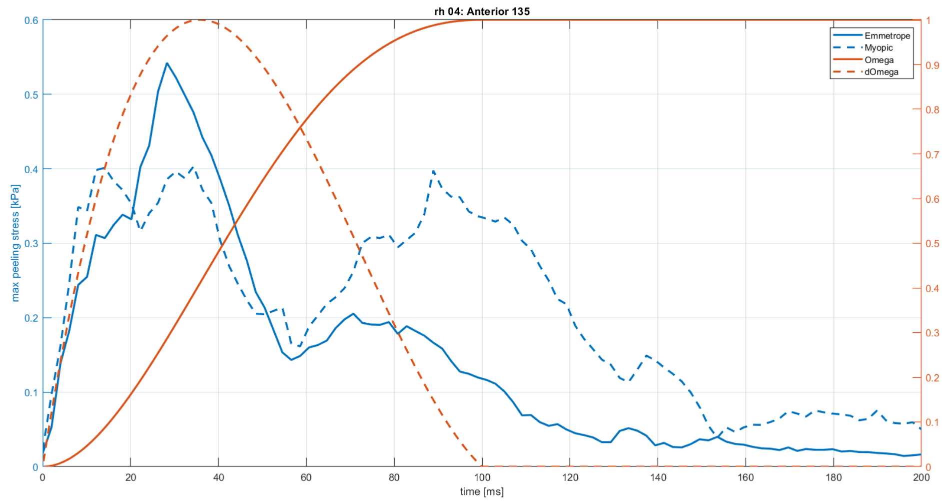

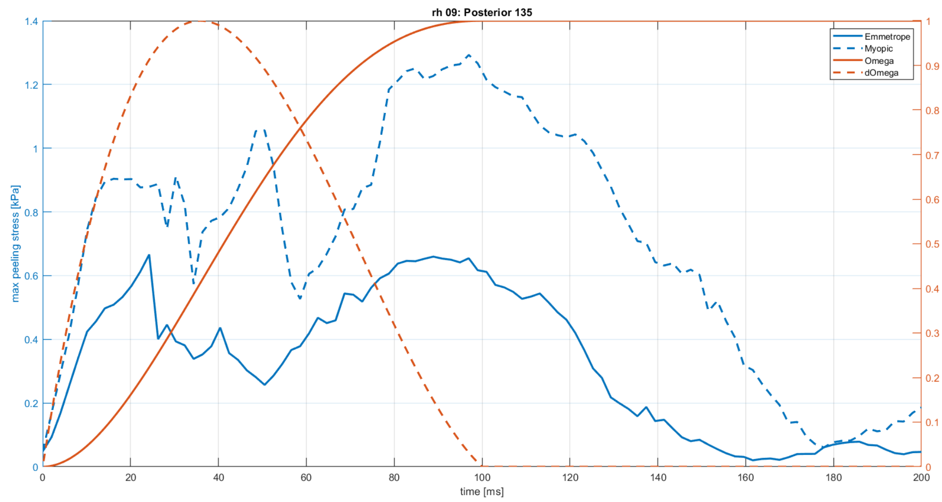

Figure 4.30: Peeling stress acting at the edge of retinal holes in anterior and posterior position for 135°.

Eye type	Position of the hole	σ_{peel} (kPa)	Time of maximum stress (ms)
Emmetrope	Anterior	0.54	28.30
Myopic	Anterior	0.40	34.00
Emmetrope	Posterior	0.67	24.20
Myopic	Posterior	1.29	96.96

Table 4.5: Peeling stress for configurations at 135°.

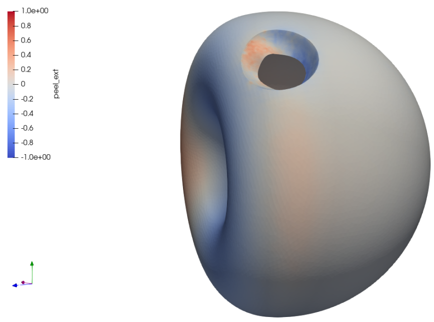

(a) Emmetrope eye with anterior hole

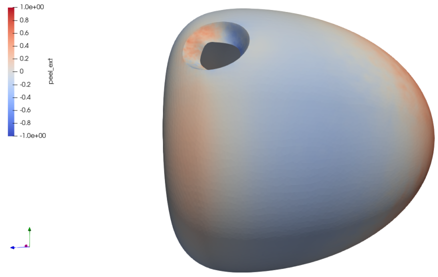

(b) Myopic eye with anterior hole

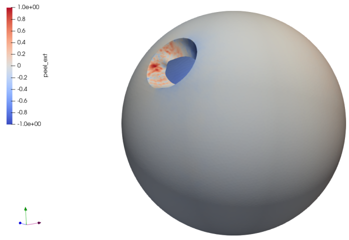

(c) Emmetrope eye with posterior hole

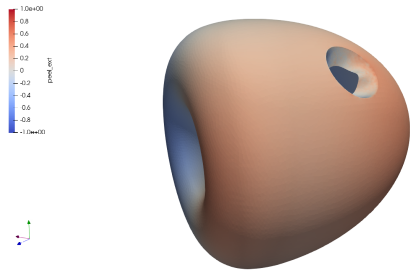

(d) Myopic eye with posterior hole

Figure 4.31: Maximum deformations occurring for eyes with retinal holes at 135°

For the configurations with retinal hole at 180°, the worst case, as for the group with retinal holes at 0°, is the retinal hole in posterior position of a myopic eye, as highlighted in Table 4.6 and in Figure 4.32. In Figure 4.33, maximum deformations for each position of the hole are represented.

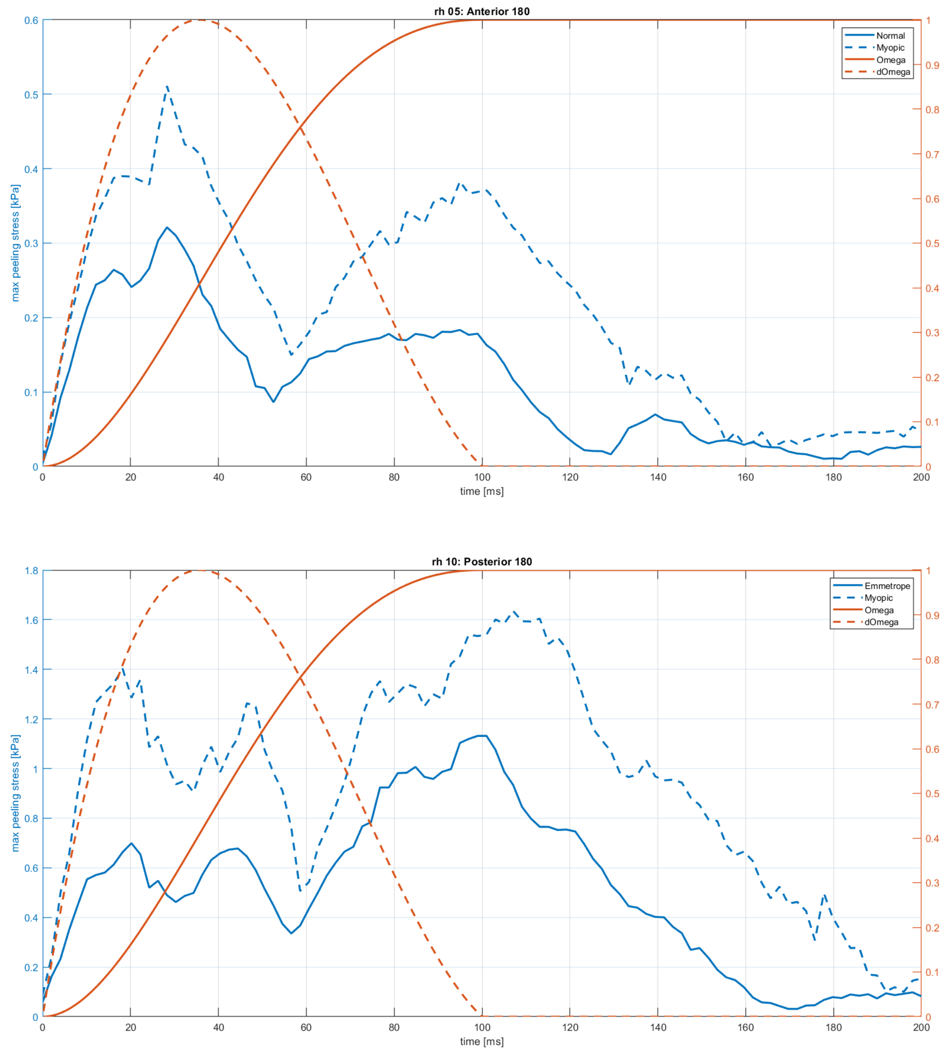

Figure 4.32: Peeling stress acting at the edge of retinal holes in anterior and posterior position for 180°.

Eye type	Position of the hole	σ_{peel} (kPa)	Time of maximum stress (ms)
Emmetrope	Anterior	0.32	28.30
Myopic	Anterior	0.51	28.30
Emmetrope	Posterior	1.13	101.1
Myopic	Posterior	1.63	107.1

Table 4.6: Peeling stress for configurations at 180°.

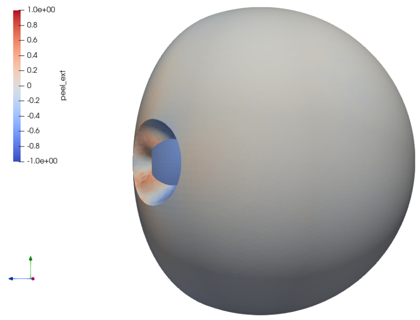

(a) Emmetrope eye with anterior hole

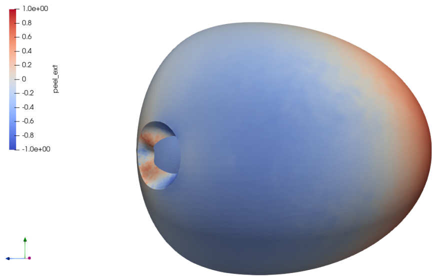

(b) Myopic eye with anterior hole

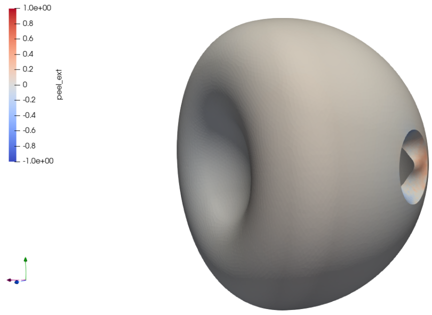

(c) Emmetrope eye with posterior hole

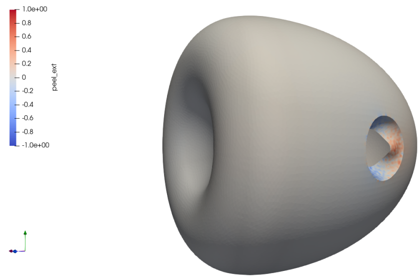

(d) Myopic eye with posterior hole

Figure 4.33: Maximum deformations occurring for eyes with retinal holes at 180°

Finally, Figure 4.34 shows the trend for maximum peeling stress in the case of macular holes, while Table 4.7 reports its maximum value and Figure 4.35 represents the maximum deformations for this position of the retinal hole in an emmetrope and in a myopic eye. As for all of the other groups, except that with retinal holes at 90°, the myopic eye is the one undergoing the highest values of stress.

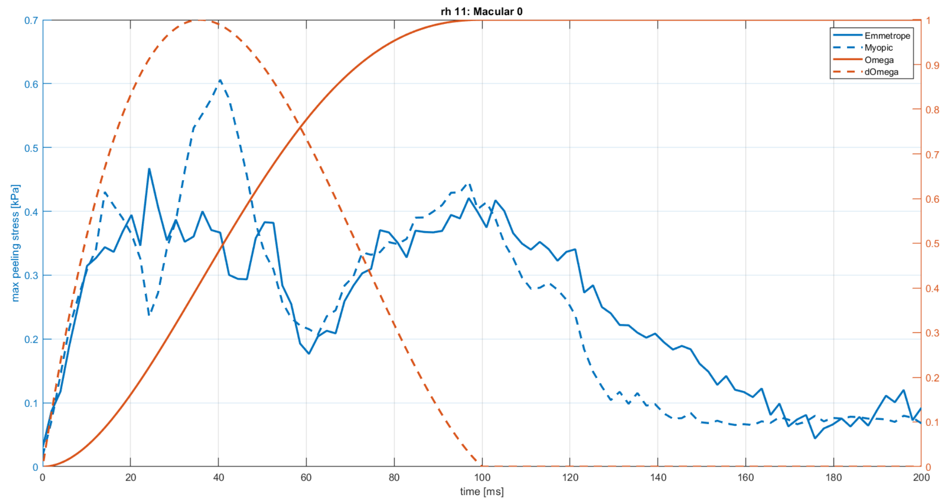

Figure 4.34: Peeling stress acting at the edge of retinal holes in macular position.

Eye type	Position of the hole	σ_{peel} (kPa)	Time of maximum stress (ms)
Emmetrope	Macular	0.47	24.24
Myopic	Macular	0.60	40.40

Table 4.7: Peeling stress for macular configurations.

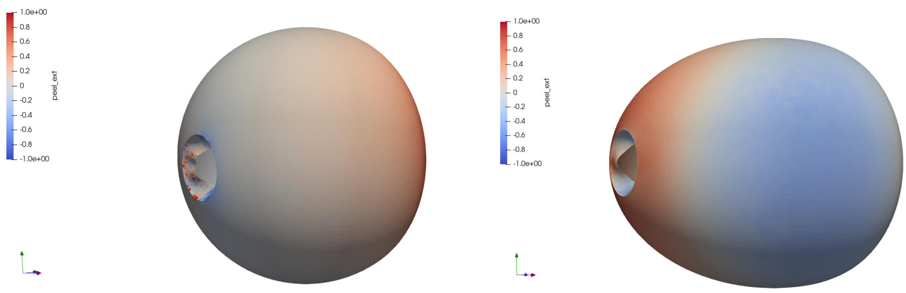

(a) Emmetrope eye with macular hole

(b) Myopic eye with macular hole

Figure 4.35: Maximum deformations occurring for eyes with retinal holes in macular position

In conclusion, Table 4.8 reports the values of the maximum peeling stress for each configuration, in order of decreasing magnitude. The maximum value, obtained for the myopic eye with anterior hole at 0°, is highlighted in red, while the other configurations for which $\sigma_{peel} > \sigma_{max}$ are highlighted in yellow. As a matter of fact, in accordance with the detachment criterion described above, retinal detachment might occur when $\sigma_{peel} > \sigma_{max} = 1$ kPa. For these positions of holes, retinal detachment might occur in absence of external forces, like vitreoretinal traction, and fluid dynamics on its own is sufficient to lead to detachment. It is to notice that the only configurations exceeding the maximum peeling stress are those with posterior retinal holes at 0°, 45°, 135° and 180°, both for the myopic and the emmetrope eye; on the other way round, macular holes don't look very critical and configurations with posterior holes at 90° reach the lowest values of magnitude. This suggests that axial distance from the axis of rotation by itself is not sufficient to induce retinal detachment, but a combination of axial distance and lateral distance is necessary to reach values of σ_{peel} that may induce retinal detachment. Figure 4.36 shows the positions of the retinal holes for the above-mentioned configurations, projected on the xy plane.

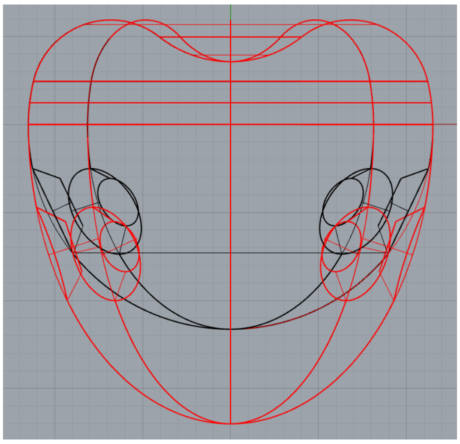

Figure 4.36: Position of retinal holes for the most critical configurations, projected on the xy plane.

Eye type	Position of the hole	Angle (°)	σ_{peel} (kPa)
Myopic	Posterior	0	2.00
Emmetrope	Posterior	0	1.72
Myopic	Posterior	180	1.63
Myopic	Posterior	45	1.48
Myopic	Posterior	135	1.29
Emmetrope	Posterior	180	1.13
Emmetrope	Posterior	45	1.01
Myopic	Anterior	45	0.71
Emmetrope	Posterior	135	0.67
Emmetrope	Anterior	90	0.67
Myopic	Anterior	0	0.64
Myopic	Macular	0	0.60
Emmetrope	Anterior	45	0.58
Myopic	Anterior	90	0.55
Emmetrope	Anterior	135	0.54
Myopic	Anterior	180	0.51
Emmetrope	Macular	0	0.47
Emmetrope	Anterior	0	0.41
Myopic	Anterior	135	0.40
Emmetrope	Anterior	180	0.32
Emmetrope	Posterior	90	0.26
Myopic	Posterior	90	0.26

Table 4.8: Peeling stress among all of the configurations. In red, the most stressed configuration, while in yellow are highlighted all of the other configurations that overcome the value of σ_{max} and might lead to retinal detachment

4.4 Discussion

in generale, le leggenda di colori dei campi (u, p) è difficile leggere perchè il font è piccolo. Figs 4.38, 4.39, …

The above-mentioned results have been evaluated for six different configurations depending on the angle at which the retinal hole is located, as mentioned before. Consequently, the results obtained for all eyes with retinal hole positioned at the same angle will be compared among each other; for example, the emmetrope and the myopic eyes with retinal holes located anteriorly and posteriorly at 0° will be compared with each other. Similarly will be done for eyes with retinal holes at 45°, 90°, 135° and 180° and for those with macular holes. This choice was made since results show a similar behaviour for the eyes within the same group of configurations, whereas it is different among eyes with retinal holes located at different angles. For this reason, it was considered of relevant interest to evaluate the phenomena occurring and the predominant factors for each group of configurations.

4.4.1 Configurations with retinal holes at 0° and at 180°

Eyes with retinal holes at 0° and at 180° are both discussed in here since results obtained from simulations show a similar behaviour between these two different groups of configurations. This is due to the specular position of holes between the two groups which, in spite of the asymmetry of the problem, undergo similar mechanisms of deformation for this reason. As stated above, for these groups of simulations, the most dangerous situation is that involving a myopic eye with retinal hole in posterior position. Table 4.9 reports the magnitude of σ_{peel} in decreasing order for the four different configurations at 0°, while Table 4.10 shows it for the configurations with retinal holes at 180°.

Eye type	Position of the hole	σ_{peel} (kPa)	Time of maximum stress (ms)
Myopic	Posterior	2.00	44.40
Emmetrope	Posterior	1.72	42.40
Myopic	Anterior	0.64	40.00
Emmetrope	Anterior	0.41	30.00

Table 4.9: Peeling stress for configurations at 0° in order of decreasing magnitude.

Eye type	Position of the hole	σ_{peel} (kPa)	Time of maximum stress (ms)
Myopic	Posterior	1.63	107.10
Emmetrope	Posterior	1.13	101.10
Myopic	Anterior	0.51	28.30
Emmetrope	Anterior	0.32	28.30

Table 4.10: Peeling stress for configurations at 180° in order of decreasing magnitude.

As underlined by Table 4.9 and Table 4.10, the value of σ_{peel} decreases when the axial distance between the hole and the axis of rotation is reduced. Moreover, it is to notice that there is not a significant difference in magnitude of the σ_{peel} between the myopic and the emmetrope eyes as long as the retinal hole is in posterior position for both the models or in anterior position for both of them, with both the eyes with posterior retinal hole overcoming the value of σ_{max}. On the other hand, the difference is substantial - a factor two - when a retinal hole in anterior position and one in posterior position are compared. Since configurations with retinal holes at 0° and configurations with retinal holes at 180° have the same trend of results and, due to their specular positions, they have the same phenomena contributing to σ_{peel}, only the group with holes at 0° will be analyzed and discussed in more detail, with results being valid for configurations at 180° as well. For this reason, Figure 4.37 shows the positions of retinal holes in the four configurations considered for this groups; it can be noticed how the difference of axial distance between the anterior (posterior) holes in the emmetrope eye and in the myopic eye is way lower than the difference of distance between holes in anterior position and holes in posterior position, independently from the type of eyes. This fact suggests the huge importance of axial distance as a parameter in the mechanics of retinal detachment. On the other side, the lateral distance between the retinal holes and the axis of rotation is fairly similar across configurations, implying that this parameter is less relevant to compare the results obtained.

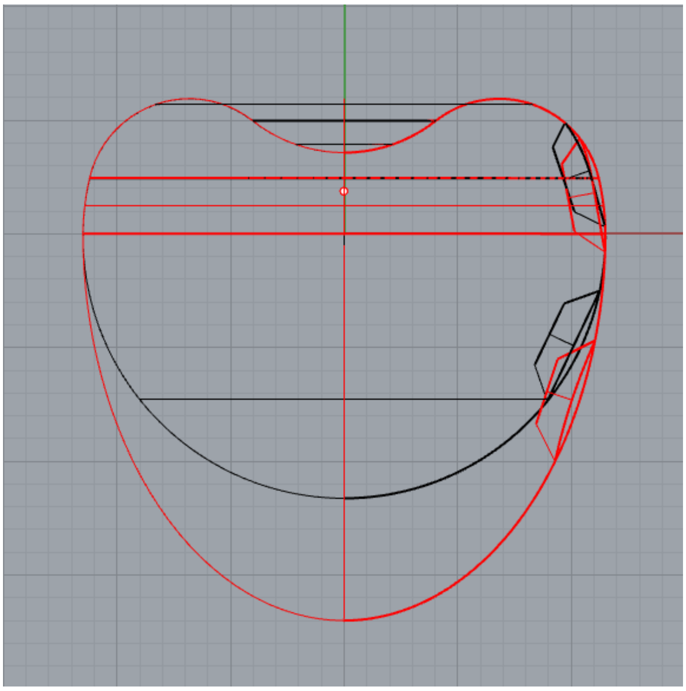

Figure 4.37: Position of retinal holes for configurations at 0°, projected on the xy plane.

In order to better analyze the mechanisms which play the most important roles for the magnitude of σ_{peel}, a comparison of fields of pressure, speed in x direction q_1 and speed in y direction q_2 is made between the four configurations of this group. In order to make the comparison more efficient, values of pressure are dimensionalized with $\rho^* U^{*2}$ and values of speed are dimensionalized with U^*, where ρ^* and U^{*2} are defined in Chapter 3. These fields have been obtained by intersecting the models with a xy plane located at 0°; thanks to the position of retinal holes, this plane intersects the point of maximum deformation during the motion independently from the configuration, since the point of maximum stress lays on the xy plane in the posterior side of the hole. In order to make the comparison more effective, each configuration was evaluated at the time of its maximum peeling stress, which differs from one configuration to another. Figure 4.38, Figure 4.39 and Figure 4.40 represent the field of pressure, speed q_1 and speed q_2, respectively.

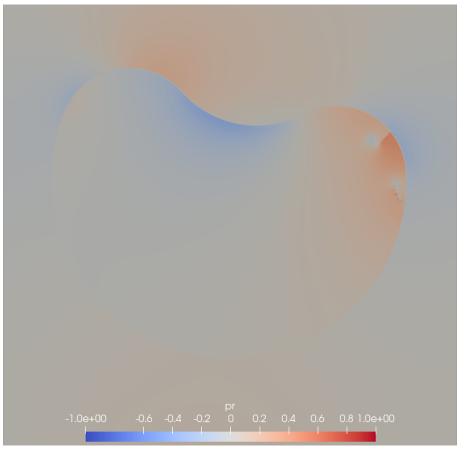

(a) Emmetrope eye with anterior hole

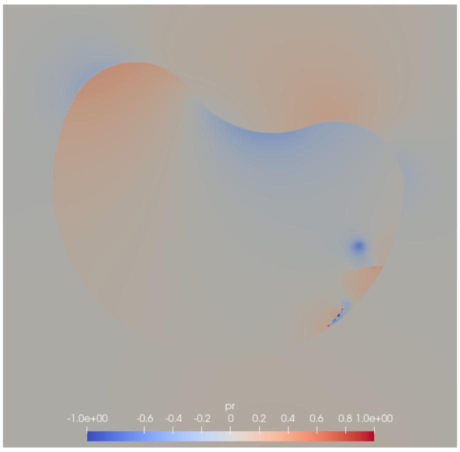

(b) Emmetrope eye with posterior hole

molto difficile
leggere i valori

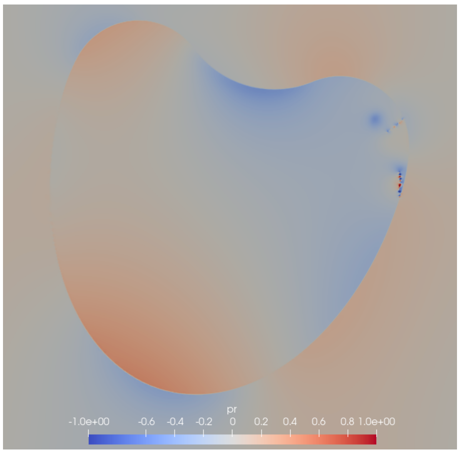

(c) Myopic eye with anterior hole

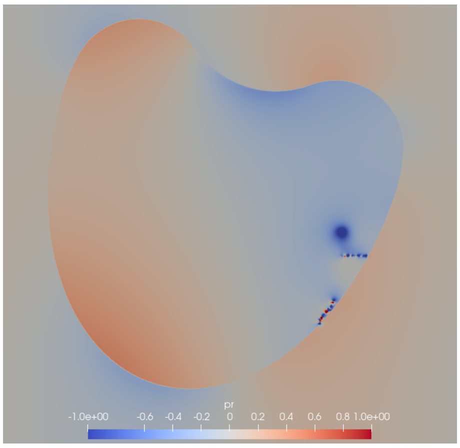

(d) Myopic eye with posterior hole

Figure 4.38: Field of dimensionalized pressure for configurations with retinal holes at 0°

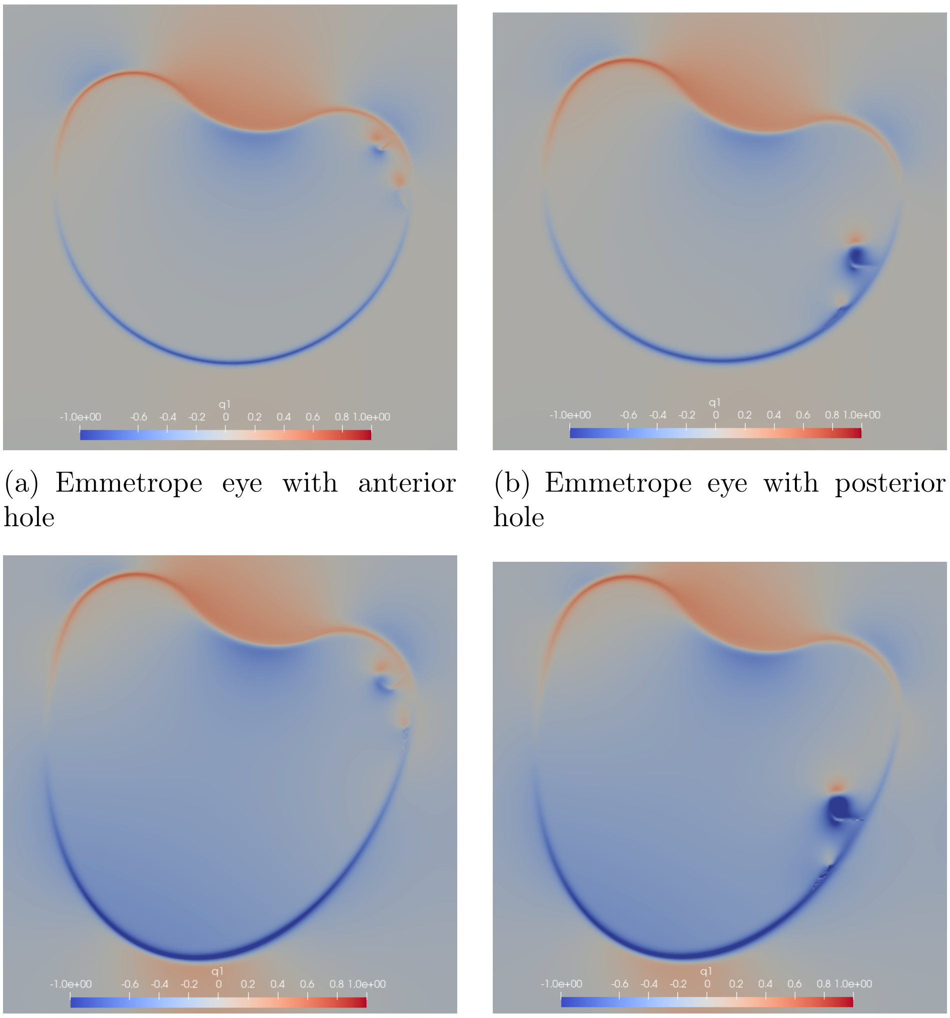

molto difficile leggere i valori

(a) Emmetrope eye with anterior hole

(b) Emmetrope eye with posterior hole

(c) Myopic eye with anterior hole

(d) Myopic eye with posterior hole

Figure 4.39: Field of dimensionalized velocity in x direction q_1 for configurations with retinal holes at 0°.

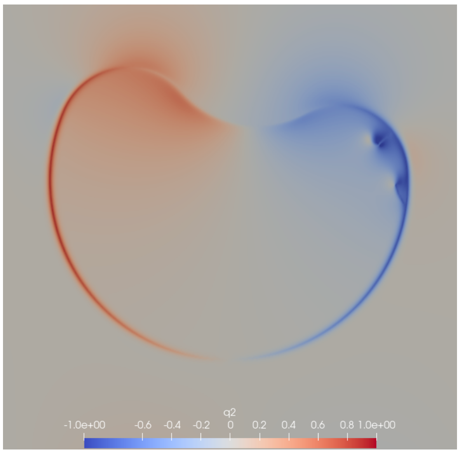

(a) Emmetrope eye with anterior hole

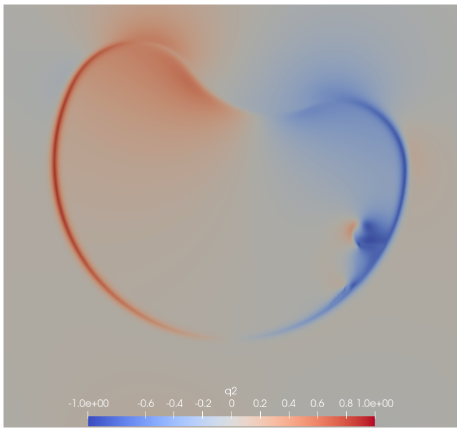

(b) Emmetrope eye with posterior hole

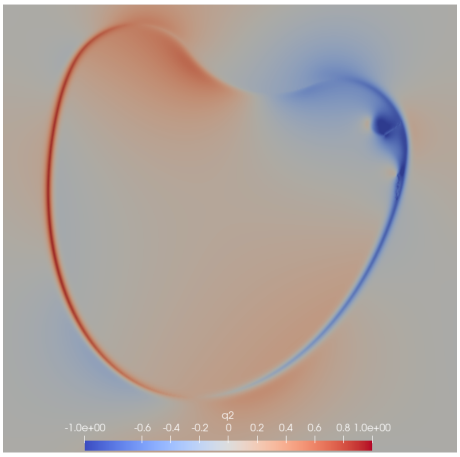

(c) Myopic eye with anterior hole

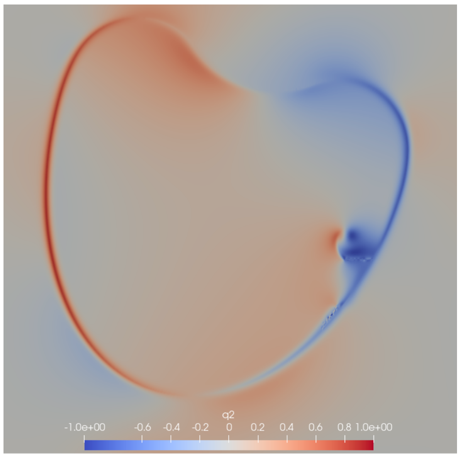

(d) Myopic eye with posterior hole

Figure 4.40: Field of dimensionalized velocity in y direction q_2 for configurations with retinal holes at 0°.

From Figure 4.38, it is possible to see how the difference between the upper and the lower pressure acting on the raised surface of the retina - $(p_f^+ - p_f^-)$ - increases for cases in which a higher σ_{peel} values was recorded.
Regarding the contribute given by shear stress, Figure 4.39 highlights, for the speed component in x direction q_1, the same trend of pressure, with increasing difference between above and below the surface for the configuration corresponding to higher σ_{peel} values, while Figure 4.40 shows a different trend, with major difference of q_2 (component of speed in y direction) for eyes with anterior retinal hole. Both these results are in accordance with the distance in x and y direction between the centre of the retinal hole and the axis of rotation, for which values of speed increase with the distance from the axis. The results obtained for σ_{peel} suggest that components of $\nabla\mathbf{u}$ involving the x component of speed are more relevant than those involving the y direction to obtain greater values of difference between upper and lower shear stress $(\boldsymbol{\tau}_f^+ - \boldsymbol{\tau}_f^-)$. Since, as stated in Chapter 3, $\mathbf{F}_f^{ext} = [-(p_f^+ - p_f^-)\mathbf{n}_f^+ + (\boldsymbol{\tau}_f^+ - \boldsymbol{\tau}_f^-) \cdot \boldsymbol{n}_f^+]A_f$,

due to the considerations above, it is possible to conclude that the combination of pressure gradient and shear stress due to axial distance from the axis of rotation is crucial to obtain high values of σ_{peel} and for the consequent retinal detachment for configurations where retinal holes are located at 0°, thus suggesting that axial distance plays a relevant role in this type of situation. It is also to mention that lateral distance does not play a fundamental role in the choice of the most critical configuration within this group with retinal holes at 0°, but it for sure counts when different groups are compared; as a matter of fact, macular retinal holes, especially on myopic eyes, have the highest value of axial distance and an approximately null value of lateral distance, but values of σ_{peel} are much lower than those recorded for retinal holes at 0° in posterior position for both myopic and emmetrope eyes. It is probably due to the fact that the difference of pressure and shear stress are more relevant for holes with a greater later distance, making them more penalized from a stress point of view in comparisons with retinal holes located on the yz plane (like macular and 90° configurations). Consequently, as stated above, shear stress induced by q_1 on its own is not sufficient to induce retinal detachment, but the combination of shear stress and gradient of pressure might be detrimental. As stated above, the same considerations are applicabe to group with retinal holes at 180°.

4.4.2 Configurations with retinal holes at 90°

This group of configurations is very interesting, due to the fact that the myopic and emmetrope eyes with posterior retinal hole record the lowest values of σ_{peel}, with the emmetrope eye with anterior retinal hole being the most critical case, in contrast to all other groups of simulations, as Table 4.11 shows.

Eye type	Position of the hole	σ_{peel} (kPa)	Time of maximum stress (ms)
Emmetrope	Anterior	0.67	18.20
Myopic	Anterior	0.55	20.20
Emmetrope	Posterior	0.26	26.30
Myopic	Posterior	0.26	54.50

Table 4.11: Peeling stress for configurations at 90° in order of decreasing magnitude.

As previously, the fields of pressure, speed q_1 and speed q_2 are evaluated on the yz field. They are represented in Figure 4.41, Figure 4.42 and Figure 4.43, respectively, for each configuration at the time of its maximum deformation. By the way, it is important to underline that, in this case, the plane does not intersect the point of maximum deformation; moreover, the intersection changes during the motion due to rotation of the eye; as a matter of fact, the plane doesn't intersect the hole in the myopic eye with posterior retinal hole. Due to all of these considerations, this analysis is less accurate than the one above, but it still suggests interesting reflections regarding fluid dynamic phenomena that occur.

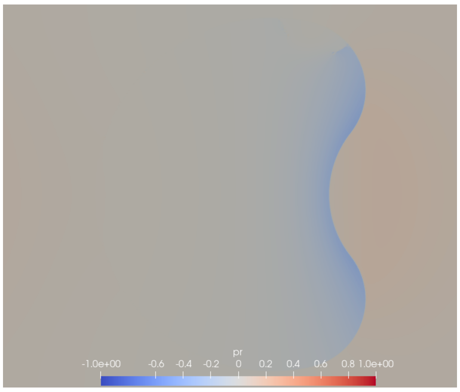

(a) Emmetrope eye with anterior hole

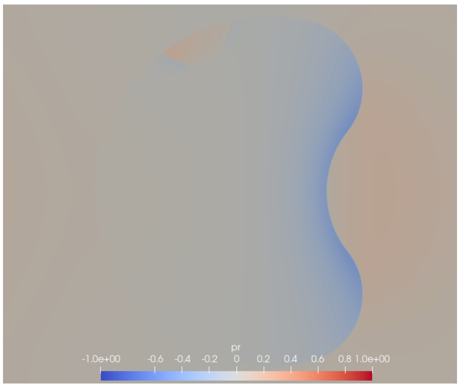

(b) Emmetrope eye with posterior hole

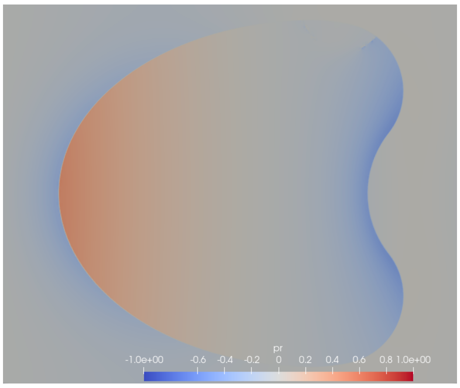

(c) Myopic eye with anterior hole

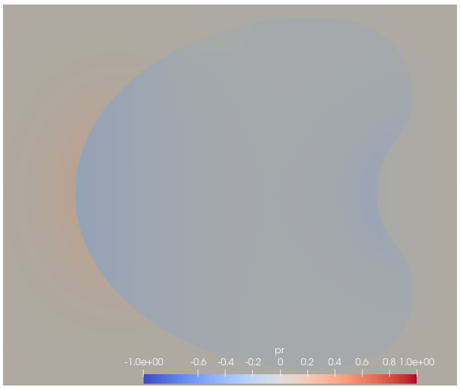

(d) Myopic eye with posterior hole

Figure 4.41: Field of dimensionalized pressure for configurations with retinal holes at 90°

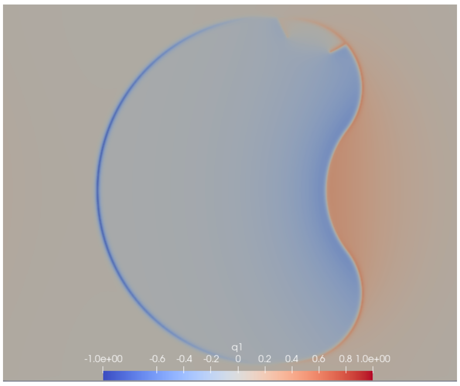

(a) Emmetrope eye with anterior hole

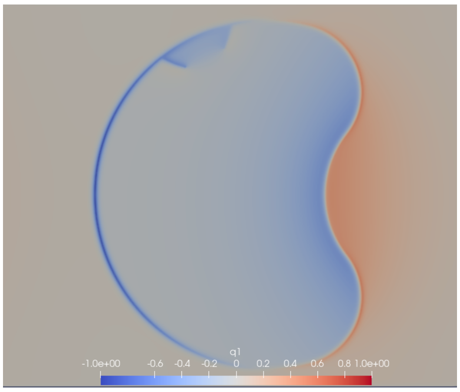

(b) Emmetrope eye with posterior hole

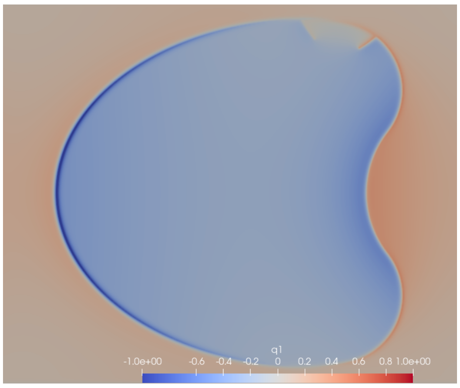

(c) Myopic eye with anterior hole

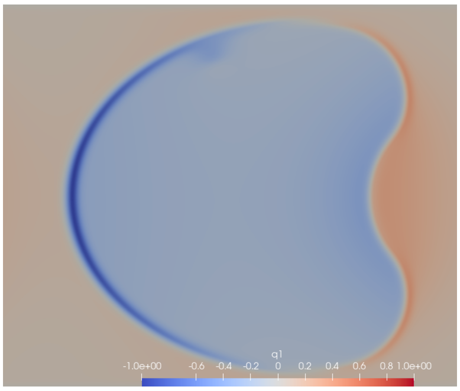

(d) Myopic eye with posterior hole

Figure 4.42: Field of dimensionalized velocity in x direction q_1 for configurations with retinal holes at 90°.

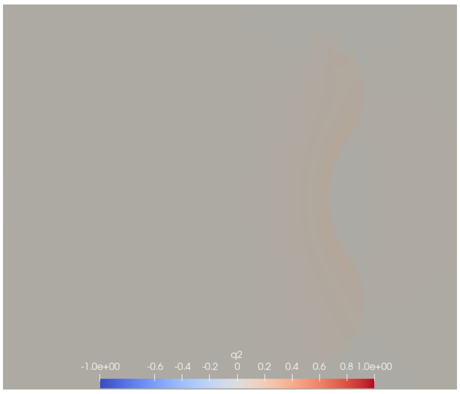

(a) Emmetrope eye with anterior hole

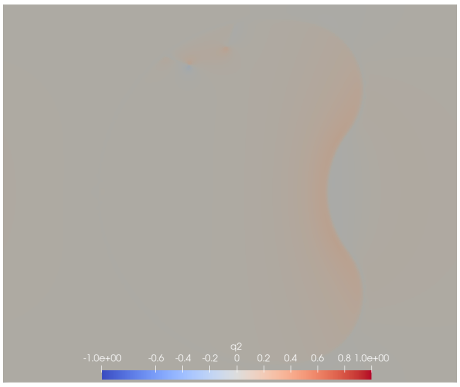

(b) Emmetrope eye with posterior hole

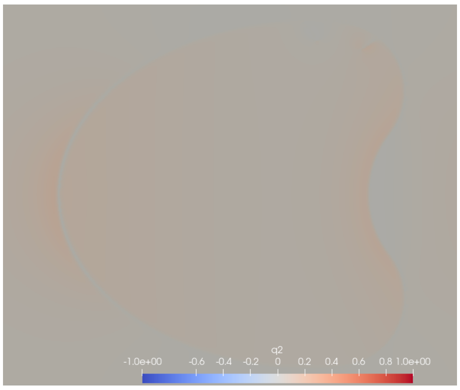

(c) Myopic eye with anterior hole

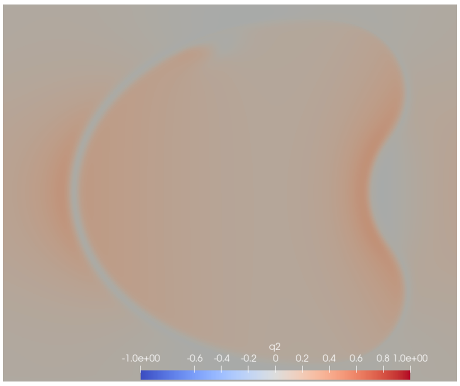

(d) Myopic eye with posterior hole

Figure 4.43: Field of dimensionalized velocity in y direction q_2 for configurations with retinal holes at 90°.

For this group of configurations, speed in y direction q_2 is not relevant, since retinal holes are all located at the same lateral distance; for this reason, pressure and speed in x direction are the only relevant parameters. Regarding the contribution of q_1, which induces shear stress, it depends on axial distance; Figure 4.44 shows the different position of retinal holes for this group of simulations, while the point indicates the axis of rotation.

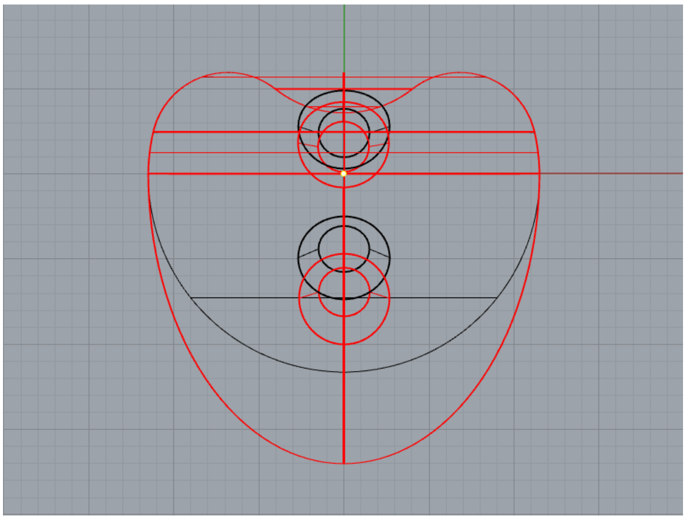

Figure 4.44: Position of retinal holes for configurations at 90°, projected on the xy plane.

It is possible to notice a difference between this group and the group with retinal holes at 0°, since in this case holes in anterior position are ahead of the axis even at the time of maximum stress, while for the other group all of the configurations where above the axis at the time of maximum peeling stress. For this reason, as far as the anterior position is evaluated and the contribution of shear stress due to axial distance is concerned, the hole on the emmetrope eye is further from the axis of rotation than the hole on the myopic eye and this fact explains why the emmetrope eye with anterior retinal hole is more solicited than the myopic one. On the other side, this consideration is not sufficient on its own to explain why eyes with holes in anterior position are largely more stressed than eyes with holes in posterior position. As a matter of fact, referring to Figure 4.44, according to the previous consideration, the myopic eye with posterior retinal hole should be the most stressed one, since its axial distance from the axis of rotation is the greatest and the shear stresses acting on the raised surface should be the highest. In fact, shear stress contribution is not the only one to take into account. Figure 4.45, which shows the field of pressure for all of the four configurations, helps to better understand the role of pressure gradients for this group of eyes, since the scale is more refined.

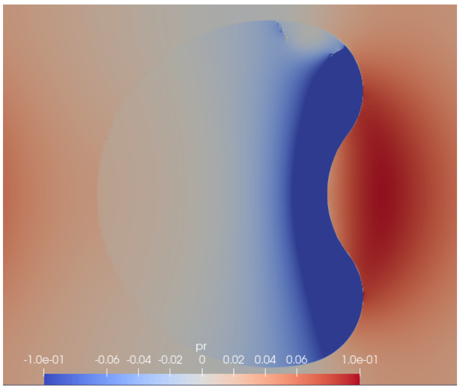

(a) Emmetrope eye with anterior hole

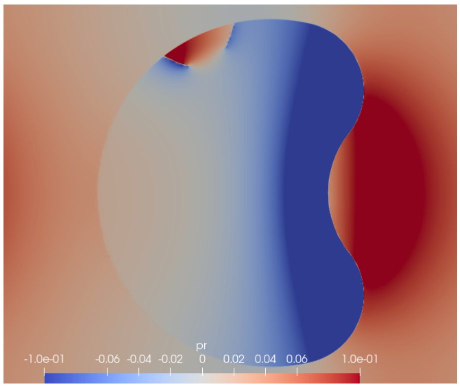

(b) Emmetrope eye with posterior hole

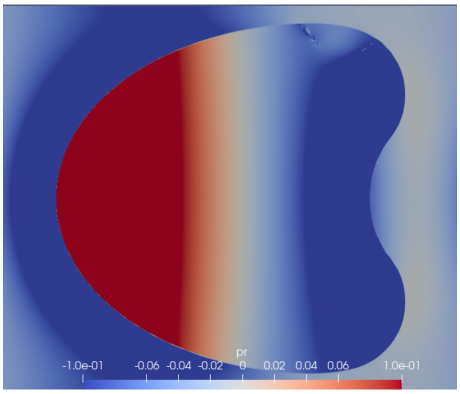

(c) Myopic eye with anterior hole

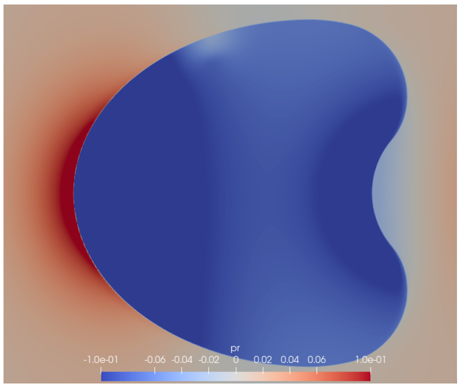

(d) Myopic eye with posterior hole

Figure 4.45: Field of dimensionalized pressure for configurations with retinal holes at 90°, with a lower scale to have a more visible comparison.

As the figure shows, retinal holes in anterior position are invested by a strong gradient of pressure, which is due to their position; as a matter of fact, both on the emmetrope and on the myopic eye, anterior retinal holes are located in closed proximity to the axis of rotation, around which the pressure gradient is very relevant; since this difference of pressure happens within the diameter of the holes, in these cases their dimensions are not negligible with respect to the dimensions of the problem. The presence of this pressure gradients, for anterior retinal holes only, explains why retinal holes in anterior positions are more stressed than those in posterior position, where the gradient is not relevant, in spite of a greater axial distance from the axis of rotation. This distance becomes decisive between the emmetrope and the myopic eye with anterior hole, both invested by the pressure gradient, but it is not relevant when anterior and posterior positions are compared, since the pressure gradient gives a definitely more relevant contribution. These considerations explain why the emmetrope eye with anterior retinal hole results in more stress than the other configurations, thanks to the strong pressure gradients along its diameter and to its axial distance from the axis of rotation. It is important to underline that this group of configurations is the only one presenting this characteristics due to the proximity of anterior retinal holes to the axis of rotation. Finally, it is to mention that, overall, greater values of stress among this group are lower when compared to those obtained for other groups, since lateral distance of retinal holes from the axis of rotation is very small, making the contribution of q_2 to shear stress almost null.

4.4.3 Configurations with retinal holes at 45° and 135°

As for configurations with retinal holes at 0° and at 180°, also those with holes at 45° and 135° show results with trends similar between each other, so they will be discussed together. These two groups of configurations have values of stress comparable to those obtained for groups with holes at 0° and 180°, with the exception of anterior retinal holes at 135°, where the emmetrope eye is more solicited than the myopic one. Anyway, this consists in an isolated case with no explicable reason, which might be caused by a numerical error in simulations. Table 4.12 and Table 4.13 report resulting values of σ_{peel} for groups with holes at 45° and at 135°, respectively.

Eye type	Position of the hole	σ_{peel} (kPa)	Time of maximum stress (ms)
Myopic	Posterior	1.48	44.40
Emmetrope	Posterior	1.01	26.30
Myopic	Anterior	0.71	42.00
Emmetrope	Anterior	0.58	26.30

Table 4.12: Peeling stress for configurations at 45° in order of decreasing magnitude.

Eye type	Position of the hole	σ_{peel} (kPa)	Time of maximum stress (ms)
Myopic	Posterior	1.29	96.96
Emmetrope	Posterior	0.67	24.20
Emmetrope	Anterior	0.54	28.30
Myopic	Anterior	0.40	34.00

Table 4.13: Peeling stress for configurations at 135° in order of decreasing magnitude.

Unluckily, for these two groups of configuration it is difficult to define a cartesian plane which intersects retinal holes during the motion, due to their positions. Anyway, from the obtained results and from considerations about position of holes for these configurations compared to those of the previously-analyzed groups, it is possible to deduce that the same phenomena playing relevant roles in groups with holes at 0° and 180° are decisive for these two groups too. For this reason, it is to believe that the combination of axial and lateral distance from the axis of rotation and pressure is fundamental for retinal detachment.

4.4.4 Configurations with macular retinal holes

The group of configurations with macular holes shows the same trend of results as configurations with holes at 0°, 45°, 135° and 180°, with myopic eye more stressed than emmetrope eye. Anyway, it is to notice that, when macular holes are concerned, neither the myopic nor the emmetrope eye reach values of peeling stress capable to induce a retinal detachment, which is of particular interests since macular holes have the highest axial distance from the axis of rotation. Table 4.14 reports values of σ_{peel} for myopic and emmetrope eyes with macular hole.

Eye type	Position of the hole	σ_{peel} (kPa)	Time of maximum stress (ms)
Myopic	Macular	0.60	40.40
Emmetrope	Macular	0.47	24.24

Table 4.14: Peeling stress for configurations with macular holes in order of decreasing magnitude.

As previously, also for this group of configurations it is possible to evaluate the field of pressure and of speed on a xy plane intersecting the retinal holes in their points of maximum peeling stress. Figure 4.46, Figure 4.47 and Figure 4.48 show the field of pressure, speed q_1 and speed q_2, respectively.

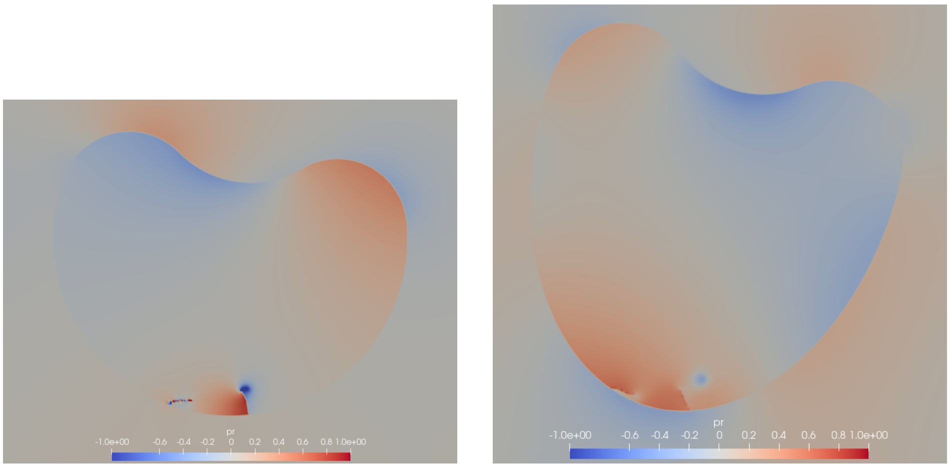

(a) Emmetrope eye with macular hole

(b) Myopic eye with macular hole

Figure 4.46: Field of dimensionalized pressure for configurations with macular retinal holes.

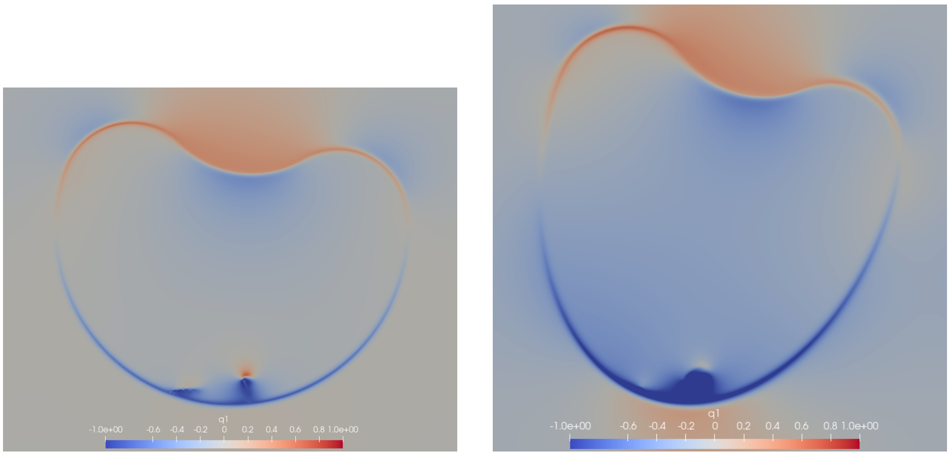

(a) Emmetrope eye with macular hole

(b) Myopic eye with macular hole

Figure 4.47: Field of dimensionalized velocity in x direction q_1 for configurations with macular retinal holes.

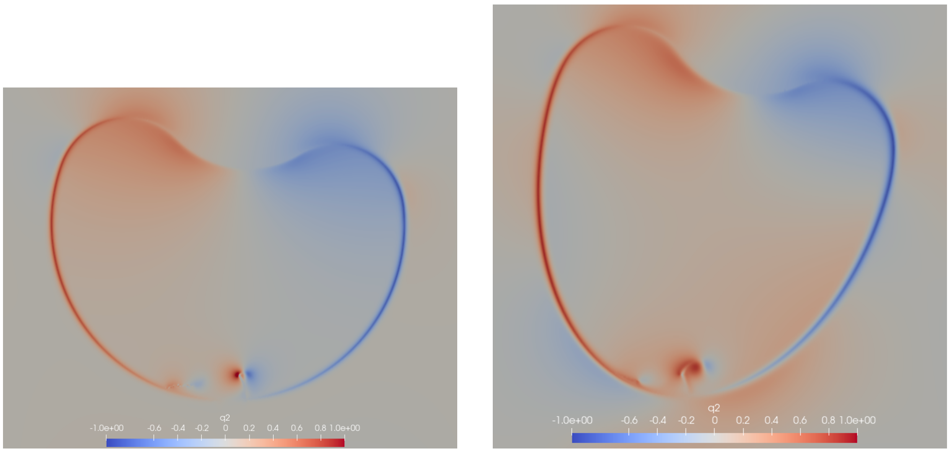

(a) Emmetrope eye with macular hole

(b) Myopic eye with posterior hole

Figure 4.48: Field of dimensionalized velocity in y direction q_2 for configurations with macular retinal holes.

From Figure 4.46, it is possible to see that the difference $(p_f^+ - p_f^-)$ of pressure acting on the surface of the risen retina is greater for the myopic eye. Moreover, axial distance from the axis of rotation plays an important role, since it increases the value of velocity gradients, especially concerning q_1, and consequently the value of shear stress, which is thought to be the preponderant contribution for this group of retinal holes. As a matter of fact, Figure 4.47 shows a great difference in velocity field for q_1 between the emmetrope and the myopic eye and also the way surfaces deform suggests a prevalent contribution of shear stress with respect to pressure.

4.5 Conclusions

Simulations run on several different configurations of retinal holes have given very interesting preliminary results. In particular, for configurations with retinal holes at 0°, 45°, 135°, 180° and in macular position, axial distance from the axis of rotation is relevant within each group to increase the value of peeling stress, suggesting determinant role of shear stress due to q_1. On the other side, when different groups are compared, it was seen that axial distance alone is not sufficient to induce great values of σ_{peel}, suggesting that a combination of pressure and shear stress due to both q_1 and q_2 is necessary to reach values of peeling stress sufficient to induce retinal detachment, with the greatest values recorded for a great value of both the axial and the lateral distance from the axis of rotation. Macular holes recorded lower values of σ_{peel} than configurations with retinal holes at 0°, in spite of a greater axial distance; the reason is to account to the greater lateral distance in configurations at 0°, compared to the almost null lateral distance in macular configurations.
A further consideration should be made regarding macular holes. Several studies indicate a prevalence of retinal detachment from macular holes in myopic eyes compared to emmetrope eyes; results obtained in this work indicate values of σ_{peel} which are insufficient to induce retinal detachment in both the emmetrope and the myopic eye, thus suggesting that retinal detachment in myopic eyes with macular retinal hole is not induced by fluid dynamics only. The axial elongation of myopic eyes might involve a stretching and a thinning of the retina in the posterior section of the eye; this morphological change in myopic eyes, combined with the greater values of hydrodynamic loads do to axial elongation, might result in an increased risk of retinal detachment with respect to emmetrope eyes.
As far as fluid dynamics only is regarded, posterior retinal holes at 0° in myopic eyes are the most dangerous. The fact that, for some configurations, also emmetrope eyes with posterior retinal holes might reach retinal detachment suggests that, when hydrodynamic loads induced by a combination of shear stress and pressure, due to axial and lateral distance from the axis, reaches eligible values, retinal thinning due to axial elongation in myopic eye is not a relevant factor anymore.
In conclusion, the results given by this work are a first useful approach to a very complex tridimensional problem, but it still is a preliminary approach that should be improved in order to reduce the number of assumptions for the problem set-up, such as more realistic dimensions of retinal holes, a partially liquefied vitreous and a reduced thickness of posterior section of the retina on myopic eyes.

Chapter 5

Horseshoe Retinal Tears

Horseshoe retinal tears are the most common type of retinal breaks and their development and lifting are strictly related to posterior vitreous detachment and vitreoretinal traction. Because of this strong connection with PVD and vitreoretinal traction, the problem involving the evolution of retinal tears should be treated accounting for the biphasic (liquid and gel) nature of the vitreous humor. In the following, some preliminary results in the case of vitreous humor modelled as a Newtonian fluid are reported.

5.1 Problem set-up

As stated above, differently from retinal holes, problems involving retinal tears are more complex, due to the presence of a portion of vitreous gel attached to the risen portion of retina. This portion of gel induces vitreoretinal tension that contributes to keep the retinal tear lifted. For an accurate evaluation of the problem, it is not possible to neglect this contribution. Anyway, taking into account vitreoretinal tension would imply the need to represent a biphasic fluid, which moves and creates a variable tension during the motion. This kind of work requires a lot of effort and time and, for this reason, as far as this qualitative analysis is concerned, vitreoretinal traction is neglected and the strong assumption of considering the vitreous fully liquefied is made. Moreover, gravital force is not considered in this work, hence the position of the retinal tear along a circumference of the eye is irrelevant from this point of view, while it still remains important as far as fluid dynamic loads are concerned.
Retinal tears can develop in a wide variety of positions, orientations and dimensions. The surgical treatment for retinal tears is scleral buckling, as explained in Chapter 1. For this reason, two different type of problems are evaluated in this work. Both the problems concern an emmetrope eye, since axial length is not relevant for this type of breaks. The first problem concerns a sick eye with three different orientations of retinal tears, located at the same positions and oriented in y-direction, z-direction and in-between these two (approximately diagonal with respect to those

two directions). This study is useful to understand which orientation is visibly the most critical and which one is not a matter of concern for an evolution of retinal detachment. The second problem concerns the application of a scleral buckle and consists of a comparison of the same retinal tear, oriented in y-direction, before and after the indentation of the retina caused by a radial scleral buckle. All of the configurations are made with the retinal tear intersecting the xy plane which passes through the origin of the eye, as for the configurations at 0° in Chapter 4. Figure 5.1 shows the three different configurations of retinal tears considered in the first problem. For this problem, retinal tears are positioned at the section of maximum diameter of the eye and dimensions of retinal tears are bigger than those in nature; in fact, retinal tears are usually 1.5 mm large and 2 mm long, while those considered for this problem are about 2.5 mm large and 3.5 mm long.

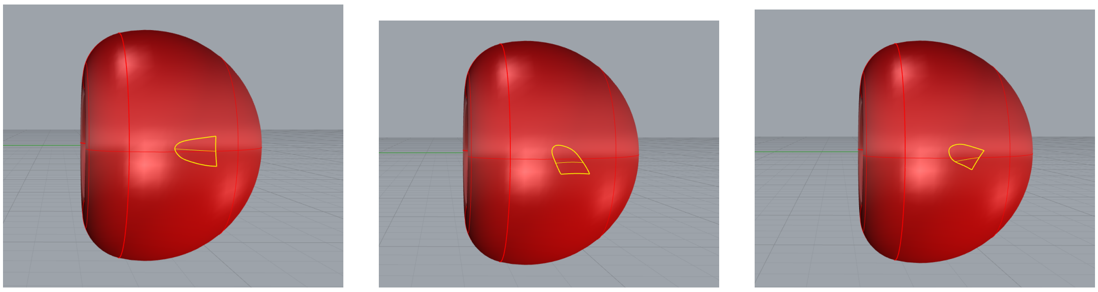

(a) Retinal tear in y-direction

(b) Retinal tear in z-direction

(c) Retinal tear with 45° angle between the y and z directions

Figure 5.1: Different orientations of retinal tears considered for the first problem.

As far as the problem involving the comparison with and without scleral buckle is concerned, for this case the retinal tear has more relistic dimensions, being 1.5 mm large and 2.4 mm long. Moreover, it is positioned 4.5 mm prior to the equator, since, according to ophthalmologists, this is the position where retinal tears are more likely to occur. On the other side, the radial scleral buckle taken into account for this problem has an elliptic section of dimensions 3 mm x 5 mm and it is 4.5 mm long. The scleral buckle creates an 1.5 mm indentation in the eye and it is positioned in order to have the retinal tear at its center. Figure 5.2 represents both the retinal tear used for this second problem and the eye indented by the scleral buckle. For this second case, the position of the retinal tear is translated along the x-direction to represent what happens when a scleral buckle is inserted in the eye with a surgical procedure, as explained in Chapter 1.

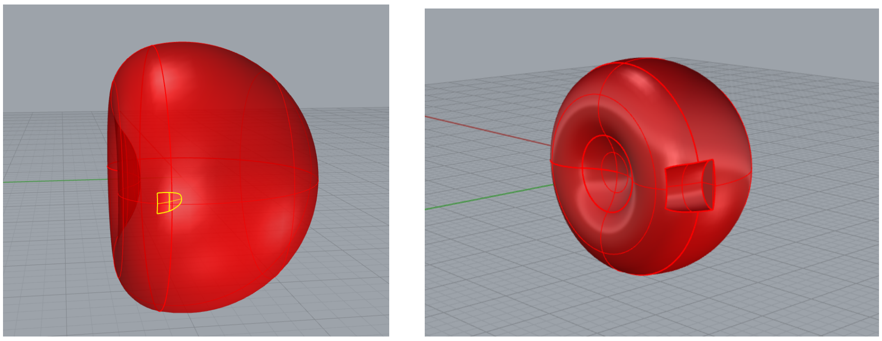

(a) Eye with retinal tear before surgery

(b) Eye with retinal tear after surgery

Figure 5.2: Models of eye with retinal tear and eye with radial scleral buckle for the second type of problem.

The qualitative analysis consists of a visual evaluation of deformation for each of the cases of study, in order to understand which configuration leads to a wider opening of the retinal tear.
As in Chapter 4, the retina is reduced to a thin layer of thickness $t = 0.22$ mm and Young's Modulus $E = 1$ kPa, in accordance to literature. For simulations, a whole (or indented) retina rotates during a saccadic movement thanks to the imposed kinematic law expressed in Chapter 2 and used in Chapter 4; a retinal tear is thought as an elongated surface with a clamping angle of 50° with the shorter edge attached to the whole retina. In order to reproduce the clamping constraint, the same kinematic law as that of the whole retina is imposed to the first two lines of nodes on the retinal tear. In this way, the retinal tear is free to deform but it maintains its clamping angle still and follows the whole retina during the motion. Regarding the features of the whole retina, the model is the same used in Chapter 4, representing an emmetrope eye of axial length of 23.5 mm.

5.2 Building of the models

As stated above, two different kind of problems involving horseshoe retinal tears are treated in this chapter. For the first problem, concerning three different orientations of retinal tears, it is necessary to create a CAD model for the retinal tear and a CAD model for the whole retina on software Rhinoceros. For the second type of problem, regarding the retinal tear and the indented eye with scleral buckle, it is necessary to have a model of the retinal tear and a model of the retina, as before, but also a model for the indented retina.

5.2.1 Whole retina

As shown in Figure 5.3, the healthy retina surface is created starting from a draft, which represent half a section of the eye. In order to create the surface of revolution, the draft is rotated around the y-axis through the command “Revolve”.

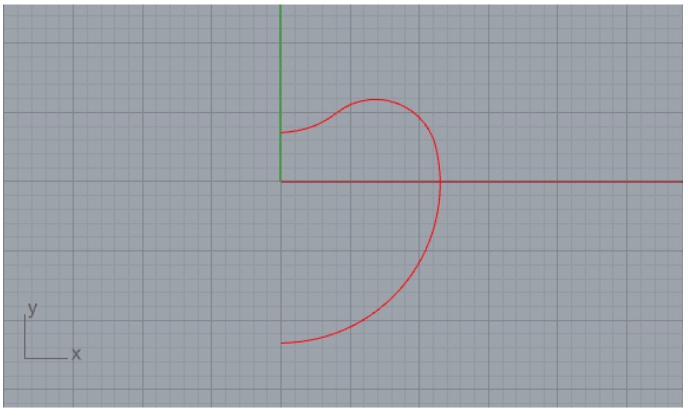

Figure 5.3: Sketch of half section of the retina.

From this step, three different surfaces are made, so, in order to have one surface only, the command “Join” is applied. Figure 5.4 represents the 3D geometry of the whole retina.

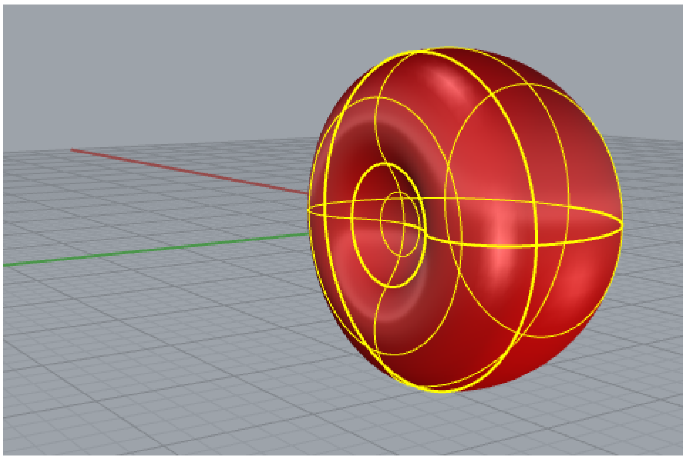

Figure 5.4: 3D geometry of the whole retina.

To create a quadrangular mesh on the surface, the command “Mesh from surface/polysurface” is used; later, the surface underneath is removed. Then, the quadrangular mesh is turned into a triangular one, with the command “Triangulate mesh”. To improve the quality of the mesh, it is uploaded in .stl format on MeshLab, where the filter “Remeshing: isotropic explicit remeshing” is applied, with a target length depending on the type of problem of interest. As a matter of fact, for the first problem a loose mesh is sufficient, due to the dimensions of retinal tears, while for the second problem a more refined mesh is necessary, since dimensions of the retinal tear are smaller. Figure 5.5 shows the refined mesh for the first problem, while Figure 5.6 shows the refined mesh for the second one. The difference in the number of nodes and faces between the two models is quite relevant.

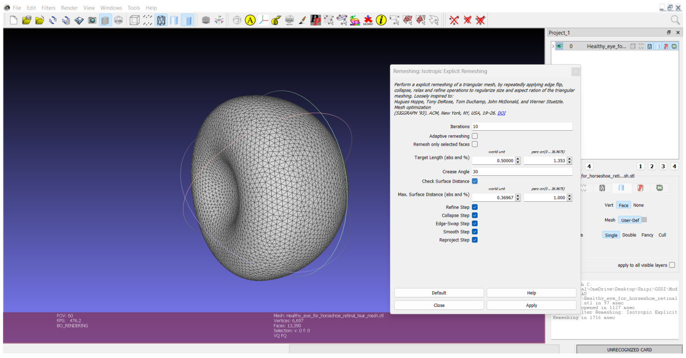

Figure 5.5: Mesh improvement on MeshLab for the first type of problem.

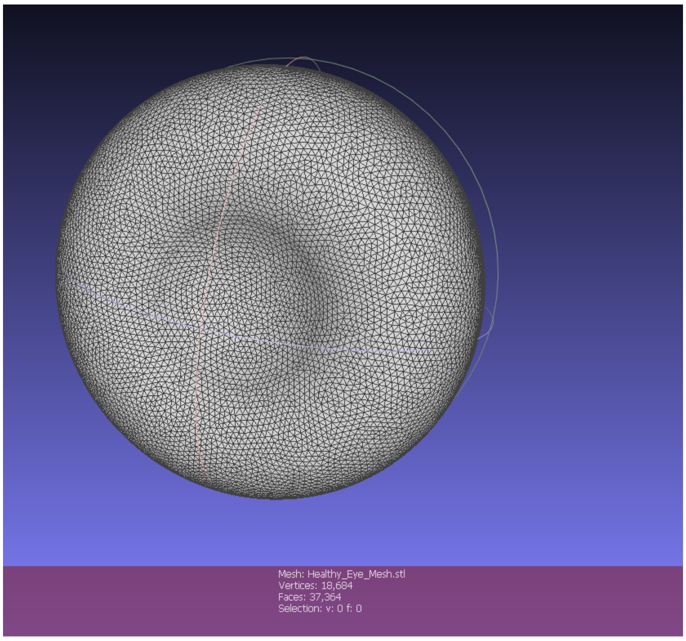

Figure 5.6: Mesh improvement on MeshLab for the second type of problem.

5.2.2 Horseshoe retinal tear

The procedure for the model for horseshoe retinal tear is the same for each dimension and orientation; for this reason, in this section, it will be treated in a general way, but the procedure is exstensible to every other configuration. The substantial difference among models consists of a different level of mesh refinement.
Since models for retinal tears must be compatible with the model for the whole retina, the latter is used as a reference for the making of the retinal tear, which is literally drawn on its surface. For this reason, starting from the surface of the whole retina, whose creation was explained above, it is necessary to use the command "Interpolate curve on surface" to draw a closed curve representing the retinal tear, as represented in Figure 5.7.

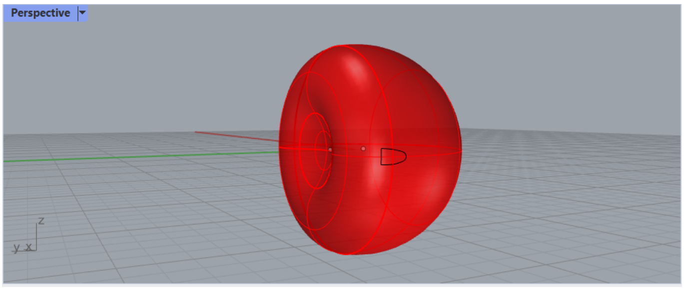

Figure 5.7: Sketch of horseshoe retinal tear interpolated on the surface of the whole retina.

In order to make a different surface for the retinal tear, the command "Split surface from isocurve", using the curve created previously as a contour. Figure 5.8 shows the so-made surface, whose border is in yellow.

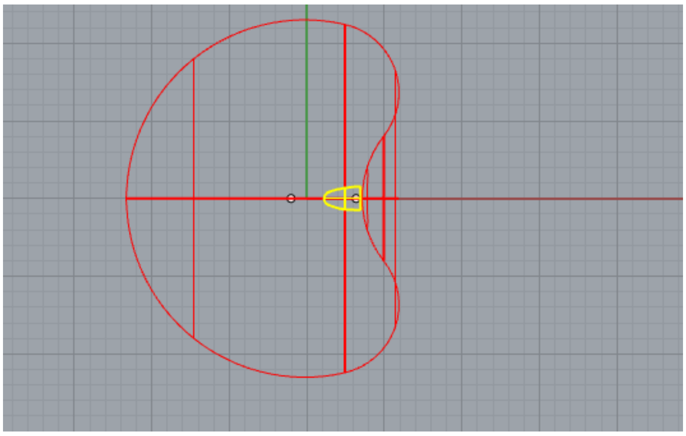

Figure 5.8: Surface of horseshoe retinal tear on the surface of the whole retina.

The next step consists of a rotation of the surface around its shorter edge, in order to create the clamping angle, through the command "Rotate 3-D", with a starting angle of 50°. In Figure 5.9 the retinal tear rotated of 50° is shown.

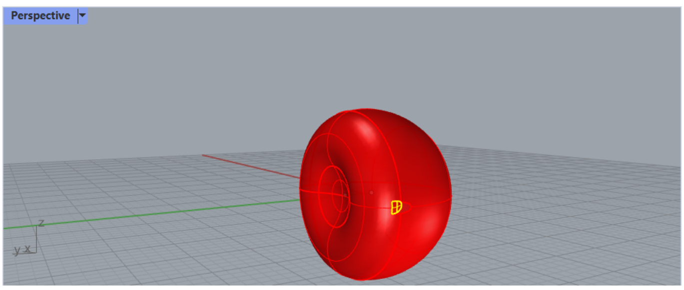

Figure 5.9: Surface of horseshoe retinal tear rotated of 50° around its shorter edge.

Finally, the surface of the whole retina is removed and a quadrangular mesh is applied on that of the horseshoe retinal tear by using the command "Mesh from surface/polysurface". The surface underneath is removed and the resulting mesh is reported in Figure 5.10.

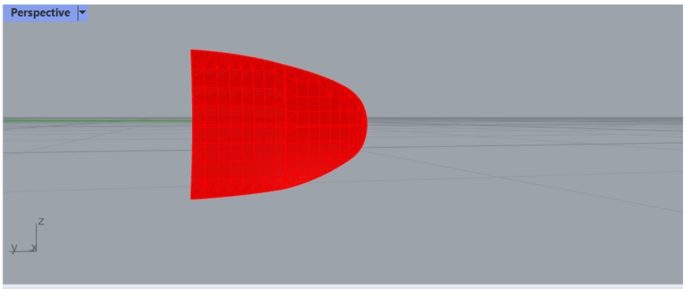

Figure 5.10: Qadrangular mesh on the horseshoe retinal tear.

The quadrangular mesh is then turned into a triangular mesh through the command "Triangulate mesh". The resulting triangular mesh is shown in Figure 5.11

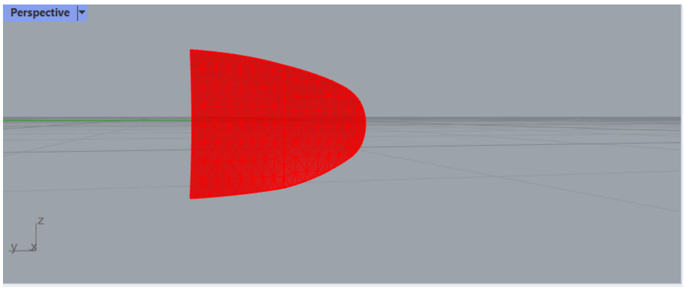

Figure 5.11: Triangular mesh on horseshoe retinal tear.

To conclude, the triangular mesh is refined in MeshLab using the filter "Remeshing: isotropic explicit remeshing"; as for the whole retina, the degree of refinement depends on the model of interest. Figure 5.12 compares a retinal tear used for the first problem of interest and a retinal tear used for the second one; it is to notice that their numbers of faces and nodes are comparable, differently from the case of the whole retina.

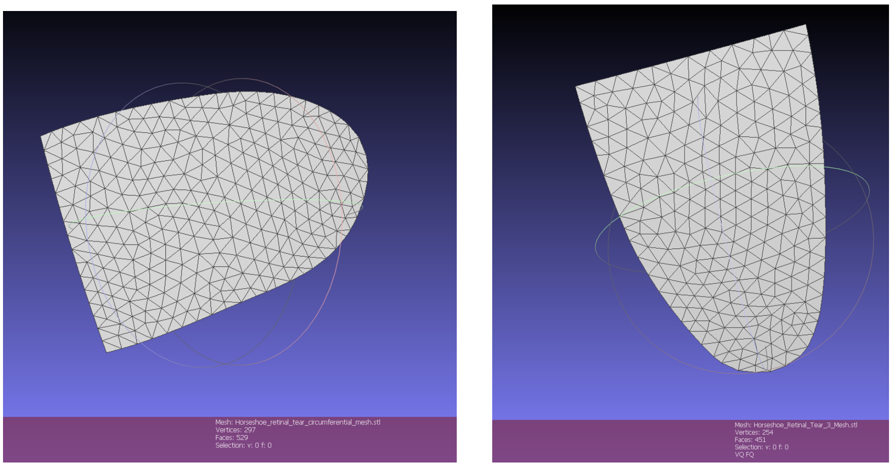

(a) Retinal tear for the first problem (b) Retinal tear for the second problem

Figure 5.12: Comparison between a retinal tear from the first problem and a retinal tear from the second problem, both remeshed on MeshLab.

5.2.3 Indented retina from scleral buckle

The creation of the indented retina, resulting from surgery, starts with the making of a model for the selected scleral buckle. This model is later going to intersect that of the whole retina to create the indentation. As a matter of fact, for the study of fluid dynamics within the eye, it is not necessary to have the surface of scleral buckle, it is only necessary to represent the effect of its presence on the retina. The first step consists in the draft of an ellipse of desired dimensions (3 mm x 5 mm); this ellipse must be positioned in order to create a maximum indentation of around 1.5 mm. During the construction of the configuration with scleral buckle it is convenient to use the model of the retinal tear as a reference. Figure 5.13 shows the ellipse drawn on the whole retina.

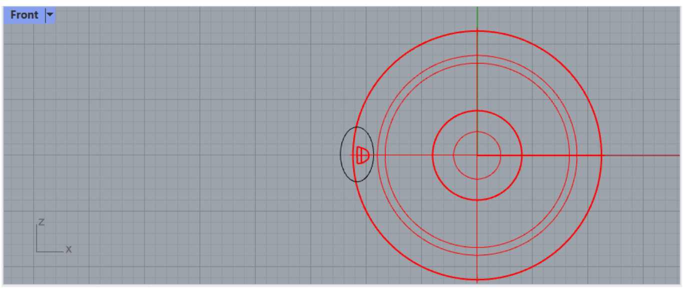

Figure 5.13: Sketch of the elliptical section of the scleral buckle.

To create the surface of the scleral buckle, since its profile should be curved to follow the profile of the retina, it is necessary to apply the command "Rail revolve", by drawing an arc of circumference as a railway from the origin. Surfaces at the extremities of the model are filled by using the command "Surface from planar curve". The result is shown in Figure 5.13

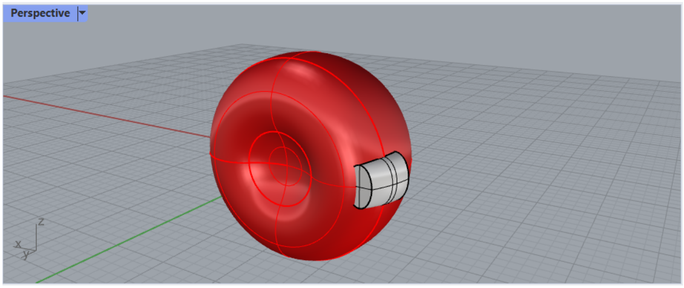

Figure 5.14: Surface of scleral buckle on the whole retina.

In order to make the indentation, the command "Boolean split" is used and the external surface of the scleral buckle is removed, so that only the indentation created by the scleral buckle remains, as highlighted from Figure 5.15

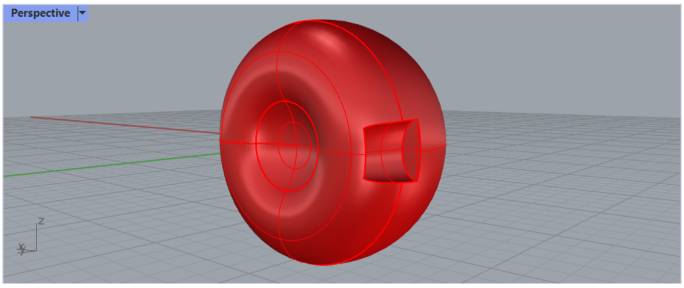

Figure 5.15: Surface of the whole retina indented by scleral buckle.

Later, a quadrangular mesh is applied on the surface through the command "Mesh from surface/polysurface" (Figure 5.16) and it is turned into a triangular mesh by using the command "Triangulate mesh".

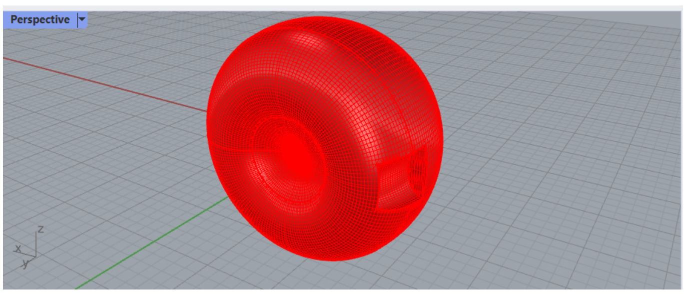

Figure 5.16: Quadrangular mesh on the indented retina.

In order to improve the quality of the mesh, the model is imported on MeshLab, where the filter "Remeshing: isotropic explicit remeshing" is applied with a target length of 0.3 and 10 iterations. Finally, in order to smoothen the borders of indentation, the filter "Laplacian Smooth" is used with 3 smoothing steps. Figure 5.17

and Figure 5.18 represent the mesh on the indented retina after the refinement and after the smoothing, respectively.

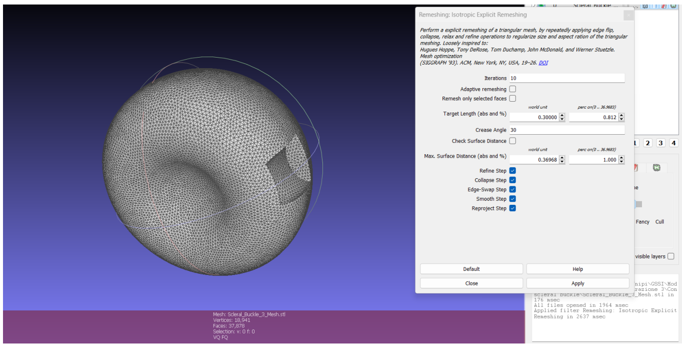

Figure 5.17: Refined triangular mesh on the indented retina.

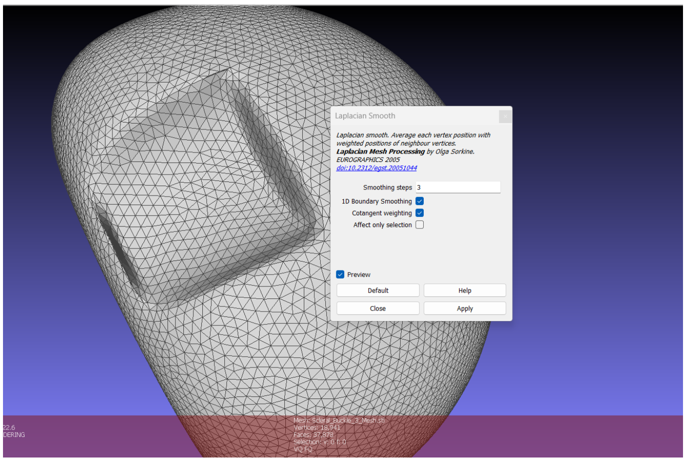

Figure 5.18: Triangular mesh on the indented retina after the application of the "Laplacian smoothing" filter.

To conclude, the model of the retinal tear must be adapted to the model of the indented eye; in order to do it, it is necessary to translate the model of the retinal tear along the x-axis until the limit of intersection between the two surfaces. It is to specify that for the retina the model in Figure 5.18 is used, while for the retinal tear the surface is imported, without mesh. Since it is necessary to have the edge of the retinal tear adjacent to the surface of the retina, the command "Split mesh" is applied on the tear using the whole retina as a cutting tool. This creates a retinal tear with a corner laying on the retina and, moreover, it also creates a triangular mesh on the retinal tear. This triangular mesh must be imported on MeshLab to improve the quality of mesh through, as always, the filter “Remeshing: isotropic explicit remeshing”. The result is shown in Figure 5.19.

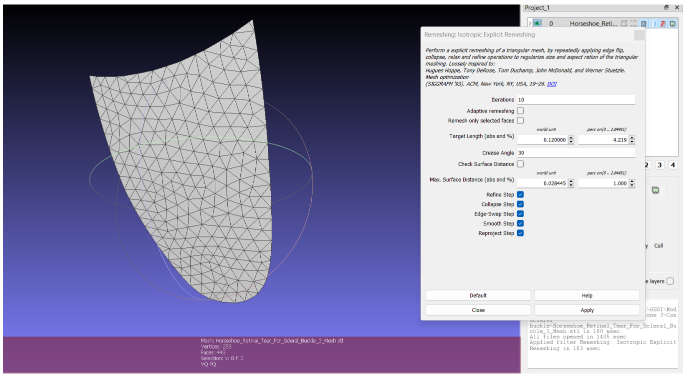

Figure 5.19: Meshed retinal tear compatible with the indented retina.

It is to underline that the difference between the model of horseshoe retinal tear used for the whole retina and the one used for the indented retina is not substantial and it is supposed not to change the results of simulations. Figure 5.24 shows the difference between these two models.

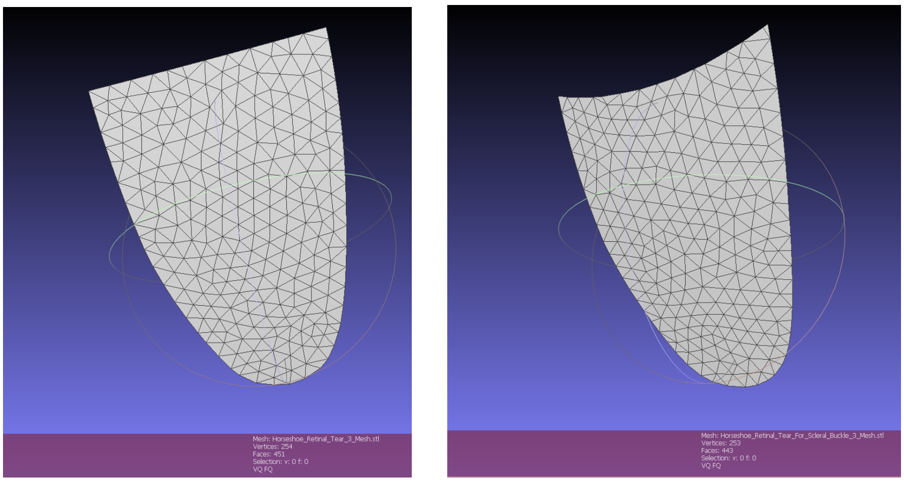

(a) Retinal tear for the whole retina model

(b) Retinal tear for the indented model

Figure 5.20: Comparison between the retinal tear for the whole retina model and the retinal tear for the indented retina model, both remeshed on MeshLab

5.3 Results and discussion

In this section, a visual comparison of results obtained from simulations is made among the three different orientations studied in the first problem and between the pre-surgery and the post-surgery configuration in the second problem.

5.3.1 Horseshoe retinal tears with different orientations

Figure 5.21, Figure 5.22 and Figure 5.23 compare the maximum deformation of retinal tears with their position at the beginning of the saccadic movement, for the retinal tear orientated in z-direction, in y-direction and in-between the other two, respectively.

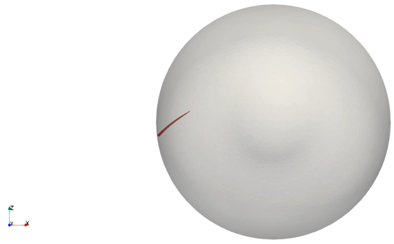

(a) Retinal tear at the beginning of motion

(b) Retinal tear at its maximum deformation

Figure 5.21: Comparison between the retinal tear in z-direction at the beginning of the saccade and at its maximum deformation.

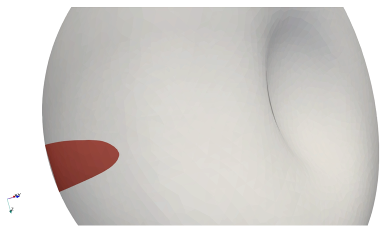

(a) Retinal tear at the beginning of motion

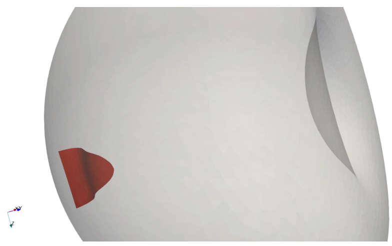

(b) Retinal tear at its maximum deformation

Figure 5.22: Comparison between the retinal tear in y-direction at the beginning of the saccade and at its maximum deformation.

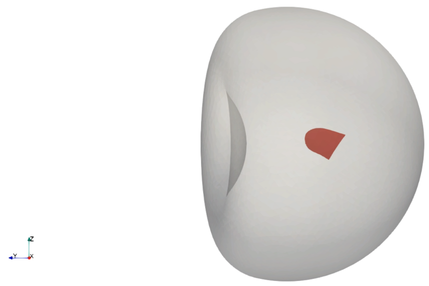

(a) Retinal tear at the beginning of motion

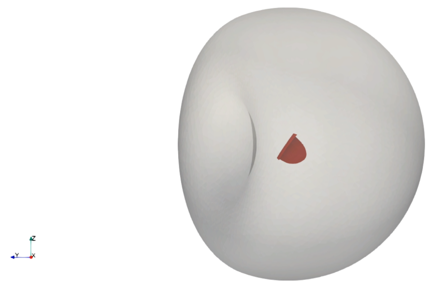

(b) Retinal tear at its maximum deformation

Figure 5.23: Comparison between the retinal tear in intermediate direction between the y-axis and the z-axis at the beginning of the saccade and at its maximum deformation.

Figure 5.21, Figure 5.22and Figure 5.23 reveal that the orientation in z-direction induces deformations definitely smaller than those induced in the two other configurations, while deformations for retinal tears orientated in y-direction and for retinal tears orientated in an intermediate direction are of comparable entity.
Most probably, this phenomenon is related to the hydrodynamic loads induced by the rotation around the z-axis. As a matter of fact, when the retinal tear is orientated in z-direction, the biggest contribution to hydrodynamic forces is made by viscous stress and the contribution of pressure is probably way inferior; this deduction is in accordance with both the way this surface deforms and the way the fluid invests the surface. On the other way round, when the retinal tear is oriented in y-direction, pressure acting on the surface gives a huge contribution for the "opening" of the break, much more than shear stress. Finally, regarding the retinal tear in intermediate position, it is likely that both the pressure and the shear stress have a great impact on the deformation, which explains why this retinal break is the one which bends the most.

5.3.2 Comparison of horseshoe retinal tears with and without radial scleral buckle

Figure 5.24 shows results obtained for deformations of retinal tear when the retina is not indented (before surgery) and when it is indented by the presence of a radial scleral buckle inserted surgically.

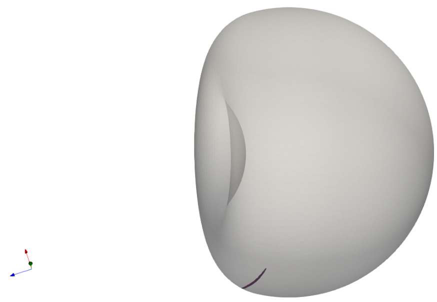

(a) Maximum deformation of retinal tear without scleral buckle

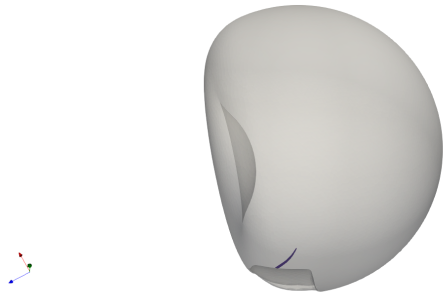

(b) Maximum deformation of retinal tear with scleral buckle

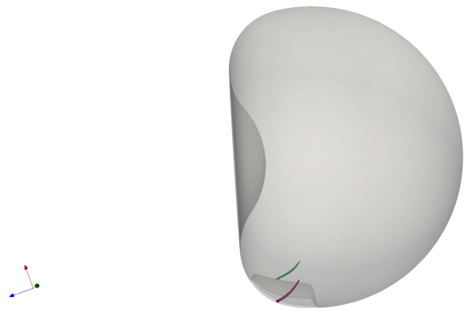

(c) Comparisons of deformations of retinal tears with scleral buckle (in green) and without scleral buckle (in red)

Figure 5.24: Comparison between deformations of retinal tear without scleral buckle and with scleral buckle.

In order to better understand if any change in deformations occurs when the scleral buckle is present, Figure 5.24 provides also a direct comparison of simulations with and without scleral buckle (c). It is possible to see that, in presence of indentation, the retinal tear bends slightly less. Even if this difference is very small, it is possible to attribute it to the reduced lateral distance of the retinal break from the axis of rotation due to indentation. It is known that one of the effects of scleral buckle is the approach of retinal tear to vitreous gel in order to reduce retinal traction, but these results suggest an impact of scleral buckle on fluid dynamics, even in absence of a gel part of humor vitreous attached to the retinal tear.

Chapter 6

Conclusions

Rhegmatogenous Retinal Detachment is a serious condition interesting a relevant percentage of the population and potentially leading to blindness. This illness originates from retinal breaks, which may vary in their shape, position and pathological origin. Retinal breaks can be classified in three different groups based on their shape: retinal holes, retinal tears and dialyses; of these, retinal holes and retinal tears are taken into account in this work.
In spite of the wide diffusion of this pathological condition, a gap of knowledge has been found regarding the formation and progression of retinal breaks to their evolution into retinal detachment. For this reason, the purpose of this work is to fill this gap of knowledge through a numerical study of the fluid-structure-interaction on retinal holes and retinal tears.
In order to accomplish this purpose, an FSI approach was used, thanks to the use of a numerical solver based on two different coupled mainstays: a flow solver for the fluid dynamics of the liquefied vitreous and a structural solver for biological tissues. As far as the flow solver is concerned, it is based on central, second-order, finite differences, with the eye placed in a Cartesian computational domain and no-slip conditions on wet surfaces imposed through an Immersed Boundary Method.
Inside this work, two different problems were considered. Retinal holes have been analysed in detail and a comparison was made between peeling stresses acting on retinal holes on emmetrope eyes and myopic eyes and among different position of the holes. This study was considered of particular interest since myopic eyes have shown, in nature, a greater tendency of retinal holes to degenerate into retinal detachment. For this reason, retinal holes at three different sections (anterior to the equator, posterior to the equator and macular) and at different angles for each section where studied in both an emmetrope and a myopic eye. When it comes to numerical simulations, some assumptions where used, such as a completely liquefied vitreous, a constant retinal thickness and a constant diameter for retinal holes along the axial length of the eye. Moreover, a detachment criterion was chosen to compare the values of peeling stress obtained from simulations for each configuration in order to determine the most critical ones that may lead to retinal detachment and to analyze

the factors that play an important role for the disease progression. From simulations, it was found that a combination of axial distance and lateral distance from the axis of rotation is necessary to develop values of peeling stress sufficient to induce retinal detachment in absence of external forces. In particular, it was found that the most critical configurations involved both the emmetrope and the myopic eye with retinal holes located posteriorly to the equator on the plane on which the rotation occurs (the xy plane); on the other side, macular positions resulted as less critical due to the almost null lateral distance from the axis of rotation. Indeed, values of peeling stress depend on both pressure gradients and shear stresses, whose magnitude depends on both the axial and the lateral distance from the axis of rotation.
Retinal tears where studied in a preliminary way, due to the greater complexity of that problem, which should involve the presence of vitreoretinal tension. For the sake of this preliminary approach, the strong assumption of completely liquefied vitreous was made, which led to the absence of vitreoretinal tension. Different orientations of retinal tears were compared to determine those which deform the most during the motions. Results showed that retinal tears oriented as the axis of symmetry or with a 45° angle between the axis of symmetry and the axis of rotation are the most dangerous. This is probably due to a prevalent contribution of pressure gradients rather than shear stresses on the surface due to the orientation of retinal tears with respect to the motion. Later, a comparison on deformations was made on an eye with retinal tear before and after the application of a radially-oriented scleral buckle. Results show less deformations when the scleral buckle is applied; this is probably due to the indentation created by the presence of the scleral buckle, which reduces the distance bewteen the retinal tear and the axis of rotation.
This work constitutes a completely innovative approach towards computational fluid dynamics applied to retinal diseases. Even if other works have used computational sources to study retinal disease, it was the first time a 3D model was applied to retinal tissues to investigate the fluid-structure-interaction. That of retinal diseases is a huge topic, involving several cases, parameters and hypotheses, since it still isn't completely known from several points of view; for this reason, this work has been conducted in collaboration with experienced ophthalmologists, who have helped to select some problems of practical interest and to understand the acceptability of some limits imposed by computational resources. Along with continuous discussion with ophthalmologists, a perpetual study of literature material regarding eye diseases and the use of computational fluid dynamics to study them has been carried on.
In spite of all of these considerations, this work still constitutes a first approach of this kind to this topic and, for this reason, it has some flaws and some limits. First of all, both the study on retinal holes and that on retinal tears are based on the hypothesis of completely liquefied vitreous; as stated before, this hypothesis is acceptable for retinal holes, but it is unrealistic for retinal tears, where vitreoretinal traction is relevant for the evolution of the break. For this reason, a more accurate study including a biphasic fluid would be interesting and might give more reliable results, especially as far as retinal tears are involved. Regarding retinal holes, for

both the emmetrope and the myopic eye the same axis of rotation was used, in order not to have a huge amount of variables; it is not known for sure how accurately it represents a real case, but it could be interesting to investigate this aspect with further simulations. Finally, simulations on retinal holes have given interesting and explainable results for holes with a 3 mm diameter, but other simulations might be run with more realistic dimensions, like a smaller diameter varying along the axis of symmetry.

This study is a starting point for further investigation about this topic and its setting allows one to push further with the problem, going to simulate a progressive detachment of the retina from the hole, in accordance with the chosen detachment criterion, thanks to models made with coincident nodes between choroid and retina. Another case of interest might involve simulations to compare retinal holes in emmetrope and in myopic eyes taking into account morphological changes of retina (like its thickness) due to the axial elongation of the eye in the myopic case.

Finally, it might be interesting to run simulations with a periodic repetition of saccadic movements, alternating a clockwise rotation to a counterclockwise one, in order to evaluate the risks of retinal detachment due to mechanisms of fatigue, rather than from a static point of view.

In spite of all the limits and improvements listed above, results obtained from simulations, especially as far as retinal holes are compared, are a very useful starting point for more accurate studies on this pathology. Even these preliminary results might be used to evaluate risk factors for retinal detachment for each patient basing on the position of retinal breaks on their eye and on the presence of myopia. The outcome might be the possibility to predict whether a retinal break might degenerate and to schedule more ophthalmological controls to evaluate the progression of the breaks or earlier surgical operations for those patients with breaks in critical positions. This possibility would lead to a less invasive approach to eye diseases based on predictive medicine, that might reduce medical costs and number of hospitalizations. Moreover, the knowledge of risk factors for retinal detachment might be useful to develop less invasive and more taylor-made surgical procedures to stop retinal detachment even in the most critical cases.

Bibliography

[1] "Modeling of Mass Transport Processes in Biological Media". In: ed. by Sid M. Beckeret al. Academic Press, 2022. Chap. 13.

[2] Federica Di Michele et al. "A mechanical model of posterior vitreous detachment and generation of vitreoretinal tractions". In: *Biomechanics and Modeling in Mechanobiology* (July 2020), p. 15.

[3] Charles P.Wilkinson. *Scleral Buckling for Rhegmatogenous Retinal Detachment*. Available on line. URL: https://eyewiki.aao.org/Scleral_Buckling_for_Rhegmatogenous_Retinal_Detachment.

[4] R.G. Michels J.T. Thompson. "Volume displacement of scleral buckles". In: *National Library of Medicine* (1985).

[5] "Retina". In: ed. by Stephen J. Ryan et al. Elsevier, 2013. Chap. 99.

[6] J. Vroon et al. "Numerical study of the effect of head and eye movement on progression of retinal detachment". In: *Biomechanics and Modeling in Mechanobiology* (2018).

[7] Rodolfo Repetto et al. "Experimental investigation of vitreous humour motion within a human eye model". In: *Physics in Medicine and Biology* (2005).

[8] Francesco Viola et al. "High-fidelity model of the human heart: An immersed boundary implementation". In: *Physical Review Fluids 8* (2023).

[9] T. Ung et al. "Clinical features and surgical management of retinal detachment secondary to round retinal holes". In: *Eye* (2005).

[10] William J Foster. "Bilateral Patching in Retinal Detachment: Fluid Mechanics and Retinal Settling". In: *Investigative Opthalmology Visual Science* (2011).

[11] Michael Siegel Tom Chou. "A mechanical model of retinal detachment". In: *Physical Biology* (2012).